Solving Quantum Many-Body Problems on Quantum Computers

Baptiste Anselme Martin

université
PARIS-SACLAY

Solving Quantum Many-Body Problems on Quantum Computers

Résoudre le problème quantique à N-corps à l'aide de calculateurs quantiques

Thèse de doctorat de l'université Paris-Saclay

École doctorale n°564, Physique en Île-de-France (PIF)
Spécialité de doctorat : Physique
Graduate School : Physique
Référent : Faculté des sciences d'Orsay

Thèse préparée au **Laboratoire de Physique des Solides** (Université Paris-Saclay, C.N.R.S.), sous la direction de **Pascal SIMON**, professeur à l'Université Paris-Saclay, et la co-supervision de **Marko RANCIC**, quantum computing project lead à TotalEnergies.

Thèse soutenue à Paris-Saclay, le 04 décembre 2023, par

Baptiste ANSELME MARTIN

Composition du jury

Membres du jury avec voix délibérative

Denis LACROIX Directeur de Recherche, Université Paris-Saclay, C.N.R.S.	Président
Andrew GREEN Professeur, University College London	Rapporteur & Examinateur
Peter ORTH Professeur, Universität des Saarlandes	Rapporteur & Examinateur
Cécile REPELLIN Chargée de recherche, Université Paris-Saclay, C.N.R.S.	Examinatrice

THESE DE DOCTORAT
NNT : 2023UPASP179

université PARIS-SACLAY

ÉCOLE DOCTORALE
Physique en Île-de-France (PIF)

Titre : Résoudre le problème quantique à N-corps à l'aide de calculateurs quantiques
Mots clés : Calcul quantique, matière condensée, NISQ, réseaux de tenseurs

Résumé : Les calculateurs quantiques promettent de résoudre des problèmes insolvables pour les ordinateurs classiques. En particulier, manipuler des états superposés et intriqués de bits quantiques est une voie naturelle pour étudier la physique des systèmes quantiques à N-particules. Avec les avancées rapides des technologies quantiques, nous avons pu voir émerger les premiers processeurs quantiques, nommés processeurs "NISQ" (de l'anglais *Noisy-Intermediate-Scale-Quantum*). Les progrès de ces machines ouvrent de nouveaux chemins aux physiciens pour simuler des systèmes quantiques. Cependant, leur taille limitée et les erreurs liées à la décohérence limitent fortement leur usage aujourd'hui. La conception d'algorithmes quantiques efficaces, résistant aux erreurs, est un défi considérable.

Ce travail de thèse s'attelle à comprendre les capacités des processeurs quantiques à simuler des systèmes quantiques à N-corps, avec une attention particulière aux applications pour la physique de la matière condensée. Dans un premier temps, nous abordons le sujet du calcul de l'état fondamental d'Hamiltoniens, à l'aide d'un algorithme variationnel quantique-classique (nommée l'algorithme VQE, de l'anglais *Variational Quantum Eigensolver*). Nous évaluons les performances de cette méthode sur le modèle de Hubbard, grâce à différentes métriques, comme la fidélité, l'énergie et les propriétés physiques des solutions obtenues. Nous démontrons, malgré des performances prometteuses en simulant un calculateur quantique sans bruit, que le niveau de bruit des machines contemporaines rend impossible la réalisation d'un calcul significatif.

En revanche, certains états quantiques aux propriétés intéressantes peuvent avoir une forme simple. Leur préparation sur un calculateur quantique est un problème pertinent dans le but d'initialiser un calcul quantique avec ces états pour les amener vers des régimes où ils perdent leur forme simple. Pour illustrer ceci, nous prenons l'exemple du modèle Affleck-Lieb-Kennedy-Tasaki (AKLT), le premier modèle de chaîne de spin entier antiferromagnétique possédant une solution simple vérifiant la conjecture d'Haldane. Nous proposons deux schémas pour préparer les états AKLT, l'un suivant leur construction naturelle en projetant des paires de qubits sur leur sous-espace triplet, l'autre utilisant leur forme de réseaux de tenseurs. Nous analysons l'implémentation de ces méthodes en fonction de la taille du système, avec une réalisation expérimentale sur un processeur quantique.

Enfin, nous explorons la synergie entre les méthodes de réseaux de tenseurs et les calculateurs quantiques bruités pour simuler la dynamique hors-équilibre de systèmes de spins. La simulation de dynamique quantique est une tâche naturelle pour les calculateurs quantiques, mais atteindre des temps longs est fortement limité par le bruit. D'autre part, les réseaux de tenseurs sont également limités aux temps courts, contraints par la quantité d'intrication qu'ils peuvent encoder. Nous proposons d'utiliser le meilleur des deux mondes : la dynamique à temps court est simulée efficacement par un réseau de tenseur, compilée vers des circuits quantiques de faible profondeur pour poursuivre l'évolution temporelle sur le calculateur quantique. Nous étudions les performances de ce schéma hybride quantique-classique en regardant la fidélité des états obtenus et la production d'intrication, avec une validation expérimentale. Finalement, nous proposons d'optimiser les circuits quantiques approximant l'opérateur évolution temporelle grâce à des réseaux de tenseurs, résultant en une simulation quantique classiquement améliorée utilisant moins de ressources quantiques.

université PARIS-SACLAY | ÉCOLE DOCTORALE Physique en Île-de-France (PIF)

Title : Solving Quantum Many-Body Problems on Quantum Computers
Keywords : Quantum Computing, Condensed Matter, NISQ, Tensor Networks

Abstract : Quantum computers hold the promise of solving problems intractable to their classical counterparts. In particular, by encoding and manipulating superposed and entangled quantum states in a controlled fashion, they provide a natural pathway to study and simulate quantum many-body systems. The rapid progress made in quantum technologies led to the emergence of Noisy-Intermediate-Scale Quantum (NISQ) devices. These NISQ devices, with their increasing qubit counts and improved control, offer exciting opportunities for physicists to explore new pathways to solve complex problems. However current devices are prone to noise which strongly limits their capacities. Finding efficient algorithms that are resilient to hardware errors is a massive challenge.

This thesis focuses on understanding the capabilities of quantum devices to simulate quantum many-body systems, with specific emphasis on condensed matter physics. First, we address the ground state search problem by benchmarking the Variational Quantum Eigensolver (VQE), a hybrid quantum-classical algorithm, on the Hubbard model, a paradigmatic model to describe interacting electrons. We report its performances in terms of fidelity, energy, and physical properties, with respect to circuit complexity and noise. We show that while noiseless simulations indicated promising prospects, the current noise level prohibits any substantial quantum computations.

However, interesting states can have a simple tractable form, and preparing them on a quantum computer is an interesting task to initialize a quantum computation towards a regime where these states lose their simplicity. To illustrate this, we focus on the example of the Affleck-Lieb-Kennedy-Tasaki (AKLT) model, the first tractable Hamiltonian of a spin-1 Heisenberg chain confirming Haldane's conjecture. We used two methods to realize the 1D AKLT ground state on a quantum device, one following the natural construction of the AKLT state by projecting pairs of qubits onto their triplet subspace thanks to ancillary qubits, while the second one uses the Matrix Product State (MPS) form of the AKLT state, along with analyzing the scalability of the schemes and implementing it on a small device.

Third, we explore the synergy of tensor network (TN) techniques with noisy quantum computers to simulate far-from-equilibrium dynamics Simulating quantum dynamics is a very natural task for quantum computers, but long-time simulations are hindered by noise. On the other hand, state-of-the-art tensor networks can only access short-time dynamics as they are limited to moderately entangled states. We use the best of both worlds : the short-time dynamics is efficiently performed by TNs, compiled into short-depth quantum circuits followed by Trotter circuits run on a quantum computer. We investigate the performance of this hybrid-classical in terms of fidelities and entanglement production taking into account a realistic noise model and validate it experimentally on a small-scale quantum device. Finally, we also propose to use TN to optimize the circuits for time evolution, leading to a fully TN-enhanced quantum simulation using fewer quantum resources.

Aknowledments, Remerciements

I would like to first thank the jury members for kindly accepting to be a part of my very last challenge as a Ph.D. student and taking some much of their time to review my work and come to the LPS for the defense. Thank you to Andrew Green and Peter Orth for their constructive reports on the manuscript of this thesis. I am very grateful to Denis Lacroix and Cécile Répellin for their participation and their benevolence.

Thank you to my two supervisors, Pascal and Marko, for welcoming me to their respective entities, Total and the LPS, teaching me the ways of research, and sharing their experiences. In particular, thank you Pascal for your benevolence and your pragmatism, as well as the few runs in the Orsay forest.

I also thank Richard Deblock and Thomas Ayral for following me as members of my "comité de suivi". I also thank Thomas Ayral and François Jamet for our collaboration, I discovered a fun yet important aspect of research.

The last three years would not have been the same without the cool colleagues that I had the chance to meet and spend time with. A big thank you to my colleagues at Total(Energies). I had the chance to discover there a variety of profiles, expertise, and scientific topics, which definitely opened my mind and gave me keys for my future. My warmest thanks to all the Ph.D. students who quickly became friends, Naoufal, Cheichknah, Amin, Mohammad, Benjamin, Elie, Ali, Yagnik, and Wassil for all the coffee breaks, the fun at NanoInnov, the Playground or Mathias, and all the good times at and outside of the office. Big up to the quantum team for all our scientific (or not) discussions. You guys made my time at Total so much more enjoyable and you will be what I will remember first from my experience there.

I am also very grateful for the environment at the LPS. Thank you to all the members of the theory group. The friendly atmosphere, everybody's passion, and the numerous coffee breaks made my time at the LPS a great experience. I have been very lucky to meet the Ph.D. students and people from the LPS staff, who were a big part of my motivation to come to the lab. Thank you to Antoine C., Florian, my co-bureau Lise, Thibault, Reda, Xavier, Léo, Alice E.-S., Alice R., Alexis, Suzanne, Malar, Antoine, and Thomas. A special thank you to the old student gang, Jean-Baptiste, Ansgar, Marina, Etienne, and Mateo. I am proud to count you as my friends, and all the little moments at the lab, in Paris, or at the PMU of Bures-sur-Yvette were very precious.

Merci à Valentin Vie pour les bons moments partagés à Alésia, ainsi que pour l'accès à son infrastructure de calcul haute performance.

Je remercie ma famille et mes parents qui m'auront toujours soutenu, fait confiance

et aidé dans mes choix. Ma réussite est la leur.

Enfin, je remercie de tout mon cœur Angèle pour son soutien inconditionnel qui aura été si important.

Résumé

Au cours de ces dernières années, les technologies quantiques ont connu un développement rapide et intense, entraînant un grand enthousiasme non seulement au sein la communauté scientifique, mais également du grand public. En tête de file, les calculateurs quantiques apportent la promesse d'un nouveau paradigme de calcul permettant de résoudre des problèmes aujourd'hui inaccessibles, et ce dans de nombreux domaines scientifiques. Ces calculateurs utilisent la mécanique quantique au cœur de leur fonctionnement: en contrôlant des systèmes physiques à l'échelle quantique, elles encodent et manipulent une grande quantité d'information via deux phénomènes clefs, la superposition et l'intrication de bits quantiques, ou qubits.

Les idées fondatrices du calcul quantique émergent dans les années 1970 et 1980 [1, 2, 3, 4, 5], motivées par la grande difficulté des simulations des systèmes quantiques. En revanche, ce n'est que récemment que nous avons pu assister à un progrès radical des prototypes de calculateurs quantiques, dans les laboratoires de recherche tout d'abord, puis au sein d'acteurs industriels et start-ups. Ces avancées sont telles qu'il est aujourd'hui possible d'accéder et programmer ces calculateurs quantiques en tant qu'utilisateur depuis des services en ligne [6]. Ces machines, de taille modérée et sujettes au bruit, sont appelées *NISQ*, de l'anglais *Noisy-Intermediate-Scale-Quantum device* [7] (machine quantique bruitée de taille intermédiaire en français). Leur développement a engrangé une explosion de la recherche en calcul quantique, qu'elle soit expérimentale, théorique ou algorithmique, avec en ligne de mire l'objectif d'atteindre un *avantage quantique*.

Le terme "avantage quantique" fait référence à la supériorité des algorithmes quantiques sur les méthodes classiques pour réaliser un calcul. On peut cependant faire la distinction entre deux natures différentes. On nommera premièrement l'*avantage de complexité*. Celui-ci qui vise à l'élaboration d'algorithmes quantiques dont le coût, connu et contrôlé, est meilleur que celui des algorithmes classiques lorsque la taille du problème augmente. C'est par exemple le cas de l'algorithme de Shor [8, 9], algorithme paradigmatique permettant la factorisation de nombres premiers. En revanche, la conception d'algorithmes dont la complexité favorable est démontrée et sans ambiguïté représente une véritable dif-

ficulté. De plus, les erreurs et imperfections des prototypes de calculateurs quantiques rendent presque impossible l'implémentation de ces algorithmes. La démonstration d'un avantage quantique implique la capacité d'une machine quantique à réaliser un calcul inaccessible aux algorithmes classiques. En pratique, cela signifie que les erreurs induites par le bruit expérimental sont inférieures aux approximations, conceptuelles ou numériques, des outils classiques. Cet avantage est qualifié d'*avantage pratique*. Différentes expériences réalisées grâce à des machines quantiques ont annoncé avoir atteint un avantage quantique [10, 11, 12, 13], mettant en avant l'argument de la complexité de la tâche réalisée, mais celles-ci ont toujours été nuancées au vu de simulations classiques avec approximations [14, 15, 16, 17].

Dans cette thèse, nous étudions la possibilité d'utiliser les calculateurs quantiques pour résoudre des problèmes paradigmatiques de la physique quantique à N-corps et de la matière condensée, avec une attention particulière pour les implémentations expérimentales sur les machines disponibles aujourd'hui. Après une introduction aux concepts fondateurs du calcul quantique donnée par le Chapitre 1, le Chapitre 2 s'intéresse à la recherche d'états fondamentaux de systèmes d'électrons corrélés. Déterminer l'état fondamental, ou état de plus basse énergie, d'un système physique est au cœur de la mécanique quantique, car il permet de connaître et de comprendre la nature et les propriétés physiques du système étudié. En mécanique quantique, l'énergie d'un système est décrite par un Hamiltonien H. Cet opérateur permet de calculer l'énergie E d'un état normalisé $|\Psi\rangle$ via $E = \langle H \rangle = \langle \Psi | H | \Psi \rangle$. Ainsi, déterminer l'état fondamental $|\Psi_0\rangle$ ayant l'énergie la plus basse E_0 peut être formulé comme un problème de valeur propre :

$$H\,|\Psi_0\rangle = E_0\,|\Psi_0\rangle\,. \tag{1}$$

Dans un cas général, l'Hamiltonien H est représenté par une matrice aux dimensions croissant exponentiellement avec le nombre de degrés de liberté du système ($2^N \times 2^N$ pour N spins-1/2 ou qubits). De même, un état $|\Psi\rangle$ prend la forme d'un vecteur encodant les amplitudes associées aux différents états formant une base. Obtenir les valeurs et vecteurs propres de H devient ainsi une tâche exponentiellement coûteuse à mesure que le taille du problème augmente. L'élaboration et l'utilisation de représentations efficaces sont des éléments clef pour simuler un système à N-corps quantique. En revanche, les calculateurs quantiques proposent une voie alternative naturelle pour encoder et manipuler des états quantiques à plusieurs particules: en préparant et contrôlant un véritable état quantique, réalisé par le calculateur quantique. En augmentant le nombre de bits quantiques et leur niveau de contrôle, les calculateurs quantiques promettent de préparer des états corrélés hors de portée des calculateurs classiques. Néanmoins, accéder à de tels états n'implique pas de savoir comment les utiliser, par exemple pour trouver l'état fondamen-

tal d'un Hamiltonien donné. C'est ce à quoi s'attele le champ de recherche des algorithmes quantiques: utiliser la puissance des calculateurs quantiques afin de réaliser des tâches inaccessibles aux algorithmes classiques. Ces considérations sont larges, de l'étude théorique du coût algorithmique de ces méthodes à des considérations pratiques, comme la résilience aux erreurs ou l'implémentation expérimentale pour une machine donnée. Dans le but de simuler des systèmes quantiques avec interaction, nombre d'algorithmes quantiques ont été proposés, à la fois pour des machines avec correction d'erreur (inexistantes aujourd'hui) et des calculateurs dits NISQ.

Ce travail explore la possibilité d'utiliser des calculateurs quantiques dans le but de simuler des fermions corrélées. Ayant en ligne de mire les machines actuelles NISQ, nous choisissons de tester les performances de l'algorithme *Variational Quantum Eigensolver* [18, 19] (VQE, solveur quantique variationnel du problème aux valeurs propres en français). L'algorithme VQE, sans doute l'algorithme NISQ le plus proéminent, est une méthode hybride classique-quantique. Dans ce schéma, le calculateur quantique prépare un état variationnel grâce à un circuit dépendant de paramètres. L'énergie de l'état selon l'Hamiltonien étudié est évaluée grâce à des mesures sur l'état, puis les paramètres sont optimisés par un processeur classique dans le but de minimiser l'énergie. Ici, l'unique rôle de la machine quantique est de préparer un état quantique.

Afin de comprendre les capacités de cette approche, nous faisons le choix d'un circuit paramétré appelé *Variational Hamiltonian Ansatz* (VHA) [47, 48, 51, 52], inspiré du principe d'évolution adiabatique pour la préparation d'états fondamentaux. Nous testons ses performances pour le modèle de Hubbard unidimensionnel, un des modèles phares décrivant les interactions entre électrons. Grâce à des simulations classiques exactes, nous analysons l'énergie minimisée ainsi que la fidélité des états optimisés en fonction de la complexité du circuit et du paramètre d'interaction du modèle. Nous démontrons que cette méthode est performante, mais nécessite des circuits profonds lorsque l'interaction entre électrons devient importante. C'est sous le prisme de la physique de la matière condensée que nous explorons ensuite l'aptitude de l'approche VQE à observer la physique du modèle Hubbard. Nous évaluons des observables physiques, notamment les corrélations de charge et de spin. Nous observons que des circuits de longueur modérée permettent de retrouver la physique à court portée, tandis que les corrélations à plus longue portée requièrent des circuits plus profonds. Enfin, dans le but de comprendre son comportement en situation réelle, nous effectuons des simulations de l'algorithme avec un modèle de bruit ainsi qu'une implémentation expérimentale sur un prototype de calculateur quantique d'IBM [6]. Nous nous concentrons sur un problème à 2 sites (4 qubits), tout en incorporant des techniques de réduction d'erreur. Bien que les niveaux d'erreur dégradent drastiquement la qualité des résultats, la combinaison de techniques de réduction d'erreur semble indiquer qu'il est

possible d'extraire l'information utile des états bruités, fournissant un accord au moins qualitatif des résultats expérimentaux avec ceux attendus.

Bien que déterminer les états fondamentaux de systèmes quantiques peut en général devenir une tâche herculéenne, il existe de nombreux cas pour lesquels ces états exhibent une forme simple et facile à représenter. À l'inverse, étudier leur dynamique peut devenir un véritable défi pour les simulations classiques, l'état du système perdant sa forme simple. De plus, explorer la physique autour de ces points exactement solubles peut également devenir une tâche difficile. L'utilisation de calculateurs quantiques peut ouvrir une nouvelle voie pour ces problèmes classiquement difficiles.

Par exemple, de nombreux algorithmes quantiques, comme VQE, reposent sur la préparation d'un bon état initial, au plus proche de la solution exacte. Dès lors, être en mesure de préparer ces états représentables classiquement présente un réel intérêt. Dans le Chapitre 3, nous nous attardons sur l'exemple de chaîne antiferromagnétique de spin-1, en particulier du modèle AKLT [20](pour Affleck-Lieb-Kennedy-Tasaki), le premier modèle vérifiant la conjecture d'Haldane [21, 22], et dont l'état fondamental revêt une forme simple. Dans le but de préparer ces états de spin-1 sur un calculateur quantique basé sur des bits quantiques, nous explorons deux méthodes distinctes. La première se base sur la construction naturelle des états AKLT, où chaque site de spin-1 est obtenu à partir de deux spin-1/2 (ou ici des qubits). Chaque spin-1/2 forme un état singulet avec un spin-1/2 d'un site voisin, puis chaque pair de spin-1/2 d'un même site est projetée vers un état de spin-1. Nous proposons de suivre cette construction en utilisant des qubits auxiliaires pour réaliser la projection. La deuxième méthode se base sur l'écriture des états AKLT sous forme de Matrix Product States (MPS, état produit de matrices en français) [23, 24]. Nous prenons inspiration de ce formalisme pour concevoir des circuits quantiques préparant de manière efficace les états AKLT, ne nécessitant qu'une seule projection. Nous comparons le coût de ces deux méthodes à la fois en termes de nombre de portes quantiques, mais aussi du nombre moyen nécessaire de projections. Nous démontrons que la méthode projective est plus favorable aux implémentations NISQ pour des réalisations expérimentales de petite taille, grâce à ses circuits moins coûteux. En revanche, le second schéma, basé sur le formalisme MPS, présente un meilleur coût lorsque le nombre de sites devient grand, grâce à un nombre de répétitions devenant constant. Afin de valider nos techniques, nous les implémentons sur les machines quantiques d'IBM. Nous réalisons une tomographie quantique afin de reconstruire l'état produit expérimentalement. Nous démontrons avec succès la préparation d'états AKLT à 2 sites (soit 4 qubits), et confirmons les résultats attendus, i.e. une fidélité supérieure pour la méthode projective, en dépit d'un nombre de post-sélection moins favorable. Ces résultats valident une voie intéressante et pragmatique pour le calcul quantique, à savoir l'implémentation d'états fondamentaux classiquement

accessibles.

L'ensemble des contraintes imposées par les machines quantiques actuelles nous pousse à devoir cibler les problèmes pour lesquels atteindre un avantage quantique est le plus plausible. Pour ce faire, il est essentiel de comprendre les méthodes classiques, leur force, mais surtout leur faiblesse, et avoir en point de mire les scénarios où elles échouent sans ambiguïté. C'est dans cette perspective que le Chapitre 4 s'attarde sur la simulation de dynamique quantique hors-équilibre. Lorsqu'un système quantique est poussé loin de son état d'équilibre, l'état décrivant le système devient très intriqué. Or, représenter des états à plusieurs particules avec une grande quantité d'intrication est précisément l'obstacle majeur pour les techniques numériques modernes, notamment pour les réseaux de tenseurs et MPS [23, 25, 24, 26, 27, 28, 29].

Comme nous l'avons évoqué dans le Chapitre 3, les méthodes basées sur MPS sont particulièrement efficaces pour déterminer les états fondamentaux de systèmes unidimensionnels, ainsi que pour manipuler des états faiblement intriqués. En revanche, elles restent limitées pour simuler la physique hors-équilibre, où l'intrication peut augmenter de manière balistique avec le temps, le coût de simulation devenant alors exponentiel. D'un autre côté, les calculateurs quantiques sont naturellement propices à générer des états quantiques et performer leur propagation en temps, mais restent limités par le bruit. Dans ce Chapitre, nous utilisons le meilleur des deux mondes : la simulation à temps court est réalisée efficacement par des MPS, compilés en circuits quantiques courts optimisés grâce à des méthodes de réseaux tensoriels. Ces états MPS peuvent être ainsi implémentés sur un calculateur quantique, qui poursuit leur évolution temporelle au-delà de la limite classique. Afin d'évaluer les performances de cette démarche mêlant classique et quantique, nous utilisons un modèle de bruit et évaluons la fidélité des états et la quantité d'intrication produite en fonction du temps de simulation et du niveau de bruit. Nous concluons que cette approche permet de battre les simulations MPS, tout en abaissant significativement les niveaux de bruit nécessaires pour atteindre un avantage quantique. Nous confirmons nos résultats avec une réalisation expérimentale sur une machine d'IBM, où notre méthode permet à la fois de réaliser de meilleures performances qu'une méthode MPS de faible coût et une simulation purement quantique. Enfin, nous proposons d'étendre notre méthode en optimisant les circuits quantiques utilisés pour la propagation des états MPS. Pour ce faire, nous développons une méthode basée sur des MPO (Matrix Product Operators, opérateurs produit de matrices en français) permettant de compresser les circuits utilisés pour l'évolution temporelle en des circuits courts et efficaces en terme de production d'intrication. Cette extension permet de fournir au calculateur quantique tous les ingrédients pour une simulation quantique efficace, classiquement optimisée. Cette approche ouvre une voie pragmatique et performante pour atteindre un avantage quantique.

Introduction

Over the past few years, we have witnessed a rapid progress of quantum technologies, which brought a lot of enthusiasm in the scientific community as well as for the general public. At the forefront of this interest for quantum physics lie quantum computers, raising the hope to solve intractable problems in a variety of scientific domains.

Original ideas of quantum computation emerge in the 1970s and 1980s [1, 2, 3, 4, 5], motivated by the hardness of simulating quantum systems. However, it is only recently that we have observed a radical improvement of quantum devices, from academic research groups to industrial actors, to the point that we can now manipulate (small and noisy) quantum computers as a high-level user on cloud-based services [6]. These so-called Noisy-Intermediate-Scale-Quantum devices (NISQ) [7] have led to a tremendous growth of the field of quantum computing, from the experimental to theoretical and algorithmic research, with main objective of reaching a *quantum advantage*.

The term "quantum advantage" is often used to refer to the superiority of quantum computers over classical methods to perform a computation. We can however distinguish between two kinds of quantum advantage. The first one, which we could refer to as *complexity advantage*, corresponds to designing quantum algorithms with a favorable complexity scaling with respect to problem size over classical algorithms. This is for instance the case for the famous Shor algorithm [8, 9] for prime factorization. But finding algorithms that exhibit a clear and unambiguous favorable scaling over existing methods is not a trivial task. Additionally, the noise inherent to quantum devices makes the realization of such algorithms extremely challenging. Demonstrating an advantage for a computational task implies that quantum computers demonstrate the ability to perform a computation believed to be beyond the capacity of any classical methods. In practice, this often signify that the errors from noise are lower than the approximations, conceptual or numerical, used by the classical methods. We can refer to this as *practical advantage*. Different experiments with quantum devices have claimed to have perform a computation task beyond classical capabilities [10, 11, 12, 13], putting forward the complexity argument of the task, but these announcements were often nuanced in regards of comparison with

classical approximated solutions [14, 15, 16, 17].

In this thesis, we focus on the latter by investigating the feasibility of using quantum computers to solve paradigmatic problems in quantum many-body physics and condensed matter physics, with a focus on experimental implementations on currently available quantum devices. After an introduction to the basic concepts and tools in quantum mechanics and quantum compution in Chapter 1, we investigate in Chapter 2 the possibility of using quantum computers to find ground states of interacting fermionic models, namely the Hubbard model, a simple but crucial model to model electrons with Coulomb repulsion. To do so, we choose the Variational Quantum Eigensolver (VQE) [18, 19], one of the most prominent algorithm proposed for NISQ devices. VQE employs a quantum computer to prepare a quantum state, supposedly intractable for classical computer, thanks to a parameterized quantum circuit, whose parameters are optimized thanks to a classical optimizer.

Despite finding ground states are in general a very challenging endevor, interesting models exhibiting rich physics can be formulated with simple tractable forms. Preparing such states on a quantum computer is an useful task to bring them toward regimes where they lose their simplicity. In the Chapter 3, we focus on the Affleck-Lieb-Kennedy-Tasaki (AKLT) states [20], the first tractable ground states of antiferromagnetic spin-1 systems verifying the Haldane conjecture [21, 22]. We explore two preparation schemes, one based on their natural construction by performing local projection of pairs of qubits onto their triplet subpace, the other one based on their Matrix Product State (MPS) [23, 24] form.

Taking into account the numerous constraints surrounding the performances of current quantum devices, finding an advantage requires to focus on physical problems where classical methods unambiguously fail while being adequate to quantum computers. With this in mind, we focus in Chapter 4 on the simulation of out-of-equilibrium quantum dynamics, where states are driven towards high level of entanglement. Representing large amount of entanglement is the key bottleneck to state-of-the-art numerical techniques for simulation of quantum systems, namely tensor network and MPSs [23, 25, 24, 26, 27, 28, 29]. We study the synergy between MPS and noisy quantum computers to simulate quantum dynamics of a spin model with a tensor-network-enhanced quantum simulation, and quantify the noise requirement to obtain an advantage over MPS.

Table of contents

1 | Elements of quantum computing

In this chapter, we give the basic concepts and notations to describe quantum systems, with an emphasize on quantum bits (or qubits). We describe how to represent operations on qubits with quantum circuits, along with how to perform a computation thanks to measurement. Then, we focus on the differences between quantum states with and without noise, and how to model the behavior of current noisy devices. This introductive chapter is inspired from the textbook *Quantum Computation and Quantum Information* [30] by Isaac Chuang and Micheal Nieslen, that we recommand for further reading.

1.1 Quantum mechanics and quantum bits

1.1.1 Quantum states and linear algebra

The description of quantum objects is based on linear algebra, that gives tools to describe vector spaces. In particular, quantum objects that possess n degrees of freedom are described by vectors living in the vector space $\mathbb{C}^n$. The vector space describing all the possible configurations of a given quantum object is called *Hilbert* space. The standard *ket* notation for a quantum state ψ is $|\psi\rangle$ such that

$$|\psi\rangle = \begin{pmatrix} \psi_1 \\ \vdots \\ \psi_n \end{pmatrix}, \tag{1.1}$$

where $\{\psi_i\}$ are complex scalars. Each number ψ_i corresponds to the amplitude associated with the basis state $|i\rangle$ defined as the vector with the i-th component is 1 and zero

elsewhere. Using the ket notation, we can equivalently express $|\psi\rangle$ as

$$|\psi\rangle = \sum_{i=1}^{n} \psi_i |i\rangle . \tag{1.2}$$

From this, we can define an inner product between two vectors $|\Psi\rangle$ and $|\varphi\rangle$. To do so, we define *bra* notation such that

$$\langle\varphi| = |\varphi\rangle^\dagger = \begin{pmatrix} \varphi_1^* & \dots & \varphi_n^* \end{pmatrix}, \tag{1.3}$$

where $.^\dagger$ operates the transposition and conjugation of a matrix, such that $(a^\dagger)_{ij} = a_{ji}^*$. With this, we can define an inner (or scalar) product on the Hilbert space. The inner product between $|\psi\rangle$ and $|\varphi\rangle$ is then defined as

$$\langle\varphi|\psi\rangle = \begin{pmatrix} \varphi_1^* & \dots & \varphi_n^* \end{pmatrix} \begin{pmatrix} \psi_1 \\ \vdots \\ \psi_n \end{pmatrix} = \varphi_1^*\psi_1 + \ldots + \varphi_n^*\psi_n. \tag{1.4}$$

For example, two basis vectors $|i\rangle$ and $|j\rangle$ from an orthonormal basis obey $\langle i|j\rangle = \delta_{ij}$. The norm of the quantum state $|\psi\rangle$ is given by $\langle\psi|\psi\rangle$. The Born's rule, one of the postulates of quantum mechanics, states that the probability p_i of observing (or measuring) $|\psi\rangle$ in the state $|i\rangle$ is given by

$$p_i = |\langle i|\psi\rangle|^2. \tag{1.5}$$

Such interpretation yields the convention of describing quantum state with vectors of norm-1, such that $\langle\psi|\psi\rangle = 1$. Moreover, as an observer can only access the squared modulus of state amplitudes, two norm-1 quantum states $|\phi\rangle$ and $|\psi\rangle$ are equivalent if they are equal up to a phase, $|\phi\rangle = e^{i\alpha}|\psi\rangle$ with $\alpha \in \mathbb{R}$. In other words, quantum states are defined up to a phase.

In order to describe physical processes acting on quantum systems, as well as to compute their properties, we define operators acting on quantum states and result in new quantum states from the Hilbert space. Such operators are described by operators defined by matrices. For example an operator A acting on an Hilbert space of dimension n is described by a $n \times n$ matrix:

$$A = \begin{pmatrix} A_{11} & A_{12} & \dots & A_{1n} \\ A_{21} & A_{22} & \dots & A_{2n} \\ \vdots & \vdots & \ddots & \vdots \\ A_{n1} & A_{n2} & \dots & A_{nn} \end{pmatrix} \tag{1.6}$$

Using the bra-ket notation, we can equivalently write A as

$$A = \sum_{i=1}^{n} \sum_{j=1}^{n} A_{ij} |i\rangle\langle j| \tag{1.7}$$

The action of A on a given quantum state $|\psi\rangle$ results in another quantum state $|\psi'\rangle$ from the Hilbert space. This state can be computed as

$$\begin{aligned} |\psi'\rangle &= A\,|\psi\rangle && (1.8)\\ &= \sum_{i=1}^{n} \sum_{j=1}^{n} A_{ij} |i\rangle\langle j| \sum_{k=1}^{n} \psi_k\,|k\rangle && (1.9)\\ &= \sum_{i=1}^{n} \sum_{j=1}^{n} \sum_{k=1}^{n} A_{ij} |i\rangle \underbrace{\langle j\,|k\rangle}_{\delta_{jk}} && (1.10)\\ &= \sum_{i=1}^{n} \sum_{k=1}^{n} A_{ij} \psi_j\,|i\rangle && (1.11) \end{aligned}$$

In particular, a physical process can be modelled with a operator U. Acting on an initial state $|\psi\rangle$, $U\,|\psi\rangle$ represent the evolved state. As one of the postulates of quantum mechanics, the operator U is unitary, meaning that $U^\dagger U = UU^\dagger = \mathbb{1}$. As a consequence, the norm of $|\psi\rangle$ is conserved after the evolution of the system, and its evolution is reversible by evolving the state under $U^\dagger$ as $U^\dagger U\,|\psi\rangle = |\psi\rangle$.

1.1.2 Qubit

A quantum bit, or qubit, is the simplest example of a quantum system. Similarly to a classical bit whose value can be either 0 or 1, a qubit can be described by vector space of dimension 2, where we can identify two values 0 and 1 with two basis states

$$|0\rangle = \begin{pmatrix} 1 \\ 0 \end{pmatrix}, \quad |1\rangle = \begin{pmatrix} 0 \\ 1 \end{pmatrix}. \tag{1.12}$$

However, contrary to a classical bit, a qubit can be described by a quantum superposition of the two configurations $|0\rangle$ and $|1\rangle$.

$$|\Psi\rangle = \alpha\,|0\rangle + \beta\,|1\rangle\,, \text{with } \alpha, \beta \in \mathbb{C}. \tag{1.13}$$

The normalization condition leads to the following conditions on the coefficients α and β:

$$\langle\Psi|\Psi\rangle = |\alpha|^2 + |\beta|^2 = 1 \tag{1.14}$$

This condition guarantees that we can use the coefficients α and β to obtain the probabilitity of the two different outputs 0 and 1 as

$$p_0 = |\langle 0|\Psi\rangle|^2 = |\alpha|^2,\ p_1 = |\langle 1|\Psi\rangle|^2 = |\beta|^2 \tag{1.15}$$

A useful and equivalent notation for quantum states is to use the density matrix that we define as

$$\rho = |\Psi\rangle\langle\Psi| \tag{1.16}$$

As ρ is a Hermitian operation, meaning that $\rho^\dagger = \rho$, we can rewrite the density matrix using a basis for the 2×2 Hermitian matrix space. Along with the identity matrix $\mathbb{1}$, the Pauli matrices form a real vector space for 2×2 Hermitian matrices, that we define as

$$\sigma_x = X = \begin{pmatrix} 0 & 1 \\ 1 & 0 \end{pmatrix}, \sigma_y = Y = \begin{pmatrix} 0 & -i \\ i & 0 \end{pmatrix}, \sigma_z = Z = \begin{pmatrix} 1 & 0 \\ 0 & -1 \end{pmatrix}. \tag{1.17}$$

Consequently, the density matrix ρ can be uniquely expressed by a linear combination of Pauli matrices, with real coefficients. Combined with the normalization condition, written as $\mathrm{Tr}(\rho) = 1$, we can write the density matrix as

$$\rho = \frac{\mathbb{1} + \vec{n}.\vec{\sigma}}{2}, \tag{1.18}$$

where the Pauli vector $\vec{\sigma}$ is defined as $(\sigma_x, \sigma_y, \sigma_z)$ and $\vec{n} = (n_x, n_y, n_z)$ is a unitary vector designating a point on the unitary sphere. Such notation allows for a geometrical representation of a qubit state. As shown in Fig. 1.1, the qubit state Ψ corresponds to a point on the so-called *Bloch* sphere, given by the coordinates $\vec{n} = (\sin\theta\cos\varphi, \sin\theta\sin\varphi, \cos\theta)$, corresponding to expressing $|\Psi\rangle$ as $\cos\frac{\theta}{2}|0\rangle + e^{i\varphi}\sin\frac{\theta}{2}|1\rangle$, with θ and φ being the two angles from the Bloch sphere. While a classical bit would be represented by only the poles in the z direction, a quantum bit lives on the whole sphere.

Contrary to a classical bit that can encode one bit of information, 0 or 1, a quantum bit stores information into the amplitudes α and β. Putting together more and more qubits will allow to encode information into the amplitudes associated with the different bit strings. However, superposition is not enough to truly access the power of quantum computation as we will explain in the next section.

1.1.3 Entanglement

In order to describe the physics of multi-particle quantum systems, it is important to introduce the notion of tensor product. The tensor product yields to the construction

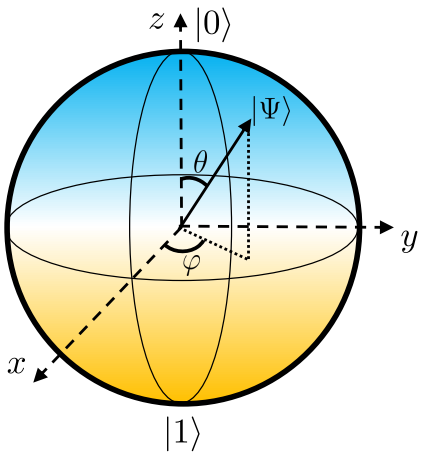

Figure 1.1: The Bloch represents the 1-qubit Hilbert space, where a state corresponds to a point of the sphere, defined by two angles θ and φ. The two poles along the z axis represent the two classical states 0 and 1.

of the Hilbert space of a many-body system from the Hilbert spaces associated with its constituting particles. Let us consider two vector spaces $\mathcal{V}$ and $\mathcal{W}$ of dimension $d_\mathcal{V}$ and $d_\mathcal{W}$. The tensor product between $\mathcal{V}$ and $\mathcal{W}$ is noted $\mathcal{V} \otimes \mathcal{W}$, and possesses a dimension $d_\mathcal{V} \times d_\mathcal{W}$. A vector belonging to $\mathcal{V} \otimes \mathcal{W}$ can be expressed as a linear combination of tensor products of the basis vectors $\{|v\rangle\}$ and $\{|w\rangle\}$ (keeping the ket notation), also noted as $|v\rangle \otimes |w\rangle$ or $|vw\rangle$.

The tensor product "$\otimes$", also called *Kronecker* product, allows to explicitly construct these objects. Let us take the example of two matrices V and W of dimension $n \times m$ and $k \times l$ respectively. The product $V \otimes W$ is a matrix of dimension $(nk) \times (ml)$ defined as

$$V \otimes W = \begin{pmatrix} V_{11}W & V_{12}W & \dots & V_{1m}W \\ V_{21}W & V_{22}W & \dots & V_{2m}W \\ \vdots & \vdots & \ddots & \vdots \\ V_{n1}W & V_{n2}W & \dots & V_{nm}W \end{pmatrix}. \tag{1.19}$$

Let us now take the example of two qubits described respectively by the Hilbert spaces $\mathcal{H}_1$ and $\mathcal{H}_2$ (with $\mathcal{H}_1 = \mathcal{H}_2 = \mathbb{C}^2$). Qubit 1 is the state $|\Psi_1\rangle$ and qubit 2 in $|\Psi_2\rangle$. As a result, the state $|\Psi_{12}\rangle$ can be described by a vector from the vector space $\mathcal{H}_1 \otimes \mathcal{H}_2 = \mathbb{C}^2 \otimes \mathbb{C}^2 = \mathbb{C}^4$, and is obtained by using Eq. 1.19 as

$$|\Psi_{12}\rangle = |\Psi_1\rangle \otimes |\Psi_2\rangle \tag{1.20}$$

$$= \begin{pmatrix} \alpha_1 \\ \beta_1 \end{pmatrix} \otimes \begin{pmatrix} \alpha_2 \\ \beta_2 \end{pmatrix} = \begin{pmatrix} \alpha_1\alpha_2 \\ \alpha_1\beta_2 \\ \beta_1\alpha_2 \\ \beta_1\beta_2 \end{pmatrix} \tag{1.21}$$

$$= \alpha_1\alpha_2 |00\rangle + \alpha_1\beta_2 |01\rangle + \beta_1\alpha_2 |10\rangle + \beta_1\beta_2 |11\rangle . \tag{1.22}$$

Having presented the tools to describe quantum systems containing multiple particles, we can define another fundamental concept of quantum mechanics alongside superposition: *entanglement*. Entanglement is the phenomenon resulting from the interaction between particles, which leads to non-classical correlations and is at the heart of the computational power of quantum computers. Taking the example of two qubits described by a state $|\Psi_{12}\rangle$, the two qubits are entangled if $|\Psi_{12}\rangle$ cannot be expressed as a tensor product of two individual qubit states $|\Psi_1\rangle$ and $|\Psi_2\rangle$:

$$|\Psi_{12}\rangle \neq |\Psi_1\rangle \otimes |\Psi_2\rangle . \tag{1.23}$$

With entanglement, a two-qubit system becomes a proper many-body system rather than a product of many single-body systems. The intriguing property of entanglement is that its effect is non-local, meaning that two entangled particles put arbitrarily far from each other will still exhibit correlations, violating local realism. This led to the famous "EPR paradox" from Einstein, Podolsky, and Rosen [31], which challenged the completeness of quantum mechanics' formulation, where Einstein argued that there should be no "spooky action at distance". The Bell's inequality, introduced by Bell [32], set an upper limit for the correlations if quantum mechanics was respecting local realism. Its violation was experimentally observed [33, 34, 35].

For example, let us consider the following state:

$$|\Psi_{12}\rangle = \frac{1}{\sqrt{2}}(|00\rangle + |11\rangle). \tag{1.24}$$

Investigating $|\Psi_{12}\rangle$, we observe that it cannot be factorized and therefore contains entanglement. This can translate into measuring correlations. For example, we can compute the 2-body correlator $C_z = \langle Z_1 Z_2\rangle - \langle Z_1\rangle\langle Z_2\rangle$. For any seperable state $|\Psi_1\rangle \otimes |\Psi_2\rangle$, $C_z = 0$. However, in this example, we obtain non-zero result as $C_z = 1$, which manifests the presence of entanglement in the system.

As a matter of fact, a two qubit system can be described using a basis of 4 orthogonal entangled states, called as the Bell states, defined as:

$$|\Psi_+\rangle = \frac{1}{\sqrt{2}}(|00\rangle + |11\rangle), \tag{1.25}$$

$$|\Psi_-\rangle = \frac{1}{\sqrt{2}}(|00\rangle - |11\rangle), \tag{1.26}$$

$$|\Phi_+\rangle = \frac{1}{\sqrt{2}}(|01\rangle + |10\rangle), \tag{1.27}$$

$$|\Phi_-\rangle = \frac{1}{\sqrt{2}}(|01\rangle - |10\rangle). \tag{1.28}$$

$$\tag{1.29}$$

Thanks to entanglement, quantum systems be can prepared into states that would not be accessible with only single-qubit superposition. From a computation perspective, entanglement enables to encode more information via the amplitudes of many-body states. Taking the example of a N-qubit quantum computer, the Hilbert space have a dimension equal to 2^N. Being able to prepare a fully entangled quantum state leads to the possibility of storing information into 2^N independant amplitudes, which underpins the power of quantum computation.

1.1.4 Quantum circuits

Quantum circuits are pictorial representations for the unitary evolution of quantum states. Reading from left to right, the state of the system is represented by a line, while a physical process U is represented by a two-legged object, the input leg is connected to the input state, which results in a new output state at the other leg, as shown in Fig. 1.2.

Figure 1.2: A quantum system in state $|\Psi\rangle$ evolves under the transformation U, which results in the new state $|\Psi'\rangle$.

For a system containing N qubits, a quantum circuit will be composed out of N lines, with unitary transformation acting on one or many qubits. Quantum circuits are quantum counterparts of classical circuits, representing a series of logical operations applied on bits. To highlight their similarities, let us take the example of the logical operator NOT that reverses the value of a classical bit. Equivalently, when using a qubit, applying the gate X also flips the state of the qubit (see Table 1.1).

Classical	Quantum
	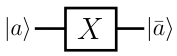

a	$\bar{a}$
0	1
1	0

$\|a\rangle$	$\|\bar{a}\rangle$
$\|0\rangle$	$\|1\rangle$
$\|1\rangle$	$\|0\rangle$

Table 1.1: The classical logic gate NOT and its quantum counterpart, the X gate.

Similarly, operations can be performed on a set of bits/qubits. For example, the classical XOR gate and its quantum version, often named CNOT, allow to flip of a bit/qubit based on the value of another bit/qubit (see Table 1.2). However, non-classical features

Classical	Quantum
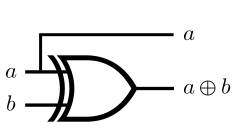	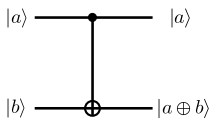

a	b	$a \oplus b$
0	0	0
0	1	1
1	0	1
1	1	0

$\|a\rangle$	$\|b\rangle$	$\|a \oplus b\rangle$
$\|0\rangle$	$\|0\rangle$	$\|0\rangle$
$\|0\rangle$	$\|1\rangle$	$\|1\rangle$
$\|1\rangle$	$\|0\rangle$	$\|1\rangle$
$\|1\rangle$	$\|1\rangle$	$\|0\rangle$

Table 1.2: The classical logic gate XOR acting on two bits and its quantum counterpart, the CNOT gate. Adapted from [36].

can be obtained by quantum gates without classical equivalents that introduce superposition and entanglement between the qubits. Let us the example for the Hadamard gate, noted H, whose action is defined by Table 1.3, that create a superposed state from $|0\rangle$ or $|1\rangle$.

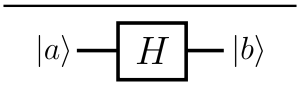

$\|a\rangle$	$\|b\rangle$
$\|0\rangle$	$\frac{1}{\sqrt{2}}(\|0\rangle + \|1\rangle)$
$\|1\rangle$	$\frac{1}{\sqrt{2}}(\|0\rangle - \|1\rangle)$

Table 1.3: The Hadamard gate, that prepares superposed one-qubit states.

Together with a CNOT gate, it becomes possible to create an entangled state that is

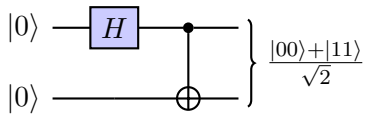

Figure 1.3: An example of a quantum circuit, an Hadamard gate combined with CNOT gate, creating a Bell state.

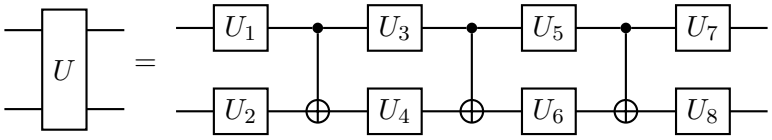

Figure 1.4: Any 2-qubit gate can be decomposed using 3 CNOTs gates and single-qubit unitaries.

truly non-classical. To do so, we create a superposed state with the control qubit whose state determines whether the second qubit's state will be flipped. The state of the second qubit becomes intrinsically linked with the state of qubit 1, as they form an entangled state, as depicted in Fig. 1.3. Table 1.4 shows commonly used quantum gates with their circuit and matrix representations. Some remarks are worth to be mentioned to better undersand their utility. First, any single-qubit unitary can be decomposed as a product of rotations along different axes such that

$$U = e^{i\delta} R_z(\alpha) R_y(\beta) R_z(\gamma). \tag{1.30}$$

Similarly, any two-qubit unitary can be decomposed with at most 3 CNOTs and single-qubit rotations [37] as shown in Fig. 1.4. In general, it is possible to define *universal gate set*, i.e. a set of quantum gates from which any N-qubit unitary can be decomposed with a finite quantum circuit, as a consequence of the Solovay-Kitaev theorem [38]. This tells us that a quantum computer accesses the full power of quantum computation by preparing any state in a finite time. For example, all the single-qubit gates (that can be expressed as 1.30) with the CNOT gate [39] or $\{\text{CNOT}, H, P(\pi/2)\}$ with the T gate forms a universal gate set. Note that the so-called Clifford group generated by $\{\text{CNOT}, H, P(\pi/2)\}$ has the property that if U belongs to the Clifford gate, therefore it maps any tensor product of Pauli matrices (often referred to as a Pauli string) σ into another Pauli string σ' as $U\sigma U^\dagger = P\sigma'$. This feature allows to simulate any quantum circuits containing only gates from the Clifford group in a polynomial time on a classical computer, thanks to the Gottesman-Knill theorem [40]. Therefore, any quantum computation should require non-Clifford gates in order to provide a quantum advantage.

Gate	Symbol	Matrix
Pauli X	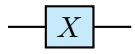	$\begin{pmatrix} 0 & 1 \\ 1 & 0 \end{pmatrix}$
Pauli Y	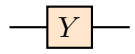	$\begin{pmatrix} 0 & -i \\ i & 0 \end{pmatrix}$
Pauli Z	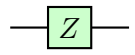	$\begin{pmatrix} 1 & 0 \\ 0 & -1 \end{pmatrix}$
Hadamard	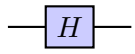	$\frac{1}{\sqrt{2}}\begin{pmatrix} 1 & 1 \\ 1 & -1 \end{pmatrix}$
Phase	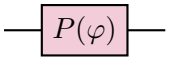	$\begin{pmatrix} 1 & 0 \\ 0 & e^{i\varphi} \end{pmatrix}$
T	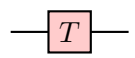	$\begin{pmatrix} 1 & 0 \\ 0 & e^{i\pi/4} \end{pmatrix}$
$R_x(\theta)$	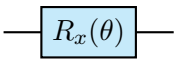	$\begin{pmatrix} \cos(\frac{\theta}{2}) & -i\sin(\frac{\theta}{2}) \\ -i\sin(\frac{\theta}{2}) & \cos(\frac{\theta}{2})) \end{pmatrix}$
$R_y(\theta)$	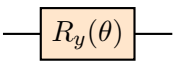	$\begin{pmatrix} \cos(\frac{\theta}{2}) & -\sin(\frac{\theta}{2}) \\ \sin(\frac{\theta}{2}) & \cos(\frac{\theta}{2})) \end{pmatrix}$
$R_z(\theta)$	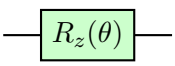	$\begin{pmatrix} e^{-i\theta/2} & 0 \\ 0 & e^{i\theta/2} \end{pmatrix}$
CNOT	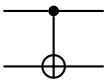	$\begin{pmatrix} 1 & 0 & 0 & 0 \\ 0 & 1 & 0 & 0 \\ 0 & 0 & 0 & 1 \\ 0 & 0 & 1 & 0 \end{pmatrix}$
SWAP	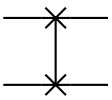	$\begin{pmatrix} 1 & 0 & 0 & 0 \\ 0 & 0 & 1 & 0 \\ 0 & 1 & 0 & 0 \\ 0 & 0 & 0 & 1 \end{pmatrix}$
Toffoli	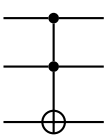	$\begin{pmatrix} \mathbb{1} & 0 & 0 & 0 \\ 0 & \mathbb{1} & 0 & 0 \\ 0 & 0 & \mathbb{1} & 0 \\ 0 & 0 & 0 & X \end{pmatrix}$

Table 1.4: Quantum gates with their symbolic represention and corresponding unitary matrix. Adapted from [41].

1.1.5 Measurement and expectation values

Measurement is the final step in the process of quantum computation. It allows to access the information carried by the superposed and entangled states from the quantum

computer. In quantum mechanics, measurement is the result of the interaction between the quantum system and an external apparatus, which leads to a probabilistic projection of the state. As part of one of the fundamental postulates of quantum mechanics, the measurement can formulated mathematically as follows. Let $|\Psi\rangle$ be the state describing the quantum system. The measurement is defined by a set of measurement operators $\{M_m\}$ where m is a measurement output. Therefore, the probability p_m of obtaining m is defined as

$$p_m = \langle\Psi|M_m^\dagger M_m|\Psi\rangle. \tag{1.31}$$

After the measurement yielding the output m, the system is described by

$$|\Psi_m\rangle = \frac{M_m\,|\Psi\rangle}{\sqrt{p_m}}. \tag{1.32}$$

The sum of the probabilities for the different outputs $\{m\}$ must be equal to 1, leading to the completeness condition:

$$\sum_m p_m = \sum_m \langle\Psi|M_m^\dagger M_m|\Psi\rangle = 1. \tag{1.33}$$

This consists of the foundation of quantum measurement. In practice, to describe the effect of measurement, a less general framework is used: the Projective Operator-Valued Measure (POVM) formalism, where the state undergoes a projection as a result of the measurement. The measurement is described by a set of positive semi-definite hermitian operators $\{\Pi_i\}$ with

$$\sum_i \Pi_i = \mathbb{1}, \tag{1.34}$$

where each operator is associated with a measurment output with probability p_i defined as

$$p_i = \langle\Psi|\Pi_i|\Psi\rangle. \tag{1.35}$$

In the case of pure states, a simple form of POVM consists of a set of projectors $\{\Pi_i\}$ (with $\Pi_i\Pi_j = \delta_{ij}\Pi_i$) associated with a set of states $\{|i\rangle\}$ forming an orthogonal basis. Within this framework, the state $|\Psi\rangle$ or ρ is projected onto a $|i\rangle$ with probability $|\langle i\,|\Psi\rangle\,|^2 = |\langle i|\rho|i\rangle|$.

This projective measurement formalism is an essential element to understand how one can evaluate a physical quantity from a state. A physical quantity is represented by an *observable*, defined by a Hermitian operator, meaning that if O is an observable, then $O^\dagger = O$. An observable can be decomposed in terms of its eigenvalues $\{\lambda_i\}$ and projectors

$\{\Pi_i\}$ onto its different eigenspaces as

$$O = \sum_i \lambda_i \Pi_i. \tag{1.36}$$

The set of projectors $\{\Pi_i\}$ define a projective measurement, the physical quantity O evaluated on the state $|\Psi\rangle$ is the sum of probabilities of the different outputs $\{i\}$ weighted by their associated eigenvalues $\{\lambda_i\}$, resulting into an averaged value $\langle O\rangle$ called *expectation value*, obtained as

$$\langle O\rangle = \sum_i \lambda_i p_i \tag{1.37}$$

$$= \sum_i \lambda_i \langle\Psi|\Pi_i|\Psi\rangle \tag{1.38}$$

$$= \langle\Psi|O|\Psi\rangle. \tag{1.39}$$

The simplest example when measuring the average magnetization of one qubit, described by the Pauli-Z observable, whose eigenvalues are +1 and -1, associated with the projectors

$$\Pi_0 = |0\rangle\langle 0|,\ \Pi_1 = |1\rangle\langle 1|. \tag{1.40}$$

These projectors correspond to projecting the qubit into one of the two computational basis states 0 or 1. The expectation value of Z is evaluated from the probabilities p_0 and p_1 of measuring the qubit in the $|0\rangle$ and $|1\rangle$, as

$$\langle Z\rangle = \langle\Psi|(|0\rangle\langle 0| - |1\rangle\langle 1|)|\Psi\rangle \tag{1.41}$$

$$= |\langle 0|\Psi\rangle|^2 - |\langle 1|\Psi\rangle|^2 \tag{1.42}$$

$$= p_0 - p_1. \tag{1.43}$$

The probability p_i is obtained by sampling the state $|\Psi\rangle$. The state is prepared and measured n times, the output 0 (1) is obtained n_0 (n_1) times. The probability for the output k is then estimated by n_k/n. Fig. 1.5 shows an example of a quantum circuit with a measurement.

For N qubits, we can use tensor products of the one-qubit projectors, such as

$$\Pi_k = \Pi_{k_1} \otimes \cdots \otimes \Pi_{k_N}, \tag{1.44}$$

where k indexes the N qubit states resulting from the tensor product of one qubit states labeled by $\{k_i\}$, $k_i = 0$ or 1. In most quantum devices this is how measurement can be

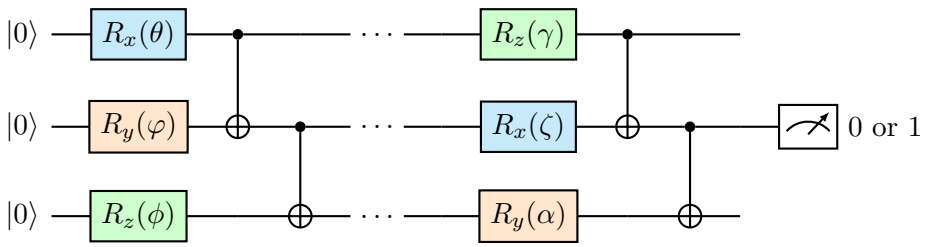

Figure 1.5: An example of a 3-qubit quantum circuit ending by a measurement on the second qubit, that produces an output 0 or 1.

described. Being able to only perform measurements in the computational basis implies that one can only evaluate observables of the form of tensor product of Z-Pauli operators, i.e. $\mathcal{Z} = \otimes_{q\in\mathcal{Q}} Z_q$, where $\mathcal{Q}$ designates a subset of the qubit register containing $N_\mathcal{Q}$ qubits. Its expectation value is obtained by.

$$\langle \mathcal{Z} \rangle = \sum_k s(k) |\langle k|\Psi\rangle|^2 \simeq \sum_k s(k) \frac{n_k}{n}, \tag{1.45}$$

where s is the sign of the bitstring k defined as

$$s(k) = (-1)^{\prod_i k_i}. \tag{1.46}$$

To measure an observable O other than the product of Z operators, the strategy is to find a unitary transformation $\mathcal{B}$ that performs a change of basis to transform O to $\mathcal{Z}$, i.e. $\mathcal{B}^\dagger \mathcal{Z} \mathcal{B} = O$, such that O can be evaluated by applying $\mathcal{B}$ before performing measurements. A simple (although not optimal) approach is to decompose the observable O as as sum of Pauli strings:

$$O = \sum_i \alpha_i \sigma_i, \tag{1.47}$$

where $\sigma_i \in \{\mathbb{1}, X, Y, Z\}^{\otimes N_\mathcal{Q}}$ and $\alpha_i \in \mathbb{C}$. By observing that

$$HZH = X, \text{ and } P(-\frac{\pi}{2}) HZH P(-\frac{\pi}{2}) = Y, \tag{1.48}$$

we can measure any Pauli string by applying the corresponding single-qubit rotations (H to measure X and $HP(-\frac{\pi}{2})$ to measure Y). Note that more efficient strategies can be found by partitioning sets of Pauli strings that can be measured simultaneously (i.e. with a single quantum circuit) based on their commutativities [19]. By summing the estimated expectation values for $\{\sigma_i\}$, we can estimate $\langle O \rangle$.

Measurement basis	Circuit
Pauli Z	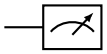
Pauli X	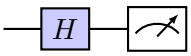
Pauli Y	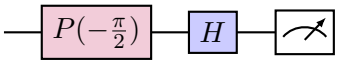

Table 1.5: Circuit to measure a qubit in the different Pauli basis. Adapted from [42]

1.2 Noise, decoherence and NISQ devices

At the heart of quantum computation lies the capacity to design and build a controllable quantum system, which represent a massive conceptual and technical challenge. In particular, its consituable qubits should keep their quantum features over long time scale, while the operations between one or more qubits should be performed at an high level of precision. The DiVincenzio's criteria [43] are often taken as reference requirements for quantum computers. According to them, performing quantum computation should require:

1. "A scalable quantum system with well-characterized qubits", meaning the fabrication of a quantum computer with a high number of qubits is possible.
2. "The ability to initialize the state of the qubits to a simple fiducial state, such as $|000\ldots\rangle$", so that any quantum computation will start with a known initial state.
3. "A long coherence time", meaning that the qubits are sufficiently isolated for their environment to keep their quantum features over long time scales. More precisely, the coherence time should be longer than the running time of a given quantum circuit.
4. "A universal set of quantum gates", to have the capacity to perform any unitary transformation, and therefore access the full potential of quantum computation.
5. "A qubit-specific measurement capability", which makes it possible to query efficiently results from the quantum computation

Different technologies are currently considered and explored in order to build a quantum computer, which has its own advantages and disadvantages with respect to the DiVincenzio's criteria. Amongst the leading technologies, superconducting qubits, built from

Josephson junctions, neutral atoms such as Rydberg atom platforms, using two specific states of manipulable and interacting atoms to act as two-level systems or trapped-ion architecture, similar to neutral atoms, ions trapped into an optical lattice are used as qubits by by isolating two electronic states. Although tremendous and rapid improvements have been performed in the past recent years, current quantum devices still suffer mainly from decoherence. These quantum platforms are often named "Noisy Intermediate Scale Quantum" or NISQ devices [7].

1.2.1 Density matrix and mixed states

To better understand the effect of noise, we can use models that mimic the interaction of qubits with their environment. First, in order to describe our quantum system, we will use a Hilbert $\mathcal{H}_S$. The system being not fully isolated, it interacts with its environment, described by a Hilbert space $\mathcal{H}_E$. As a result of this interaction, it becomes impossible to describe the system S by a quantum state from $\mathcal{H}_S$ but rather a quantum state $|\Psi_{S+E}\rangle$ belonging in $\mathcal{H}_S \otimes \mathcal{H}_E$. However, accessing the full state of the system is impossible as we do not know about the nature of the environment, and can only manipulate and measure the system S. Rather than the full quantum state, we can only access the reduced density matrix ρ of S, formally obtained by tracing out the environment's degrees of freedom:

$$\rho = \mathrm{Tr}_E(|\Psi_{S+E}\rangle\langle\Psi_{S+E}|) \tag{1.49}$$

The density matrix ρ can be for example reexpress with its spectral decomposition

$$\rho = \sum_i p_i |\Psi_i\rangle\langle\Psi_i|. \tag{1.50}$$

The expression in Eq. 1.50 teaches that the system is in a *mixed*, i.e. in a statistical mixture of *pure* states $\{|\Psi_i\rangle\}$ associated with probabilities $\{p_i\}$. The normalization of the state is still conserved, ie $\mathrm{Tr}(\rho) = 1$, but the purity of the state, i.e. how much ρ is mixed, can be measured by $\mathrm{Tr}(\rho^2) \leq 1$ ($= 1$ when pure). The expectation value of an observable O is obtained by

$$\langle O\rangle = \sum_i p_i \langle\Psi_i|O|\Psi_i\rangle \tag{1.51}$$

$$= \mathrm{Tr}(O\rho). \tag{1.52}$$

In terms of Bloch sphere representation, the vector $\vec{n} = (n_x, n_y, n_z)$ representating the

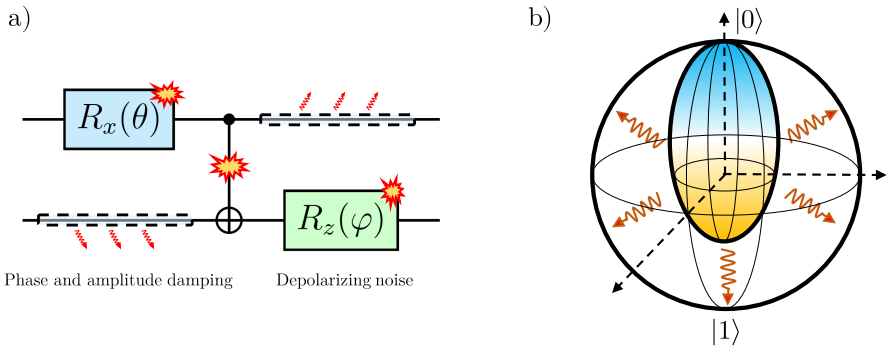

Figure 1.6: (a) Running a quantum circuit on a noisy quantum device can be modelled by channels. Idle qubits loose their coherence by phase and amplitude damping, while acting with gate on qubits also induce errors, that can be modelled by a depolarizing channel. (b) On a single qubit, noise reduces the effective Bloch sphere.

state ρ is defined as $(\mathrm{Tr}(X\rho), \mathrm{Tr}(Y\rho), \mathrm{Tr}(Z\rho))$. For a mixed state, its purity $\mathrm{Tr}(\rho^2) < 1$ translates into $||\vec{n}|| < 1$, meaning that the state corresponds now to a point inside the unit sphere, effectively reducing the computational space.

1.2.2 Noise model

To better grasp the effect of decoherence, we can use simple models that effectively capture quantum noise when running a quantum circuit. We can distinguish between several effects. A useful formalism to describe noise in the operator-sum representation. In the same spirit as Eq. 1.49, we consider that the system along with its environment undergoes a global unitary transformation. After tracing out the environment, we obtain that the density matrix for the system S is evolved and mixed under a set of operators $\{K_k\}$ resulting in an updated density matrix $\mathcal{E}(\rho)$ such that

$$\mathcal{E}(\rho) = \sum_k K_k \rho K_k^\dagger \tag{1.53}$$

The condition of trace preservation implies that $\sum_k K_k^\dagger K_k = \mathbb{1}$.

Let us first consider an idle qubit. We can usually take into account two main phenomena responsible for noise. First, the state $|1\rangle$ is an excited state of the qubit associated with a higher energy than its ground state $|0\rangle$. Therefore, qubits can spontaneously relax

to their lower energy ground state by emitting a photon. This is called *amplitude damping*, as the amplitude associated to state $|1\rangle$ is leaking toward the amplitude of state $|0\rangle$. The following Kraus operators can used to model this noise:

$$K_0^{AD} = \begin{pmatrix} 1 & 0 \\ 0 & \sqrt{1-p^{AD}} \end{pmatrix}, K_1^{AD} = \begin{pmatrix} 0 & \sqrt{p^{AD}} \\ 0 & 0 \end{pmatrix}, \tag{1.54}$$

where he relaxation probability p^{AD} is defined by typical time scale T_1 such that $p^{AD}(t) = 1 - e^{-t/T_1}$, t being the idle time. The relaxation of the qubit into its ground state has for consequence the shrinking of the Bloch sphere to the classical state 0.

Another key phenomena to include is the *phase damping*. Without loss of energy, it corresponds to the loss of quantum information by losing the information of the phase of state $|1\rangle$ with respect to $|0\rangle$. To describe this, we can use the following operators:

$$K_0^{PD} = \sqrt{p^{PD}} \begin{pmatrix} 1 & 0 \\ 0 & 1 \end{pmatrix}, K_1^{PD} = \sqrt{1-p^{PD}} \begin{pmatrix} 1 & 0 \\ 0 & -1 \end{pmatrix}. \tag{1.55}$$

This channel is equivalent to leaving the state invariant with probability p^{PD} flipping the phase of the state $|1\rangle$ by applying a Z gate with a probability $1 - p^{PD}$. Similarly, p^{PD} is defined by a typical time scale T_ϕ, so that $p^{PD} = 1 - e^{-t/T_\phi}$. In terms of the Bloch sphere, losing the information of the phase has the effect of shrinking the Bloch sphere towards the z-axis. The pure dephasing time scale is usually difficult to measure as amplitude damping occurs simultaneously. We often define the decoherence time T_2 (or transverse relaxation time) that combines both phase and amplitude damping as $T_2^{-1} = (2T_1)^{-1} + T_\phi^{-1}$.

Finally, we also need to take into account the errors arising when performing a gate on qubits. The gate imperfections are modeled by a depolarizing channel acting after each gate [44], that we define with

$$K_0^D = \sqrt{1-p}I, K_1^D = \sqrt{\frac{p}{3}}X, K_2^D = \sqrt{\frac{p}{3}}Y, K_3^D = \sqrt{\frac{p}{3}}Z. \tag{1.56}$$

When applying a gate U to a qubit in the state, this channel acting transforms the resulting $\rho \leftarrow U\rho U^\dagger$ leaves the state untouched with probability $1 - p$ or apply one of the Pauli gates with probability $p/3$:

$$\mathcal{E}(\rho) = (1-p)\rho + \frac{p}{3}(X\rho X + Y\rho Y + Z\rho Z). \tag{1.57}$$

Using the decomposition of ρ in the Pauli basis with Eq. 1.18, we can equivalently

rewrite the mixed density matrix as

$$\mathcal{E}(\rho) = (1 - \frac{4p}{3})\rho + \frac{4p}{3}\frac{\mathbb{1}}{2}, \tag{1.58}$$

meaning that the density matrix gets mixed with the maximally mixed state $\mathbb{1}/2$. To model the noise of a n-qubit gate, we take the tensor product of n one-qubit depolarizing channel, or we use global depolarizing noise defined as

$$\mathcal{E}(\rho) = (1 - p)\rho + p\frac{\mathbb{1}}{2^L}, \tag{1.59}$$

with p is here a global error probability. Despite its simplicity, Eq.1.59 gives a simple view on decoherence, where the exact state gets mixed with a completely uncorrelated classically mixed state $\frac{\mathbb{1}}{2^L}$, interpreted as a statistical mixture of all the classical states. Fig. 1.6 summarizes the noise sources occuring when running a circuit and their effects on the Bloch sphere.

2 | Ground State Search with Quantum Computers

2.1 Introduction

This chapter adresses the question of ground state search with quantum computers. Finding the ground states of interacting systems is a challenging endeavor that lies at the heart of quantum mechanics. Accessing them is crucial for understanding the fundamental nature of quantum systems and their properties. In quantum mechanics, the energy of the system is described by an Hamiltonian H, which determines the energy E of a normalized state $|\Psi\rangle$ as $E = \langle H \rangle = \langle \Psi | H | \Psi \rangle$. Therefore, determining the state $|\Psi_0\rangle$ of a system with the lowest energy E_0 can be formulated as an eigenvalue problem:

$$H\,|\Psi_0\rangle = E_0\,|\Psi_0\rangle\,. \tag{2.1}$$

In a general scenario, the Hamiltonian H can be represented with a matrix whose dimensions scales exponentially with the number of degree of freedom of the system of interest ($2^N \times 2^N$ in the case of N interacting spin-1/2's), while a state $|\Psi\rangle$ can be manipulated as a vector storing the amplitudes related to the basis states. Diagonalizing H becomes an exponentially difficult task as the system size increases (as diagonalizing a matrix of size $d \times d$ comes at a cost $\mathcal{O}(d^3)$ [45]). Finding efficient representations for quantum many-body systems is the key point to simulate them. However, quantum computers offer a way to encode and manipulate quantum many-body states in the most natural fashion: by preparing and performing operations on an actual many-body state, realized by a quantum machine, as formulated in Feynman's original idea [46]. Quantum computers make the promise of controlling entangled many-particle states untractable for classical computers because of both the number of qubits involved and the high level of entanglement. On the other hand, accessing such correlated states does not necessarily

imply that we know how to perform a computation, whose output is the desired information, such that the ground state energy of a given Hamiltonian. The field of quantum computation aims at finding algorithms that leverage the power of quantum superposition and entanglement to perform computations out-of-reach of classical algorithms. This encompasses many aspects, from algorithmic complexity to practical considerations, such as noise resilience or quantum circuit compilations tailored for a given hardware. In the case of interacting quantum systems, a number of algorithms have been proposed for both the currently non-existing quantum error-corrected devices and the currently available NISQ devices [7].

In this chapter, we describe two prototypical quantum algorithms tailored for the ground state search for quantum interacting systems. The first one, the Quantum Phase Estimation, is the historical fault-tolerant algorithm allowing to access the eigenvalues of a unitary transformation. The second, the Variational Quantum Eigensolver [18, 19], is the most prominent NISQ algorithm, using a hybrid quantum-classical scheme, delegating only a part of the algorithm to the quantum computer. This is the latter that the rest of the chapter will be focused on. We use an 8-site 1D Hubbard model as a benchmark problem for this contemporary quantum algorithm. To be more precise, we employ the VQE with the Variational Hamiltonian Ansatz (VHA) [47, 48] as our parameterized quantum circuit. The VHA leverages an ansatz that is inspired by the Hubbard Hamiltonian itself and an adiabatic way of thinking to construct the trial wavefunction. Adopting a condensed matter physics perspective, we try to evaluate how much of the underlying physics is preserved by this ansatz that respects all physical symmetries of the system. Our simulations incorporate a realistic noise model, to quantify how much is the algorithm influenced by pure dephasing, spin relaxation, and gate errors and to compare with experimental results from the IBM Quantum's `ibmq_quito` device [6]. Furthermore, we attempt an error mitigation strategy called the zero-noise extrapolation [49, 50] - a measurement of an observable with artificially modulated noise levels followed by an extrapolation to the zero-noise case, alongside post-selection.

The adiabatic evolution-inspired VHA was first introduced in Ref. [47] and has been investigated for Hubbard models in Refs. [48, 51, 52]. Furthermore, studies of spin systems were conducted in Ref. [53] as well as optimization studies with the well-studied Quantum Approximate Optimization Algorithm (QAOA) which share the same structure (proposed before VHA in Ref. [54]). The study conducted here advances that of Ref. [48] with a more elaborate noise model and discussions of potential noise-mitigation strategies. Furthermore, spin correlations, noise mitigation, and a broader range of U are discussed as compared to Ref. [51] and focus on how well certain variables are captured as compared to resource estimation as in Ref. [52].

Our findings suggest that different quantities of the physical system require different levels of ansatz complexities. Namely, even for an ansatz of relatively low depth doubly occupied site number and energy are predicted at a satisfactory level. On the other hand, long-range spin correlations are much more sensitive to the infidelities of the trial solution - even a 90% fidelity is insufficient to capture the correct long-range spin-spin behavior. Finally, zero-noise extrapolation strongly mitigates the effects of quantum noise, although we are only able to validate this for a 2-site Hubbard model (4-qubit simulation).

This chapter is organized as follows, in Section 2.2 we give a brief description of the famous Quantum Phase Estimation, whose qubit number and circuit depth motivate the Variational Quantum Eigensolver, introduced in Section 2.3, as a more noise resilient algorithm for practical use of quantum computers, with a description of specific circuit used her. Then, in Section 2.4 we describe the model used here as a prototypical interacting model for fermion, and how this can fermionic problem can be mapped onto a qubit problem. In Section 2.6 we show noiseless simulations of VQE for an 8-site one-dimensional Hubbard model with energy, fidelity, doubly occupied site number, and spin-spin correlations obtained for different circuit depths. Finally, in Section 2.7 we discuss the noise model along with error mitigation and experimental results. This work is based on [55].

2.2 The Quantum Phase Estimation

In the quest of finding ground states with quantum computers, the quantum phase estimation (QPE) algorithm was one the most important algorithm in quantum computing. Introduced in 1995 [56], the QPE algorithm is commonly used as quantum subroutine in other algorithms, such as the Shor algorithm [8, 9] for prime factorization or the HHL algorithm [57] for solving linear systems of equations, and is a major contribution in the field of quantum computation. The primary goal of the QPE is to estimate the eigenvalue of an eigenvector $|\Psi\rangle$ of a unitary operator U. As U is a unitary transformation, one can write $U|\Psi\rangle = e^{i2\pi\varphi}|\Psi\rangle$, where $\varphi \in [0, 1[$ is a phase. The QPE algorithm allows to estimate this phase φ to an arbitrary level of precision ϵ. Here we give a description of the QPE algorithm, inspired from [30].

The QPE algorithm assumes that one knows how to prepare the n-qubit state $|\Psi\rangle$ as well as to perform U^{2^m} $(m \in \mathbb{N})$ operations controlled by a auxillary qubit, called ancilla qubit. The main idea of the QPE algorithm is that a physical register of qubits where $|\Psi\rangle$ is encoded gets entangled with an ancilla register, which will encode the information about the phase φ. The ancilla register, composed of t qubits, is put in an equal superposition of all the computational states by applying Hadamard gates on each of the t qubits, while $|\Psi\rangle$ is prepared on the physical register. Then, a series of U^{2^m} operations are performed,

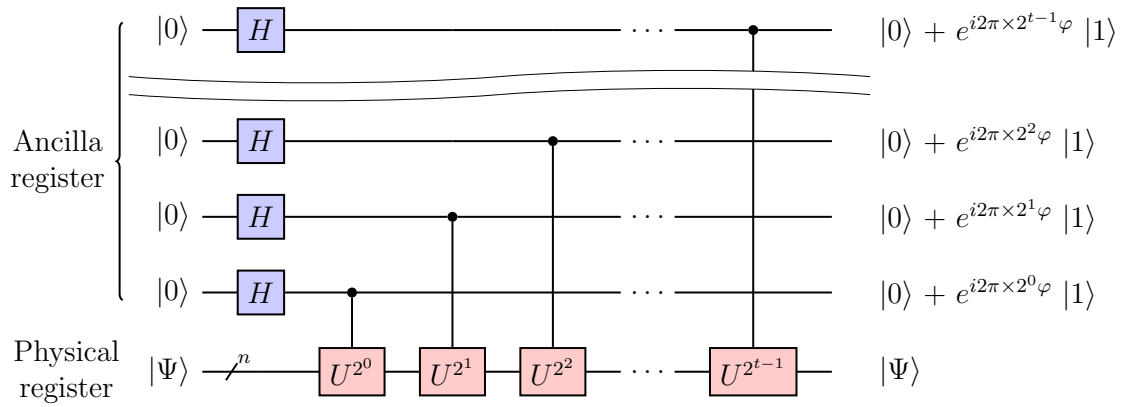

Figure 2.1: The Quantum Phase estimation circuit, adapted from [30].

acting on the physical register but controlled by one qubit of the ancilla register, as shown in Fig. 2.1. The resulting state is a product state between the two registers. The ancilla state $|\Psi_t\rangle$ reads as

$$|\Psi_t\rangle = \frac{1}{2^{t/2}}\left(|0\rangle + e^{i2\pi 2^0\varphi}\,|1\rangle\right)\left(|0\rangle + e^{i2\pi 2^1\varphi}\,|1\rangle\right)\ldots\left(|0\rangle + e^{i2\pi 2^{t-1}\varphi}\,|1\rangle\right). \tag{2.2}$$

By labelling the computational states $|\sigma_1\sigma_2\ldots\sigma_t\rangle$ by the corresponding integer $k = \sum_{i=1}^{t}\sigma_i 2^{i-1}$, we can rewrite Eq. by

$$\begin{aligned}|\Psi_t\rangle &= \frac{1}{2^{t/2}}\sum_{k=0}^{2^t-1} e^{i2\pi k\varphi}\,|k\rangle \\ &= \frac{1}{2^{t/2}}\sum_{k=0}^{2^t-1} e^{i2\pi k\tilde{\varphi}/2^t}\,|k\rangle\,, \quad \text{with } \tilde{\varphi}\equiv\varphi\times 2^t.\end{aligned} \tag{2.3}$$

By looking at Eq. 2.3, we see that the expression of the state resembles a discrete Fourier transform. In the discrete Fourier transform, an array of complex numbers $\{x_j\}_{j=0}^{N-1}$, where N is the sample size, is transformed to another array $\{y_k\}_{k=0}^{N-1}$ by the following operation:

$$y_k = \frac{1}{\sqrt{N}}\sum_{j=0}^{N-1} e^{i2\pi kj/N}x_j. \tag{2.4}$$

In fact, $|\Psi_t\rangle$ can be seen as a quantum Fourier transform (QFT). The quantum Fourier transform performs a similar transformation but acts as a unitary transformation on the basis states. From as specific state from the computational basis $|x\rangle$, it returns the fol-

lowing quantum superposition:

$$\mathrm{QFT}\,|x\rangle = \frac{1}{\sqrt{N}} \sum_{k=0}^{N-1} e^{i2\pi kx/N}\,|k\rangle\,. \tag{2.5}$$

Let us assume for simplicity that $\tilde{\varphi} = \varphi \times 2^t$ is an integer, ie φ has an exact binary decomposition with t bits, such as $\varphi = \varphi_1 \times 1/2^1 + \varphi_2 \times 1/2^2 + \cdots + \varphi_t \times 1/2^t$, where $\{\varphi_i\} \in \{0,1\}^t$. Therefore, by identifying N as 2^t, we understand the resulting state of the ancilla register is the quantum Fourier transform of the state $|\varphi\rangle = |\varphi_1\varphi_2 \ldots \varphi_t\rangle$:

$$|\Psi_t\rangle = \mathrm{QFT}\,|\varphi\rangle\,. \tag{2.6}$$

As QFT is a unitary transformation, we can represent it with a circuit representation, as well as for its inverse transformation $\mathrm{QFT}^\dagger$. As a matter of fact, one can find an efficient circuit performing QFT with $\mathcal{O}(t^2)$ gates [30]. Therefore, by applying $\mathrm{QFT}^\dagger$ on the ancilla register, one retrieves the product state $|\varphi\rangle$, and by a simple measurement in the computational basis, we evaluate φ. Let us now suppose that the phase φ cannot be decomposed with t bits, such as $2^t\varphi = a + 2^t\delta$, where a is the closest integer to φ and $|2^t\delta| \leq 1/2$. The QPE algorithm gives an estimation of $\tilde{\varphi}$ up to a precision $1/2^t$, and probability of measuring the correct output (corresponding to the closest integer to $\tilde{\varphi}$) is equal to $\frac{1}{4^t}|\frac{1-e^{i2\pi 2^t\delta}}{1-e^{i2\pi\delta}}|^2$.

However, the QPE can have another purpose than the sole evaluation of the eigenvalue $e^{i2\pi\varphi}$: it can also be used as a projection protocol. So far, we have assumed that we know how to prepare the eigenvector of $|\Psi\rangle$. In practice, given an arbitrary unitary matrix U, the task of preparing a given eigenstate is highly non-trivial. A more reasonable requirement is that we know how to prepare an approximate state $|\Psi_{\mathrm{approx}}\rangle$, that we could write as a superposition of our state of interest $|\Psi_0\rangle$ and the other eigenstates of U:

$$|\Psi_{\mathrm{approx}}\rangle = \alpha_0\,|\Psi_0\rangle + \sum_{i\geq 1} \alpha_i\,|\Psi_i\rangle\,,\ \text{with} \sum_{i\geq 0} |\alpha_i|^2 = 1. \tag{2.7}$$

In these conditions, the resulting state after applying the QPE algorithm is still a superposition of all the eigenstates $\{|\Psi_i\rangle\}$, but each of these eigenstates becomes entangled with the ancilla register, with a state containing the information about their respective phase. In a case where we have enough ancilla qubits to encode exactly the binary decomposition of the phases, we obtain the following final state:

$$|\Psi_{\mathrm{final}}\rangle = \alpha_0\,|\varphi_0\rangle\,|\Psi_0\rangle + \sum_{i\geq 1} \alpha_i\,|\varphi_i\rangle\,|\Psi_i\rangle \tag{2.8}$$

Therefore, by performing a measurement of the ancilla qubits, one gets the desired phase φ_0 with a probability $|\alpha_0|^2$. Maybe most interestingly, by looking at Eq. 2.8, we see that the physical qubit register is projected onto the desired state $|\Psi_0\rangle$. Therefore, the QPE can also be used as a projection algorithm.

The QPE is particularly appealing from a quantum many-body physics perspective. By taking the unitary matrix $U = e^{iHt}$, where H is the Hamiltonian of quantum systems of interest, for eg. an interacting spin system or chemistry problems, one can use the QPE algorithm to both evaluate the energy spectrum of the system as well as projecting the initial state onto the ground state or an excited state, from which one can measure physical properties. The required depth of the QPE scales as $\mathcal{O}(1/\epsilon)$, while a number of repetitions $\mathcal{O}(1/|\alpha_0|^2)$ is required to successfully obtain φ_0. For ground state determinations, the QPE has raised a lot of hopes for quantum computation in the fault-tolerant regime, as its scaling seems favorable compared to an exact classical solution, having assumed a generic exponential cost. However, two main problems remain for the practical implementation of the QPE algorithm. First, preparing an initial state that possesses a finite overlap with the eigenstate of interest is not a trivial task. The scaling with respect to the problem size may also depend on the size of the problem, and, in an asymptotic limit, the overlap of the prepared state can decay exponentially. This is often referred to as the orthogonality catastrophe [58, 59]. Second, the large number of gates required to perform the QPE circuit prevents any computation on a quantum computer suffering from noise. The latter encourages the exploration of alternative ways to utilize a quantum computer prior to the potential fault-tolerant era. This drives the search for practical quantum algorithms capable of accomplishing valuable computations using fewer quantum resources.

2.3 Variational Quantum Eigensolver

2.3.1 Description of the algorithm

As we have seen in the previous section, designing useful quantum algorithms must answer the following questions: how does it scale and can we realistically implement it? The Variational Quantum Eigensolver (VQE) focuses mainly on answering the second question. First introduced and experimentally demonstrated in [18], the VQE algorithm was presented as an alternative to the QPE algorithm as it proposes to a more resource-efficient use of the quantum device. Its demonstration brought a lot of enthusiasm around noisy quantum devices and was an important starting point in the field of hybrid quantum-classical algorithms and variational quantum algorithms.

The VQE method is a variational approach to the ground state search problem, relying

on the Ritz (or variational) principle. Let $|\Psi\rangle$ be any N-qubit quantum state and H an N-qubit Hamiltonian. In order to access the ground state of H, we seek to find $|\Psi_0\rangle$ which corresponds to the eigenvector of H with the lowest eigenvalue E_0. Therefore, the variational principle reads as

$$\frac{\langle\Psi|H|\Psi\rangle}{\langle\Psi|\Psi\rangle} \geq E_0 \tag{2.9}$$

This simple inequality guarantees us that minimizing the energy of a normalized state $|\Psi(\boldsymbol{\theta})\rangle$ parametrized by $\boldsymbol{\theta}$ can only bring us closer to the true ground state energy E_0, and allows to approximate $|\Psi_0\rangle$. This is upon this principle that variational approaches for many-body physics are built. A prototypical example is the Hartree-Fock approach for interacting electrons [60, 61, 62], where a product single-particle wavefunction is optimized. Later, variational Monte Carlo simulations have been a successful technique in order to approximate ground states of interacting systems [63], using for instance, the Jastrow factor [64] as a trial wave function. The selection of the variational wave function (or ansatz) is closely connected to the accuracy of the results, but in these classical approaches, it is important to maintain its tractability.

The VQE algorithm uses the same principle. It proposes to use a quantum computer to prepare the trial state, offering the possibility to use quantum states that are not representable classically. The VQE algorithm commonly has the following structure:

1. An initial state $|\Psi_0\rangle$ is prepared on the quantum computer.
2. Subsequently, one applies a variational circuit $\mathcal{U}(\boldsymbol{\theta})$, dependent on a set of variational parameters $\boldsymbol{\theta}$, yielding a variational state $|\Psi(\boldsymbol{\theta})\rangle = \mathcal{U}(\boldsymbol{\theta})|\Psi_0\rangle$.
3. After choosing a set of initial parameters $\boldsymbol{\theta}_0$, we prepare $|\Psi(\boldsymbol{\theta}_0)\rangle$ and measure the corresponding energy $E(\boldsymbol{\theta}_0) = \langle\Psi(\boldsymbol{\theta}_0)|H|\Psi(\boldsymbol{\theta}_0)\rangle$.
4. Based on the energy, a classical minimizer will optimize the parameters $\boldsymbol{\theta}$ until it converges to a minimal energy.

VQE is a hybrid quantum-classical scheme. While QPE performs the entire computation of the eigenvalue computation and eigenvector projection, VQE delegates only the state preparation of the variational state to the quantum computer thanks to a parameterized quantum circuit $\mathcal{U}$ that depends on parameters or angles $\boldsymbol{\theta}$. By sampling the quantum state, one can evaluate the expectation value of the Hamiltonian of interest. Fig. 2.2 summarizes the algorithm. What makes VQE particularly suited to NISQ devices lies in the choice of the variational circuit $\mathcal{U}$. By choosing a short circuit, suited to a given hardware, VQE allows one to obtain results from a noisy device, with the hope to mitigate errors thanks to the flexibility of the variational parameters. As mentioned earlier, the

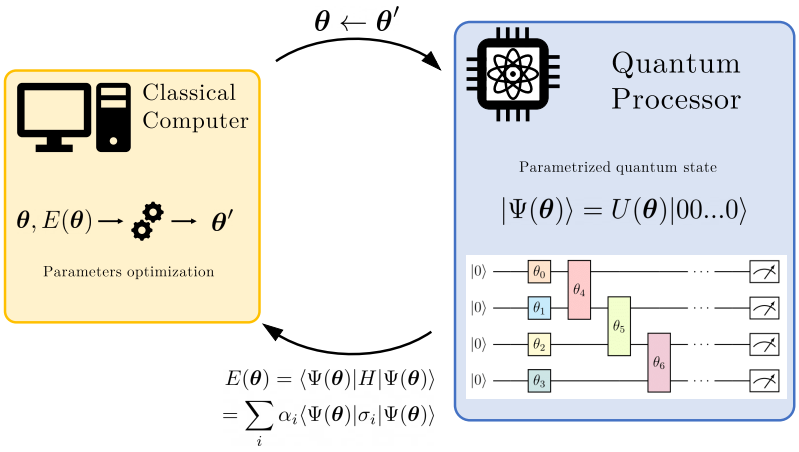

Figure 2.2: The Variational Quantum Eigensolver consists in preparing a trial state $|\Psi(\boldsymbol{\theta})\rangle$ on a quantum computer thanks to a parametrized quantum circuits. The energy $E(\boldsymbol{\theta})$ can be evaluated by performing measurements. Then, a classical computer optimizes the parameters to minimize the energy, until convergence or a stopping criterion is reached.

VQE algorithm was first both proposed and experimentally realized in [18] by performing the simulation of the He-H molecule using two qubits from a photonic processor. The original plot showing the experimental data is shown in Fig. 2.3.

2.3.2 Parametrized quantum circuits as ansätze

The choice of the parameterized circuit is essential in the VQE procedure. Two key elements need to be taken into account when selecting the type of parameterized circuit: the ability to produce the ground state with sufficiently high fidelity, and the implementability of the circuit on contemporary hardware. These two requirements are intertwined due to the limited length, connectivity, and qubit number current-day quantum circuits can have, but also the number of variational parameters a classical optimizer can handle. We can usually distinguish between two strategies when designing an ansatz: 1) the so-called hardware efficient ansätze [65, 66] prioritizes the implementability of the quantum circuits, by using short circuits with two-qubit gates which can be naturally performed by the device and taking into account to its topology. Fig. 2.4 shows an example of such a circuit. Although providing satisfying results on problems that require a small number of qubits, this approach often fails to scale to larger problems and can suffer from optimization barren plateaus [67]. 2) Numerous approaches proposed problem-inspired ansätze which produces variational states from relevant subspaces [68, 69, 70, 71, 72, 73]. Built from physical arguments, they often have better expressivity as they produce meaningful states by requiring more costly circuits. The circuit in Fig. 2.5 is an example

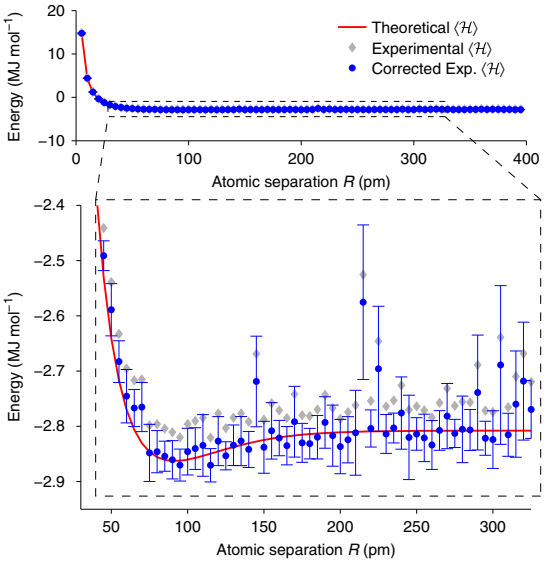

Figure 2.3: The first VQE simulation, demonstrated on a photonic processor. The computation uses two qubits to encode a variational state representing the He-H molecule, and uses VQE to estimate the energy of the molecule as a function of the distance between the two atoms. Taken from [18].

of such circuits. Furthermore, adaptive schemes have been proposed to reduce the circuit length of those methods [74, 75].

2.3.3 From adiabatic preparation to the Variational Hamiltonian Ansatz

Let us now present the thinking behind constructing a VHA trial solution [47, 48, 51, 52] inspired by the Hamiltonian of the problem itself. Observe two Hamiltonians, H_0 and H_f. H_0 corresponds to an eigenproblem that is easily solvable and H_f to a problem that is difficult to solve. The basic idea in adiabatic evolution is to prepare the ground state $|\Psi_0\rangle$ corresponding to the initial Hamiltonian H_0. Then, one can evolve the initial state in time T described by the following time-dependent Hamiltonian

$$H(s) = (1-s)H_0 + sH_f, \text{ with } s(t=0) = 0 \text{ and } s(t=T) = 1 \tag{2.10}$$

If the evolution rate is slow enough with respect to the gap of the system, Fock's adiabatic theorem guarantees that

$$|\Psi(t)\rangle = \mathcal{T} e^{-i\int_0^t H(s(\tau))d\tau} |\Psi_0\rangle \tag{2.11}$$

(where $\mathcal{T}$ is the time-ordering operator) remains in the ground state of the instantaneous Hamiltonian $H(s)$.

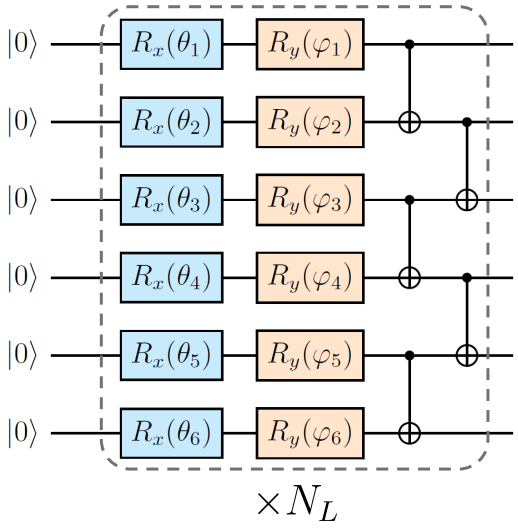

Figure 2.4: An example of hardware efficient parameterized circuit. The quantum circuit is typically organized in a layered fashion, using single-qubit rotations that are easy to implement on actual device, and CNOT gates as entangling gates to increase the state complexity. The connectivity is simple and usually respect the hardware topology. One typical feature is a high number of parameters, aiming to compensate the lack of expressivity of the circuit.

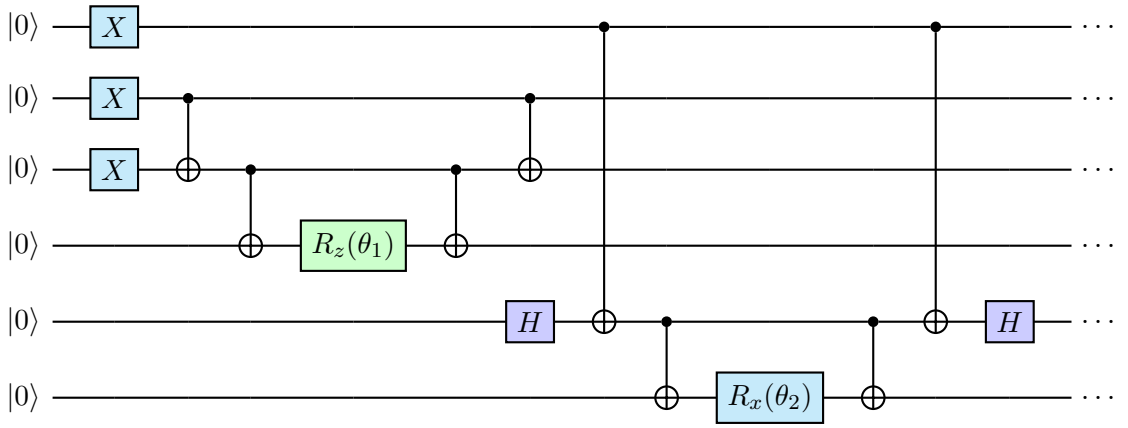

Figure 2.5: An example of a more elaborated anzatz. The circuit corresponds to specific operations, corresponding for example to evolving the state in a fermionic picture. These circuits can be motivated by physical arguments but not by practical considerations. They can involve multi-qubit gates acting on disconnected qubits, leading to a larger circuit cost. In this example, as state $|111000\rangle$ is evolved under $e^{i\frac{\theta_2}{2}Z_1X_5X_6}e^{i\frac{\theta_1}{2}Z_2Z_3Z_4}$.

In general, and on a quantum computer, the time-evolution operator can be approximated with a first-order Trotter-Suzuki [76] approximation by dividing the integration

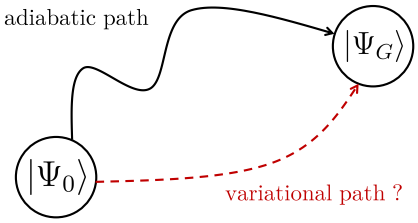

Figure 2.6: Starting by the ground state of H_0, $|\Psi_0\rangle$, that can be easily prepared, the VHA circuit resembles the time evolution propagator but provides a potential shortcut to the ground state of interest $|\Psi_G\rangle$ compared to the adiabatic path.

over time into N time step of duration $\Delta\tau$ so that $T = N\Delta\tau$:

$$\mathcal{T}e^{-i\int_0^T H(s(\tau))d\tau} = \prod_{n=1}^{N} e^{-iH(s(n\Delta\tau))\Delta\tau} \tag{2.12}$$

$$\simeq \prod_{n=1}^{N} e^{-i(H_0(1-s(n\Delta\tau))+H_f s(n\Delta\tau))\Delta\tau} \tag{2.13}$$

Secondly, we decompose H into non-commuting parts $\{H^\alpha\}$: $H = \sum_\alpha H^\alpha$. The terms contained in H^α should commute among each other in order to implement them simultaneously. By using again the Trotter-Suzuki approximation, we obtained the following circuit:

$$\mathcal{T}e^{-i\int_0^T H(s(\tau))d\tau} \simeq \prod_{n=1}^{N}\prod_{\alpha} e^{-iH_0^\alpha(1-s(n\Delta\tau))\Delta\tau}\prod_{\beta} e^{-iH_f^\beta s(n\Delta\tau)\Delta\tau}. \tag{2.14}$$

This scheme allows to perform an approximate adiabatic evolution with a quantum computer. If considering a fermionic problem, one would need to map the fermionic operator to qubit operators.

However, to respect the adiabatic criterion long evolution times are required leading to long circuits beyond the reach of NISQ devices. In order to shortcut adiabatic paths, as depicted in Fig. 2.6, VHA replaces the time steps by variational parameters, with the hope of reducing the circuit depth needed to obtain satisfying states. Fig. 2.7 summarizes

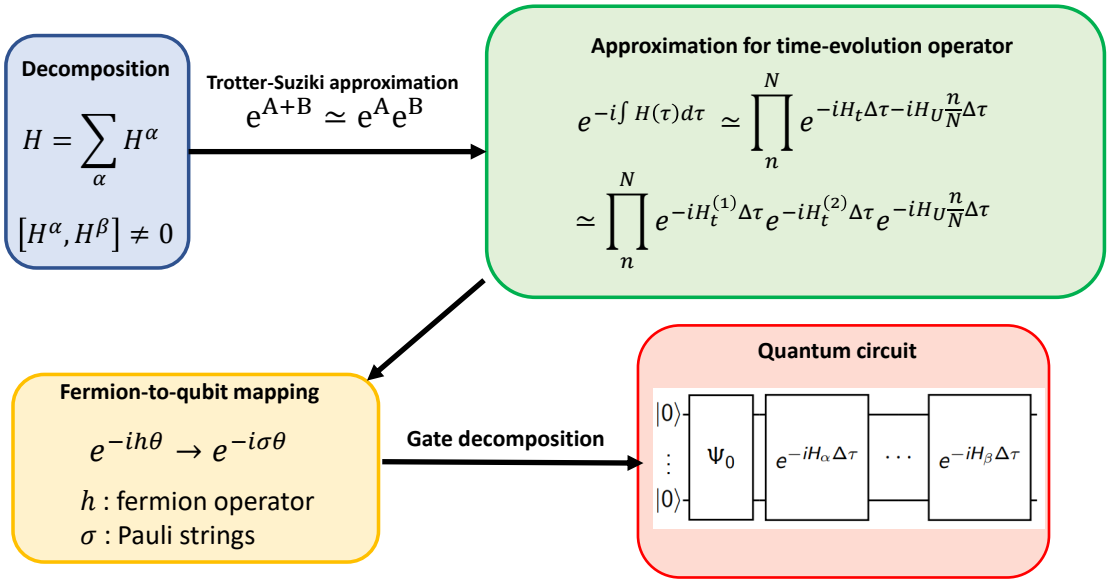

Figure 2.7: The process to perform adiabatic time evolution on a quantum computer for preparing fermionic ground states.

the procedure. The ansatz can be formulated by the following:

$$\mathcal{U}(\boldsymbol{\theta}) = \prod_{n=1}^{N_L} \prod_{\alpha} e^{-iH_0^\alpha \theta_n^\alpha} \prod_{\beta} e^{-iH_f^\beta \theta_n^\beta}, \tag{2.15}$$

where, N_L is the number of layers, and $\boldsymbol{\theta}$ are the variational parameters.

2.4 An benchmark for interacting fermions

2.4.1 A study-case: one-dimensional Hubbard model

The Hubbard model [77] is one of the most studied problems in condensed matter physics. Elegant and seemingly simple it has been the starting point in studying high-temperature superconductivity [78] and metal-to-insulator transitions [79], just to name a few. In the Hubbard model, electrons are assumed to hop between neighboring atomic sites in the lattice. This hopping term describes the kinetic energy of the electrons and is responsible for their mobility. The model also includes an interaction term, known as the on-site Coulomb repulsion. This term accounts for the fact that when two electrons with opposite spins occupy the same atomic site, there is a repulsive interaction between them due to the Coulomb force, as summarized in Fig. 2.8. Although the Hubbard model

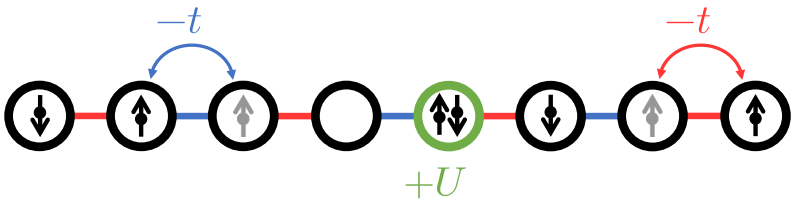

Figure 2.8: The Hubbard Hamiltonian describes electrons hopping between neighboring sites and interacting through Coulomb repulsion when on the same site. In order to use the structure of the Hamiltonian for a quantum variational ansatz, we can distinguish between three non-commuting parts: the hopping Hamiltonian between alternating pairs of sites (in blue and red), and the onsite interaction (in green).

is analytically solvable in one dimension with the famous Bethe ansatz [80], a solution in two and three dimensions is generally unknown and has been the focus of half of a century of numerical studies [81, 82].

Let us consider now the case of the 1D Hubbard model, described by the following Hamiltonian

$$H = -t \sum_{i\sigma} \left(c^\dagger_{i\sigma} c_{i+1\sigma} + \text{h.c.} \right) + U \sum_i \left(n_{i\uparrow} - \frac{1}{2} \right) \left(n_{i\downarrow} - \frac{1}{2} \right). \tag{2.16}$$

For the Hubbard Hamiltonian and in the context of trying to determine its ground state with adiabatic methods, or with the variational quantum circuits described earlier, one can choose H_0 to be the free fermion Hamiltonian $H_t = -t \sum_{i\sigma} (c^\dagger_{i\sigma} c_{i+1\sigma} + c^\dagger_{i+1\sigma} c_{i\sigma})$ and the final Hamiltonian to be the full Hubbard Hamiltonian, which corresponds to the situation of slowly increasing the interaction strength U in the system. While a one-body state can be in principle efficiently prepared on a quantum computer [83, 84, 85], the variational circuit can be formulated by:

$$\mathcal{U}(\boldsymbol{\theta}) = \prod_{n=1}^{N_L} e^{-iH_t^{(2)}\theta_n^2} e^{-iH_t^{(1)}\theta_n^1} e^{-iH_U\theta_n^U}. \tag{2.17}$$

with $H_U = U \sum_i \left(n_{i\uparrow} - \frac{1}{2} \right) \left(n_{i\downarrow} - \frac{1}{2} \right)$, $H_t^{(1)} = \sum_{i\in\text{even},\sigma} \left(c^\dagger_{i\sigma} c_{i+1\sigma} + \text{h.c.} \right)$, and $H_t^{(2)} = \sum_{i\in\text{odd},\sigma} \left(c^\dagger_{i\sigma} c_{i+1\sigma} + \text{h.c.} \right)$. Fig. 2.9 shows a schematic of one layer of the ansatz.

2.4.2 Encoding fermionic states into qubits

So far, we have considered interacting electrons, that are fermions and obey the Fermi-Dirac statistic. A system of N electronic orbitals (indexed by i) can be described by a Fock space constructed for tensor products of the single-particle Hilbert space. A useful

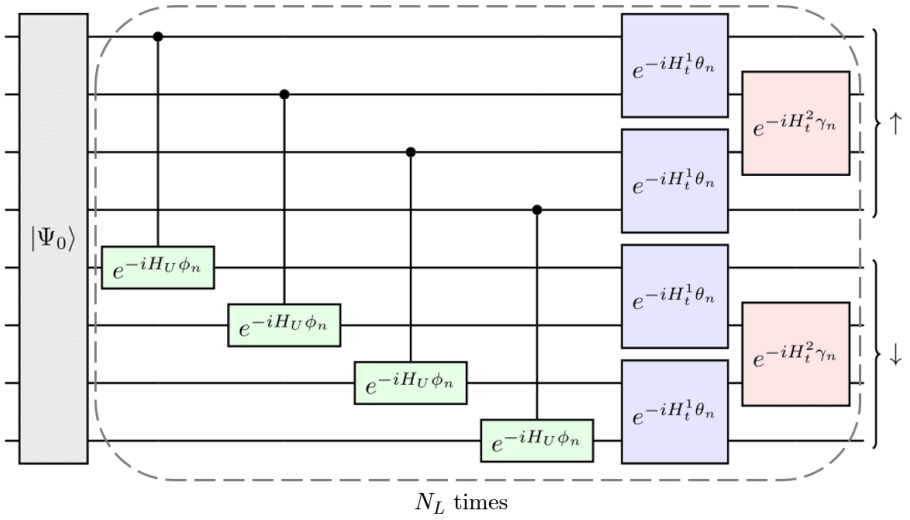

Figure 2.9: One layer for VHA, where $\mathcal{U}_u(\theta) = e^{-iH_U\theta}$, $\mathcal{U}_h^1(\theta) = e^{-iH_t^{(1)}\theta}$, and $\mathcal{U}_h^2(\theta) = e^{-iH_t^{(2)}\theta}$.

basis to span the Fock space is the occupancy number basis, which is built from the states

$$|\{n_i\}\rangle = |n_1, n_2, \ldots, n_N\rangle\,, \tag{2.18}$$

with n_i indicates the number of particles in the single-particle orbital i. In the case of fermions, $n_i = 0$ or 1, as a consequence of Pauli's exclusion principle. In the second quantization, we use creation and annihilation operators to act on many-body states. Their actions are to create or destroy a particle in a single-particle state i. We note $c_i^\dagger$ and c_i the creation and annihilation operator associated with the orbital i. Therefore, we can construct $|\{n_i\}\rangle$ as

$$|\{n_i\}\rangle = \prod_i (c_i^\dagger)^{n_i} |\text{vac}\rangle\,, \tag{2.19}$$

with $|\text{vac}\rangle$ is the vacuum of particles. The Fermi-Dirac statistic dictates that the exchange of two fermions changes the sign of the total wavefunction. As a result, the creation and annihilation operators must respect the following anti-commutation rules:

$$\{c_{i\sigma}, c_{j\sigma'}\} = 0, \tag{2.20}$$

$$\{c_{i\sigma}^\dagger, c_{j\sigma'}^\dagger\} = 0, \tag{2.21}$$

$$\{c_{i\sigma}, c_{j\sigma'}^\dagger\} = \delta_{ij}\delta_{\sigma\sigma'}. \tag{2.22}$$

In order to use a qubit-based quantum computer to solve a fermionic problem, one needs to map the fermionic operators onto qubit (or spin-1/2) operators. This fermion-

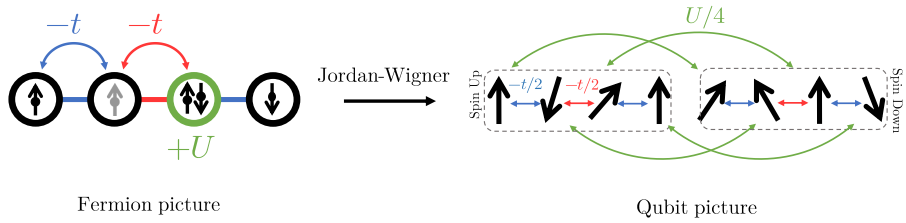

Figure 2.10: The Jordan-Wigner maps fermion into qubits. For each spin-orbital, a qubit is used to encode its occupancy. As a result, the Hubbard model with N sites can be mapped to a Hamiltonian of interacting spins with non-local interactions. For instance, in one dimension, the fermionic chain is mapped onto spins on a ladder.

to-qubit mapping must contain two features: 1) it should encode the occupancy of the fermionic state while 2) conserving the anti-commutation properties of the fermionic operators. A natural encoding, resulting from Eq. 2.18, would be to use one qubit to encode the occupancy of a given spin-orbital (i, σ): if the spin-orbital is occupied by an electron, the qubit is put in the state $|1\rangle$, while if it is empty, the qubit is set to the $|0\rangle$ state. Therefore, the spin raising and lowering operators $S^+ = \frac{X-iY}{2}$ and $S^- = \frac{X+iY}{2}$, which perform the transition between the $|0\rangle$ and $|1\rangle$ states. However, the anti-commutation rule remains to be included. The Jordan-Wigner [86] transformation offers a simple way to use this encoding while incorporating the fermionic features. First, one needs to choose an ordering for the different one-body states. For a Hubbard chain of length N, we choose to index the states by site index, the N first being attributed to spin-up, the N second for spin-down states, so that $c^\dagger_{i\uparrow} = c^\dagger_i$ and $c^\dagger_{i\downarrow} = c^\dagger_{i+N}$. The anti-commutation is encoded by attaching Z-strings to the raising and lowering spin operators. We express the creation and annihilation operators as follows:

$$c_i^\dagger = \otimes_{j<i} Z_j \otimes \begin{pmatrix} 0 & 1 \\ 0 & 0 \end{pmatrix} = \otimes_{j<i} Z_j \otimes \frac{X_i - iY_i}{2} \tag{2.23}$$

$$c_i = \otimes_{j<i} Z_j \otimes \begin{pmatrix} 0 & 0 \\ 1 & 0 \end{pmatrix} = \otimes_{j<i} Z_j \otimes \frac{X_i + iY_i}{2} \tag{2.24}$$

This allows us to reformulate our N-site electronic Hamiltonian as a $2N$ spin-1/2 Hamiltonian, as shown in Fig. 2.10, as:

$$H = -\frac{t}{2}\sum_{i=1}^{N-1} X_iX_{i+1} + Y_iY_{i+1} - \frac{t}{2}\sum_{i=N}^{2N-1} X_iX_{i+1} + Y_iY_{i+1} + \frac{U}{4}\sum_{i=1}^{N} Z_iZ_{i+N} \tag{2.25}$$

Having express fermionic operators into Pauli strings, one can rewrite the operator

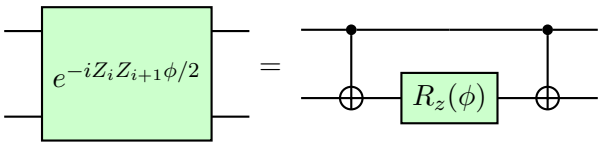

Figure 2.11: Gate decomposition for $e^{-iZ_iZ_{i+1}\phi/2}$.

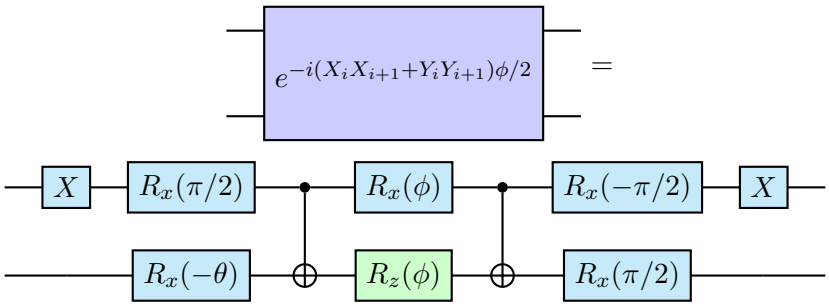

Figure 2.12: Gate decomposition for $e^{-i(X_iX_{i+1}+Y_iY_{i+1})\phi/2}$.

contained in the ansatz:

$$e^{-i(c_i^\dagger c_{i+1}+c_{i+1}^\dagger c_i)\theta} = e^{-i(X_iX_{i+1}+Y_iY_{i+1})\theta/2} = \begin{pmatrix} 1 & 0 & 0 & 0 \\ 0 & \cos(\theta) & -i\sin(\theta) & 0 \\ 0 & -i\sin(\theta) & \cos(\theta) & 0 \\ 0 & 0 & 0 & 1 \end{pmatrix}, \quad (2.26)$$

$$e^{-i(n_i-\frac{1}{2})(n_{i+N}-\frac{1}{2})\phi} = e^{-iZ_iZ_{i+N}\phi/4} = \begin{pmatrix} e^{-i\phi/4} & 0 & 0 & 0 \\ 0 & e^{i\phi/4} & 0 & 0 \\ 0 & 0 & e^{i\phi/4} & 0 \\ 0 & 0 & 0 & e^{-i\phi/4} \end{pmatrix}. \quad (2.27)$$

The last step is to find a gate decomposition that suits one's hardware specification. Aiming for universality, we choose in our simulations to decompose these unitary operations in terms of single-qubit gates and CNOTs. Figs. 2.11 and 2.12 show the decomposition for the unitary transformation associated with the hopping terms defined in Eq. 2.26 (proposed in Ref. [87]) and the interaction terms defined in Eq. 2.27. In this configuration, each element of the ansatz is decomposed with 2 CNOTs. For an N-site chain ($N > 2$) and a ladder qubit topology, this leads to 6N - 4 CNOTs per layer of the ansatz.

2.5 Initial state

2.5.1 Slater Determinant preparation

To initialize our VQE procedure, we first need to prepare an initial state that will be implemented and evolved on the quantum computer. To do so, we need to choose a state that is both tractable, meaning that we possess an efficient representation for this state and implementable as a qubit state. For fermionic states, preparing ground states of one-body (i.e. non-interacting) Hamiltonians fulfills both of these requirements. Indeed, non-interacting fermionic states can be efficiently represented by Slater determinants, that can be prepared on a quantum computer as proposed in [83, 84, 88].

Let us first consider a general one-particle fermionic Hamiltonian H describing N orbitals. For simplicity, we choose H to conserve the number of particles, i.e. without any superconducting pairing. We can write H as

$$H = \sum_{ij} h_{ij} c_i^\dagger c_j = \boldsymbol{c}^{\dagger T} h \boldsymbol{c}, \tag{2.28}$$

where h is a $N \times N$ hermitian matrix that encodes the hopping amplitudes and the energy of the N orbitals indexed by i, and $\boldsymbol{c}^\dagger$ and $\boldsymbol{c}$ are defined as

$$\boldsymbol{c}^\dagger = \begin{pmatrix} c_1^\dagger \\ \vdots \\ c_N^\dagger, \end{pmatrix} \tag{2.29}$$

and

$$\boldsymbol{c} = \begin{pmatrix} c_1 \\ \vdots \\ c_N \end{pmatrix}. \tag{2.30}$$

In this picture, we do not need to manipulate states in the Fock space (of size 2^N) as it suffices to remain in a single-particle representation. Therefore, diagonalizing the $N \times N$ h matrix allows to access the energy spectra of the system, with $h = u\epsilon u^\dagger$, u being a $N \times N$ unitary matrix and ϵ a diagonal matrix containing the energy spectra. This yields to a new one-particle basis in which h is diagonal:

$$H = \sum_i \epsilon_i b_i^\dagger b_i, \tag{2.31}$$

with $\{\epsilon_i\}$ are the ordered energies of the orbitals defined by the new creation and annihi-

lation operators $b_i^\dagger$ and b_i. More specifically, these new orbitals are defined by $\boldsymbol{b}^\dagger = u^T \boldsymbol{c}^\dagger$. Therefore, we can easily express the ground state of H for N_p electrons:

$$|\Psi_0\rangle = \prod_{i=1}^{N_p} b_i^\dagger |\text{vac}\rangle\,, \text{ with } b_i^\dagger = \sum_{j=1}^{N} u_{ji} c_j^\dagger \tag{2.32}$$

where $|\text{vac}\rangle$ denotes the vacuum of particles.

The Slater determinant described in Eq. 2.32 is the state that we want now to implement on a quantum computer. To do so, we first prepare a reference state that corresponds to filling N_p orbitals described by the original creation operators:

$$|\phi_0\rangle = \prod_{i=1}^{N_p} c_i^\dagger |\text{vac}\rangle\,. \tag{2.33}$$

From this state, which can be easily prepared by applying the X gate to the qubits representing the occupancy of the N_p filled orbitals, we can perform the single particle change of basis. While $|\Psi_0\rangle$'s natural basis is described by u, $|\phi_0\rangle$'s basis is described by the identity matrix. The procedure is based on the fact that it is possible to diagonalize the matrix u (or at least the N_p first rows) thanks to series of Givens rotations $g_{ij}(\theta)$, $[g_{ij}(\theta)]_{ii} = [g_{ij}(\theta)]_{jj} = \cos\theta$, $[g_{ij}(\theta)]_{ij} = -[g_{ij}(\theta)]_{ji} = \sin(\theta)$, and $[r_{ij}(\theta)]_{kk} = 1$ if $k \neq i$ or $j.$, $[g_{ij}(\theta)]_{kp} = 0$ if $k \neq p \neq i$ or j. These rotations can be determined via a QR decomposition of u.

As u is a unitary matrix, the resulting diagonal matrix will have diagonal elements of modulus 1:

$$(\prod_{ij} g_{ij}(\theta_{ij}))u = \text{diag}(e^{i\phi_1}, \ldots, e^{i\phi_N}). \tag{2.34}$$

The series of rotation links between between the basis of $|\Psi_0\rangle$ and $|\phi_0\rangle$, up to trivial phases. As described in [83, 84, 88], rotating the $N \times N$ single particle basis by $g_{ij}(\theta)$ is equivalent to applying the $2^N \times 2^N$ fermionic unitary transformation $G_{ij}(\theta) = e^{i\theta(c_i^\dagger c_j - c_j^\dagger c_i)}$ (This can be proven for instance by the means of Thouless theorem [89, 88]). Therefore, from $|\phi_0\rangle$, we can construct $|\Psi_0\rangle$:

$$|\phi_0\rangle = \prod_{ij} G_{ij}(\theta_{ij}) |\Psi_0\rangle\,. \tag{2.35}$$

By reversing the order of the gates, we can therefore prepare the state $|\Psi_0\rangle$. Thanks to a fermion-to-qubit mapping, such as the Jordan-Wigner transformation, the sequence of Givens rotations can be implemented as qubit gates. By performing the diagonalization

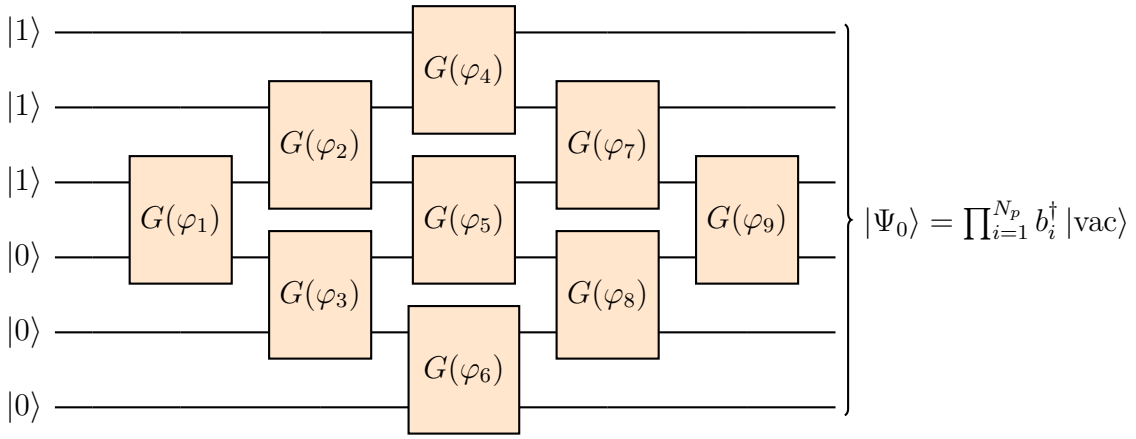

Figure 2.13: From a Slater determinant prepared in the computational basis $|\phi_0\rangle = \prod_{i=1}^{N_p} c_i^\dagger |\text{vac}\rangle$, a series of Givens rotations allows to perform the single-particle change of basis that prepare the Slater determinant of interest $|\Psi_0\rangle = \prod_{i=1}^{N_p} b_i^\dagger |\text{vac}\rangle$.

of u with rotations only acting on neighboring rows and columns, one can implement the corresponding quantum circuit while avoiding fermionic gates between orbitals that are not neighbors with respect to the Jordan-Wigner ordering, i.e. with Z strings. Using the fact that some of these gates can be performed in parallel, the Slater determinant preparation can be performed by a circuit of depth $\mathcal{O}(N)$ with $N^2/2$ gates with linear connectivity, as shown in Fig. 2.13. When considering fermions with a spin degree of freedom, preparing a Slater determinant with spin symmetry can be done by preparing the state of interest on the two separate qubit registers representing the spin up and down orbitals, therefore reducing the circuit cost.

Using the Jordan-Wigner transformation, we can express the Givens gates as qubit gates, which can be decomposed into CNOTs and single-qubit rotations, as shown in Fig. 2.14. In this work, we use this procedure as implemented in the OpenFermion package [85].

$$G(\theta) = e^{i(c_i^\dagger c_{i+1} - c_{i+1}^\dagger c_i)\theta} = e^{i(X_i Y_{i+1} - X_{i+1} Y_i)\theta/2} = \begin{pmatrix} 1 & 0 & 0 & 0 \\ 0 & \cos(\theta) & -\sin(\theta) & 0 \\ 0 & \sin(\theta) & \cos(\theta) & 0 \\ 0 & 0 & 0 & 1 \end{pmatrix} \quad (2.36)$$

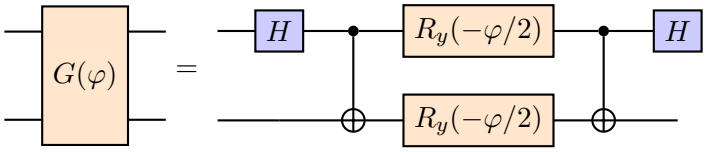

Figure 2.14: Gate decomposition for Givens rotation.

2.5.2 Mean-field vs $U = 0$ ground state

Due to the simplicity of their preparations on a quantum computer, we will restrict ourselves to Slater determinants as initial states for our VQE algorithm. We investigate two natural choices: a free fermion $U = 0$ ground and a mean-field Hartree-Fock (HF) solution as the latter is commonly utilized in VQE studies in the chemistry domain with widely studied Unitary Coupled Cluster Ansatz (UCC) [90, 91, 68]. In similarity to problems in chemistry the HF state provides a good approximation to the ground state energy (see Fig. 2.15a).

However, often in the study of condensed matter systems, one is interested in more quantities than just the mere energy such as long-range correlations or the expectation value of the square of the total spin $\langle S^2 \rangle$. The most comprehensive measure of the quality of the obtained state is the fidelity $\mathcal{F} = |\langle \Psi(\boldsymbol{\theta}) | \Psi_{\text{ex}} \rangle|^2$, where $|\Psi(\boldsymbol{\theta})\rangle$ is the approximate solution and $|\Psi_{\text{ex}}\rangle$ the exact solution. The fidelity will be 0 if the approximated solution is totally different from the exact one and 1 if these two solutions match.

The mean-field solution is obtained by transforming the two-body term in the Hamiltonian responsible for interaction into a one-body term thanks to the following approximation:

$$\sum_i n_{i\uparrow} n_{i\downarrow} \simeq \sum_i \left(\langle n_{i\uparrow} \rangle n_{i\downarrow} + \langle n_{i\downarrow} \rangle n_{i\uparrow} \right). \tag{2.37}$$

Starting from initial guess $\{\langle n_{i\sigma} \rangle_0\}$, the average densities $\{\langle n_{i\sigma} \rangle\}$ are tuned self-consistently to minimize the energy $E_{\text{HF}} = \langle \Psi_{\text{HF}} | H_{\text{HF}}(\{\langle n_{i\sigma} \rangle\}) | \Psi_{\text{HF}} \rangle$ where $|\Psi_{\text{HF}}\rangle$ is the ground state of the mean-field Hamiltonian

$$H_{\text{HF}}(\{\langle n_{i\sigma} \rangle\}) = H_t + U \sum_i \left(\langle n_{i\uparrow} \rangle n_{i\downarrow} + \langle n_{i\downarrow} \rangle n_{i\uparrow} \right) - \frac{U}{2} \sum_{i\sigma} n_{i\sigma}. \tag{2.38}$$

The total spin operator S^2 can be express as $S^2 = (S^x)^2 + (S^y)^2 + (S^z)^2$ with $S^\alpha = \sum_i S_i^\alpha$ with $\alpha = x, y, z$ and i the position index. One can first express those operators in terms of fermionic operators: $S_i^x = \frac{1}{2}(S_i^+ + S_i^-)$, $S_i^y = \frac{1}{2i}(S_i^+ - S_i^-)$, $S_i^z = \frac{1}{2}\left(n_{i\uparrow} - n_{i\downarrow}\right)$ with the spin raising and lowering operators $S_i^+ = c_{i\uparrow}^\dagger c_{i\downarrow}$ and $S_i^- = c_{i\downarrow}^\dagger c_{i\uparrow}$. Thanks to the Jordan-Wigner transformation described earlier in Sec. 2.4.2, one can write those fermionic operators into

qubit operators which can be measured on quantum hardware.

In terms of fidelity, the free fermion solution is much closer to the exact solution in the regime of $0 \leq U/t \approx 10$ Fig. 2.15b. Moreover, the free fermion solution respects the S^2 symmetry of the problem. On the other hand, the Hartree-Fock solution produces non-zero values for the total spin S^2. Note that a Restricted Hartree-Fock calculation (i.e. a mean-field optimization constrained by spin symmetries) will return the free fermion ground state as the Hubbard model contains only two-body interactions between opposite spin electrons from the same site (i.e. same spatial orbital). As VHA is Hamiltonian-based, the symmetries are preserved throughout the circuit (all the gates commute with the particle number operator N and the spin operators S^z and S^2). Therefore choosing an initial state with the right set of quantum numbers avoids the variational ansatz to span non-physically relevant parts of the Hilbert space. Other strategies aiming at including symmetries in the VQE process have been also proposed in [72, 92, 93, 94, 95].

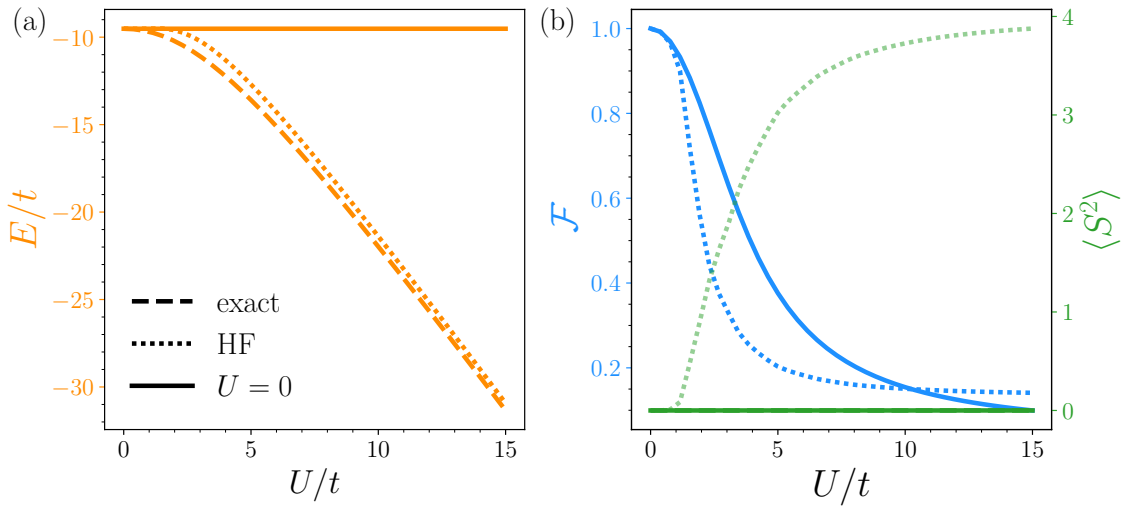

Figure 2.15: Comparison of $U = 0$ free fermion and mean-field Hartree Fock state as the initial state. (a) The energy $\langle\Psi|H(t,U)|\Psi\rangle$ and (b) the fidelity and the total spin $\langle S^2\rangle$ value as a function of U for a $N = 8$ chain. The fidelity of the exact solution is trivially one. For both (a) and (b), the full line, dashed line, and dotted line designate respectively the $U = 0$, mean-field Hartree Fock, and exact solution.

2.6 Results

To assess the performance of the VQE algorithm, we perform classical state vector simulations, focusing on a $N = 8$ site Hubbard chain, which corresponds to 16 qubit simulations. We conduct a two-fold analysis. First, we focus on key metrics directly tied

to the algorithm. These metrics include the energy, which serves as the loss function in our minimization problem. The objective is to minimize this energy, as it corresponds to the ground state energy of the quantum system. Additionally, we evaluate the overlap between the approximate ground states generated by the VQE and the exact solutions obtained through exact diagonalization. This overlap measurement helps us gauge the accuracy of the VQE results in approximating the true ground state of the system. Secondly, we adopt a condensed matter perspective by inspecting the physical properties we obtained from the algorithm, such as charge and spin correlators, which highlight phenomena caused by the interaction of the electrons.

2.6.1 Energy and fidelities

In this section, we focus on noiseless simulations of this hybrid quantum-classical scheme. The classical optimization is performed by the COBYLA optimizer [96, 97, 98]. In addition, we use an iterative approach consisting in initializing our simulations by targeting an initial value of Coulomb repulsion from the intermediate regime: $U_0 = 5$ (we set $t = 1$). We try many random initial parameters contained in $[-\pi/5, \pi/5]$, keep the lowest energy solution, and use the optimized parameters as initial parameters to simulate the case $U_1 = U_0 \pm \delta U$. Throughout the simulations, the optimized parameters for the case $U_{N-1} = U_0 \pm (N-1)\delta U$ are used as initial parameters for $U_N = U_{N-1} \pm \delta U$. In some sense, the parameters are optimized "adiabatically" as we vary U. This method is motivated by the fact that the choice of initial parameters has a significant impact on the optimized solution, and by trying multiple starting parameters, we mitigate the effect of initial parameters choice, which improves the result for the whole range of U values and speed up the optimization routine.

Fig. 2.16 shows the results for a $N = 8$ Hubbard chain. We can distinguish between the weak and strong interaction regimes. Whereas energy and fidelity errors remain small in weakly interacting regime $U \simeq 2$ even for limited numbers of ansatz layers N_L, the non-interacting initial state already providing a close match, quality of results decreases as U increases. This can be understood as the result of lower fidelity of the initial state (Fig. 2.15). Fig. 2.16 shows the effect of the number of layers N_L on the fidelity of the optimized states at different values of U. To simulate a Hubbard chain in a low interacting regime, only a few layers are required to reach relatively high fidelities $> 95\%$. However, as U increases, the overlap between the initial and the exact solution becomes smaller. Adding more layers to the parametrized circuit leads to better results, although not systematically, highlighting the complex nature of the resulting variational state. This is shown for example that the $N_L = 3$ ansatz produces higher energy states than the

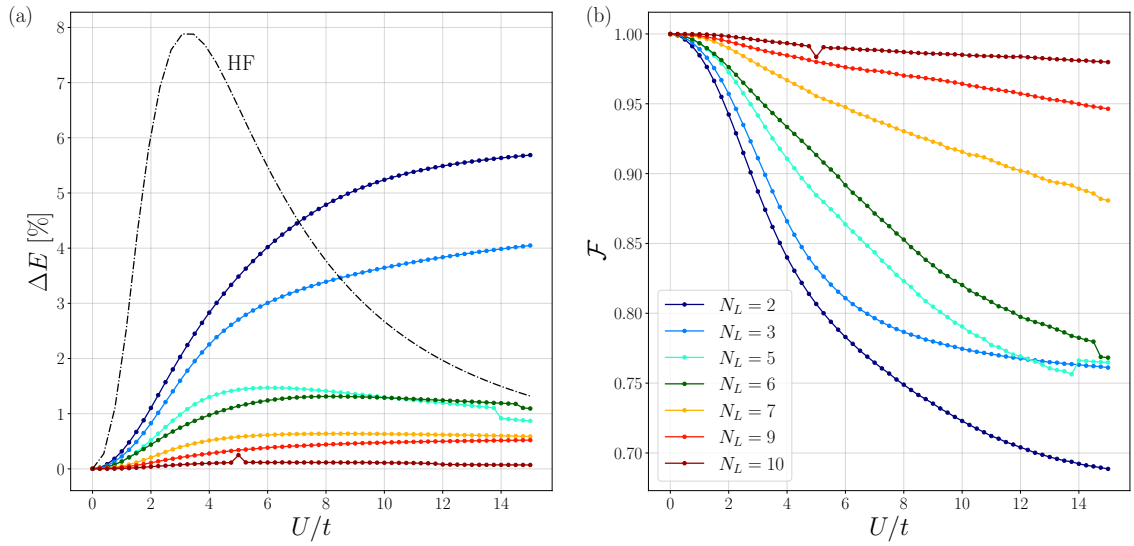

Figure 2.16: Classical simulation of the VQE algorithm applied to the 1D Hubbard model with 8 sites (16 qubits), with $U_0 = 5$. (a) The energy error for different circuit depths. (b) The fidelity of the output state with the exact ground state.

$N_L = 5$ case but leads to similar fidelity results in the region $U \gtrsim 12$. This shows that the ansatz produces polluting states that have low energies but are further away from exact solutions. Similarly, Fig. 2.17 shows that $N_L = 4$ ansatz produces better fidelities than $N_L = 5, 6$ simulations. One can note a kink in the $N_L = 10$ results at $U = 5$. This shows that the multi-start parameters still resulted in a false minima value with slightly higher energy and lower fidelity. However, solutions were improved when simulating the next case $U \pm \delta U$.

To show how sensitive are the results with respect to the initial parameters, we try 100 random initial parameters contained in $[-\frac{\pi}{5}, \frac{\pi}{5}]$ for $U_0 = 5$ and compare the obtained results. Fig. 2.18 shows the average optimized energies and their associated fidelities with standard deviation, as well as the best run over the set of initial parameters. As shown in this figure, a wide range of result quality can be obtained despite the optimization having converged. This highlights the utility of this multistart approach, which lead to significantly better energies compared to a random instance, which then benefits the ground state search for a broad range of U by performing an adiabatic optimization procedure.

2.6.2 Physical properties from low-depth circuits

Despite the fact that low-depth variational circuits fail to produce the exact ground state of the 1D Hubbard chain, we can still wonder how good are those approximate

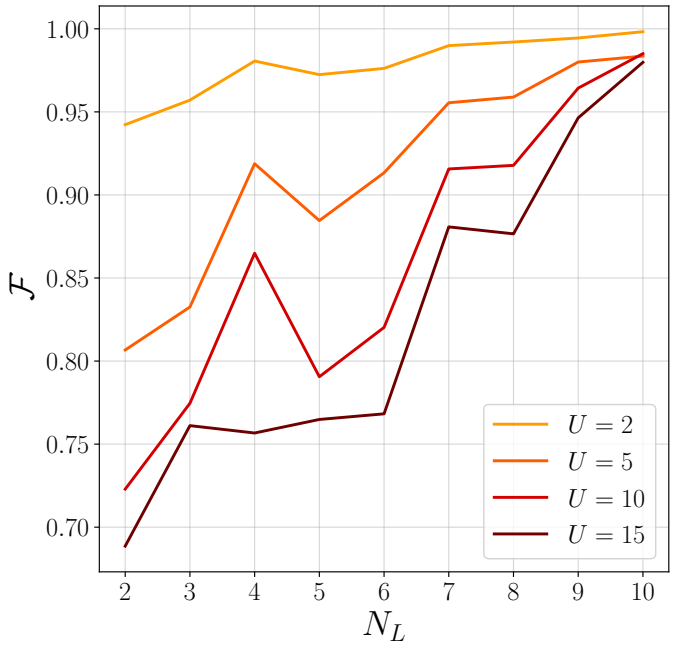

Figure 2.17: The fidelity of the optimized states with exact solutions as a function of the number of layers N_L for different values of U.

solutions describing some particular expected behavior of our system. In particular, the 1D Hubbard model exhibits physics properties caused by the interaction between the electrons. Being able to observe these phenomena from the solutions obtained by the VQE algorithm, despite being only approximate, reflects the quality of the simulation. More specifically, we can address the question of what physics is captured with respect to the circuit complexity. Here, we focus on correlations due to interaction in the system. A basic phenomenon to investigate is the localization of electrons: as the Coulomb repulsion gets more intense between the particles, fewer and fewer sites are likely to be occupied by two electrons. At half-filling, this causes the electron to be localized on one site. To investigate this, we use the local charge correlators $\langle n_\uparrow n_\downarrow \rangle = \frac{1}{N} \sum_i \langle n_{i\uparrow} n_{i\downarrow} \rangle$, N being the number of sites, which corresponds to the average number of doubly occupied sites along the chain. Fig. 2.19b shows the fidelity as a function for U for different depths and its corresponding values for $\langle n_\uparrow n_\downarrow \rangle$. Despite having a low overlap with the exact solution, the optimized states recover pretty well the transition from delocalized to localized electrons as the on-site Coulomb repulsion increases. This shows that the ansatz builds up non-trivial correlations to a non-interacting state, and captures this basic many-body phenomenon.

Secondly, because two electrons of opposite spin will repel each other on the same site, while two electrons with the same spin cannot populate the same site as a consequence of Pauli's exclusion principle, increasing U will induce an antiferromagnetic order in the

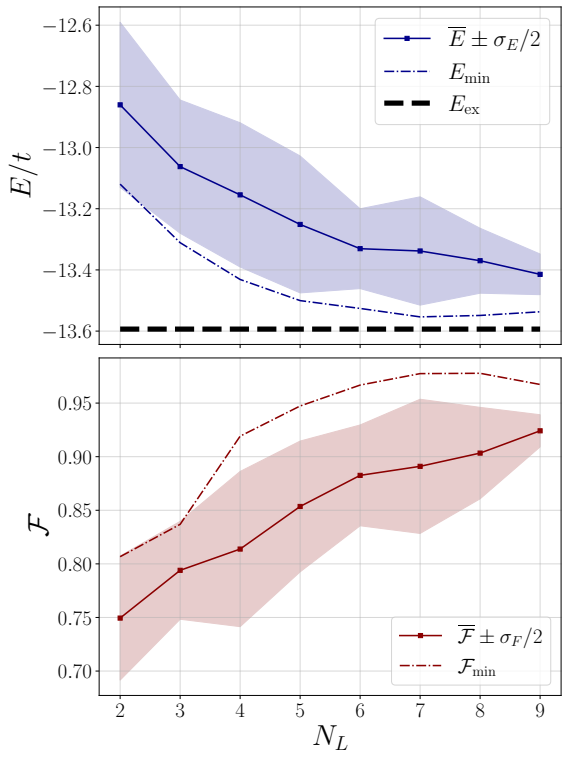

Figure 2.18: Averaged optimized energy E in units of t over a set of 100 simulations with random initial parameters. The shaded areas correspond to the averaged energies (fidelities $\pm\sigma_E/2$ ($\pm\sigma_F/2$), σ_i being the standard deviation. The colored dashed line corresponds to the minimal optimized energy and its associated fidelity.

chain. To observe this, we take a look at long-range spin correlations in our variational states, defined by $C^z_{ij} = \langle S^z_i S^z_j \rangle - \langle S^z_i \rangle \langle S^z_j \rangle$. As a result, we expect that the spin value of one site is correlated with the sites along the chain. This is shown in Fig. 2.20a, where we show the correlations for different values of U (2,5 and 15) and different numbers of circuit layers (3,6 and 9). where we get sign-alternating values for $C^z_{ij}|_{i=0}$ for example. For the low to moderate regimes ($U = 2$ and 5 here), low-depth circuits are able to capture the weak correlations. However, when simulating larger Us ($U = 15$), the short-depth circuits capture well correlations between neighboring sites, but fail for longer-range physics, even for a deeper circuit with the example of 9 layers.

Overall, we conclude that the solutions produced by VHA allow us to prepare physically relevant states, capturing local spin and charge correlations of the 1D Hubbard model, although failing to reach high-fidelity solutions in the strongly correlated regimes. As a consequence, low-depth circuits fail to capture long-range correlations.

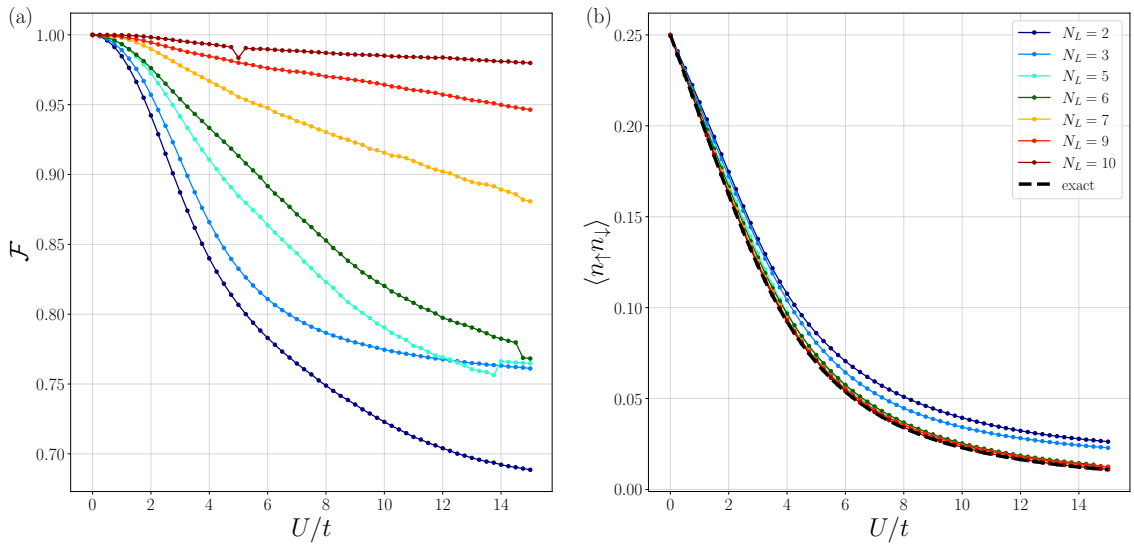

Figure 2.19: (a) The fidelity of the optimized states as a function of U for different numbers of layers for $N = 8$ sites. (b) The average number of doubly occupied sites from the optimized states. Although not reaching high-fidelity solutions, low-depth solutions capture the localization of the electrons as a consequence of an increasing interacting strength.

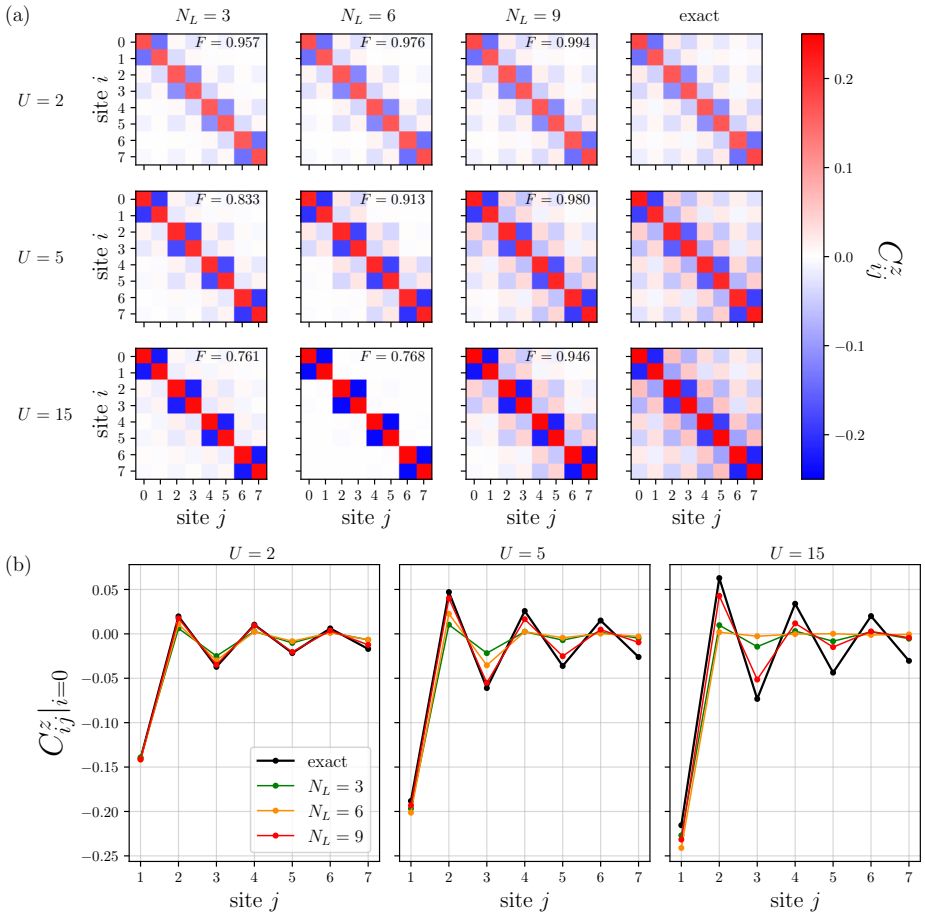

Figure 2.20: (a) The fidelity $\mathcal{F}$ as a function of U/t for $N_L = 3, 6$ and 9 VQE solutions (8-site Hubbard chain). (b,c,d,e) Spin correlation $C^z_{ij} = \langle S^z_i S^z_j \rangle - \langle S^z_i \rangle \langle S^z_j \rangle$ calculated between one end of the chain ($i = 0$) and the other sites ($j \geq 1$) as a function of U for $N_L = 3, 6, 9$ and exact solution. (f,g,h) $C^z_{ij} = \langle S^z_i S^z_j \rangle - \langle S^z_i \rangle \langle S^z_j \rangle$ for $i = 0$ as a function of $j \geq 1$ for $U = 2, 5$ and 15 for a number of ansatz layers $N_L = 3, 6, 9$.

2.7 Noisy simulations and experiment

VQE algorithms were introduced to extend the capabilities of current hardware, strongly limited by noise and decoherence. A natural question when investigating the performance of an ansatz is how robust it is when the noise occurs in the hardware. Here we investigate how noise degrades the output of the algorithm. To do so, we perform simulations of the algorithm with a noise model as well as an actual test on IBM quantum devices, focusing on a 2-site Hubbard system, which corresponds to a 4-qubit problem. Along with the noisy simulation, we implement two error mitigation strategies, described below, and observe how they affect the quality of the results. While noise models used here have been presented in the previous chapter in Sec. 1.2, namely phase and amplitude damping along with depolarizing channel, we introduce here the error mitigation techniques employed here.

2.7.1 Post-selection

The first error mitigation we use consists in a classical post-processing of the measurement output obtained from the device. We take advantage of the fact that the desired state lies in specific subspaces of symmetries, that are conserved by the variational circuit. More specifically, to mitigate errors coming from noise, we post-select the measurements that respect the number of particles and S^z symmetries. To do this, we first need to choose a measurement scheme to evaluate the Hamiltonian. We use the following scheme proposed in [51]:

- The ZZ terms are measured in the computational basis without the need for a change-of-basis circuit.
- To efficiently measure the hopping terms $\frac{1}{2}(XX + YY)$, we implement a change of basis $\mathcal{B}$ that diagonalize the operator in the computational basis such that $\mathcal{B}^\dagger \frac{1}{2}(XX + YY)\mathcal{B} = D$, D being diagonal. The circuit shown in Fig. 2.21 transforms a hopping term into $D = |01\rangle\langle 01| - |10\rangle\langle 10|$.

As $\mathcal{B}$ also conserves the number of particles for each spin, we can reject any shots that do not contain the right number of spin up and down electrons, as they are only produced by errors occurring in the device. For example, for a 2-site model, any measurement (when evaluating the hopping terms or the onsite interaction terms) that is not contained in $\{0101, 1010, 1001, 0110\}$ can be discarded. This method allows for mitigating amplitude damping, read-out, and bit-flip errors.

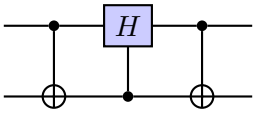

Figure 2.21: Circuit performing the change of basis to measure $\frac{1}{2}(XX + YY)$.

2.7.2 Zero-noise extrapolation

This error mitigation method was introduced first in Ref. [49]. The general idea is to artificially increase the noise of the device, in order to measure an observable at different noise levels, and then extrapolate to the zero-noise value, as depicted in Fig. 2.22. To understand its motivation, let us suppose an open system composed of qubits initially prepared in ρ_0. We apply a quantum circuit described by a time-dependent driving Hamiltonian $K(t) = \sum_\alpha J_\alpha(t) P_\alpha$, where P_α are Pauli strings and $J_\alpha(t)$ real coefficients. The system will be described by Eq. (2.39):

$$\frac{\partial}{\partial t}\rho(t) = -i[K(t), \rho(t)] + \lambda \mathcal{L}(\rho(t)). \tag{2.39}$$

$\mathcal{L}(\rho)$ is a noise generator that is invariant under time rescaling and independent from $K(t)$, which can be experimentally quite demanding. Then, an observable O can be measured on the state $\rho_\epsilon(T)$ driven by K for a duration T, such that $\langle O \rangle_\epsilon = \mathrm{tr}(O\rho_\epsilon(T))$, which can be expressed for $\epsilon \ll 1$ (ϵ being the experimental noise strength) by the following:

$$\langle O \rangle_\epsilon = \langle O \rangle_0 + \sum_{k=1}^{n} c_k \epsilon^k + \mathcal{O}(\epsilon^{n+1}), \tag{2.40}$$

$\langle O \rangle_0$ being the noise-free expectation value: $\langle O \rangle_0 = \mathrm{tr}(O\rho_0(T))$. Let us assume one can scale up the noise level ϵ by a factor c. By running the quantum circuit for different noise levels $\epsilon_i = c_i \epsilon$ for $i = 0, ..., n$ ($c_0 = 1, c_i > 1$ for $i > 0$) one can obtain an improved estimate $\bar{O}_n$ of $\langle O \rangle_0$ up to precision $\mathcal{O}(\epsilon^{n+1})$ expressed as:

$$\bar{O}_n = \sum_{i=0}^{n} \gamma_i \langle O \rangle_{\epsilon_i}, \tag{2.41}$$

with the coefficients $\{\gamma_i\}$ being solutions of $\sum_i \gamma_i = 1$ and $\sum_i \gamma_i c_i^k = 0$ for $k = 1, ..., n$. In the case $n = 1$, this is equivalent to a simple linear extrapolation:

$$\bar{O}_1 = \frac{c_1 - c_0}{c_1}(\langle O \rangle_{c_0\epsilon} - \langle O \rangle_{c_1\epsilon}) + \langle O \rangle_{c_1\epsilon}. \tag{2.42}$$

This method relies on the fact that one can access a low-level control of the device,

with noise satisfying the requirements described earlier, which is not necessarily the case. Other noise scaling techniques allow to performance of a zero-noise extrapolation of an observable, more appropriate to "digital" quantum computing [99, 100]. The most common one is the unitary folding. It consists in replacing a gate U by an equivalent sequence if run on a noise-free device but at a higher cost, by the following substitution:

$$U \rightarrow U(U^\dagger U)^n, \text{ with } n \in \mathbb{N}. \tag{2.43}$$

This way, the effective noise level is artificially increased as the circuit contains more gates. For example, if the full quantum circuit is described by $U = \prod_{i=1}^{D} G_i$, where $\{G_i\}$ are layers of gates and D is the circuit depth, the circuit folding gives a new circuit depth of $(1 + 2n)D$. To understand its effect on the noise scaling, let us describe the noise by a depolarizing model:

$$\rho \rightarrow \alpha\rho + (1 - \alpha)\frac{\mathbb{1}}{2^N}, \ \alpha \in [0, 1], \tag{2.44}$$

N being the number of qubits. The α coefficient can be taken as $e^{-\epsilon N_g}$, assuming that each gate comes with the same error rate. Therefore, folding the circuit n times requires $(1 + 2n)N_g$ gates, which corresponds to scaling the noise as $\epsilon \rightarrow (1 + 2n)\epsilon$. This motives an exponential extrapolation (instead of polynomial) for the observable:

$$\langle O \rangle_\epsilon = A + Be^{C\epsilon}. \tag{2.45}$$

However, even a simple folding $n = 1$ can already be quite demanding in terms of quantum resources on current devices. To fine-tune the scaling noise factor and scale the effective noise in the circuit at a cheaper cost, partial folding techniques propose to only fold a subset of gates.

In this work, we test a simple zero-noise extrapolation by performing a linear extrapolation with noisy simulation. Instead of folding the circuit, we directly modify the noise parameter in the depolarizing noise model, which is equivalent to simulating a folded circuit according to Eq. 2.44.

2.7.3 Results

We performed simulations based on density matrix calculations to investigate the performance of the VQE algorithm in the presence of noise. To set the inactive duration, we assign an average duration of $t_1 = 60$ ns for single-qubit gates and $t_2 = 425$ ns, as well as $T_1 = 120$ μs and $T_2 = 85$ μs. These parameters will be used to describe the phase and amplitude damping channels. For gate errors, we set $p_1 = 0.3\%$ and $p_2 = 1\%$ the

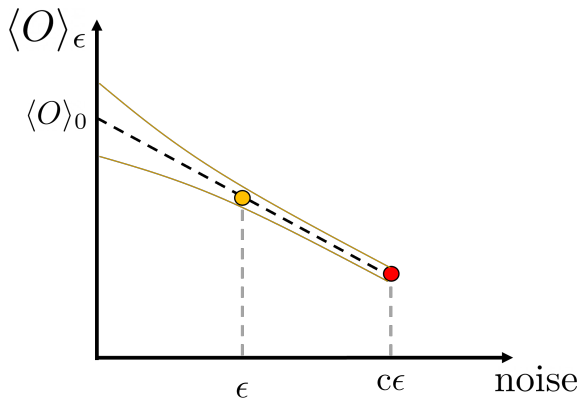

Figure 2.22: A schematic explaining the principle of zero-noise extrapolation. When interested in the expectation value of an observable, we artifically increase the noise level of the device for different amplication factor c, which allows to make an estimation of the noiseless value by extrapolation.

1-qubit and 2-qubit gates errors (modeled by a depolarizing channel) which corresponds to current-day quantum computers performances from IBM [6].

Fig. 2.23 shows the obtained results for the 2-site Hubbard system and simulations incorporating noise being compared with noiseless simulations. We choose to implement only one layer of the ansatz upon the free fermion ground state. Whereas for the noiseless case, exact solutions are obtained with only one layer of ansatz for all values of U, noise affects greatly the quality of the results. While idle noise induces an infidelity of about 2%, adding gate errors degrades significantly the results, indicating that it is the major source of error.

In an attempt to mitigate those errors, we test the two error mitigation techniques described above: post-selection and zero-noise extrapolation. As described previously, we post-select measurement outputs based on the *a priori* known symmetries of the target solution. In this work, we rejected the shots not respecting the number of particles and S^z symmetries. Moreover, we simulate the same circuit with error rates p_2 and $2p_2$ in order to perform a first-order extrapolation. This gives an approximation of the noiseless value of the energy at each iteration of the minimization process, but also for other quantities like $\langle n_\uparrow n_\downarrow \rangle$ measured from the optimized state. Fig. 2.23 also shows the noisy results with and without mitigation. In this small instance with only two parameters, the minimization does not appear to be the bottleneck of the simulation. However, the gate errors cause large deviations in the observables investigated here. The 2-point zero-noise extrapolation makes significant improvement but does not give a quantitative agreement with exact/noiseless results.

Post-selected measurements also offer significant improvements over non-selected results, at a very limited cost. For example, we recover qualitatively well the decrease of doubly occupied sites as the interaction increases. Most interestingly, combining post-selection and zero-noise extrapolation allows to recover a quantitative agreement with exact solutions. While the realistic error rates used here impact the expectation values beyond a linear approximation, post-selecting lowers the effective noise level in a regime where the zero-noise extrapolation becomes valid. This indicates that error mitigation has the potential to extract relevant information from noisy states, and in the context of these simulations, recover exact results although the noisy state does not have a fidelity 1 with the exact solution.

Finally, we test those results against the real implementation of the algorithm on IBM's hardware `ibmq_quito` [6] as shown in Fig. 2.23. Although the benchmark parameters were close to the noise parameters ($\epsilon_1^{\text{exp}} \simeq 2.6.10^{-3}$, $\epsilon_2^{\text{exp}} \simeq 1.2.10^{-2}$ $T_1^{\text{exp}} = 96\mu s$ and $T_2^{\text{exp}} = 102\mu s$) at the time of the experiment, the experimental results seem more affected by noise. This can be explained by the absence of read-out error (that is substantial in current devices) and shot noise in our model (the experiment's number of shots was set to 8,192), but also by the fact that additional noise occurs in the hardware like crosstalk noise. Finally, additional SWAP gates (decomposed with 3 CNOTs) are needed because of the hardware's topology. In this case, the circuit is run on a set of qubits with linear connectivity, while the ideal connectivity with respect to the Jordan-Wigner mapping corresponds to a ladder-shaped set of qubits (or a square for 2 sites). However, the experimental results are in qualitative agreement with the noisy simulations as both energy and double occupancies follow the same behavior. While we didn't implement zero-noise extrapolation as it represents a difficult experimental challenge, post-selection improves overall the results for the energy values as well as the number of doubly occupied sites, where the steep decrease for small values of U is better captured.

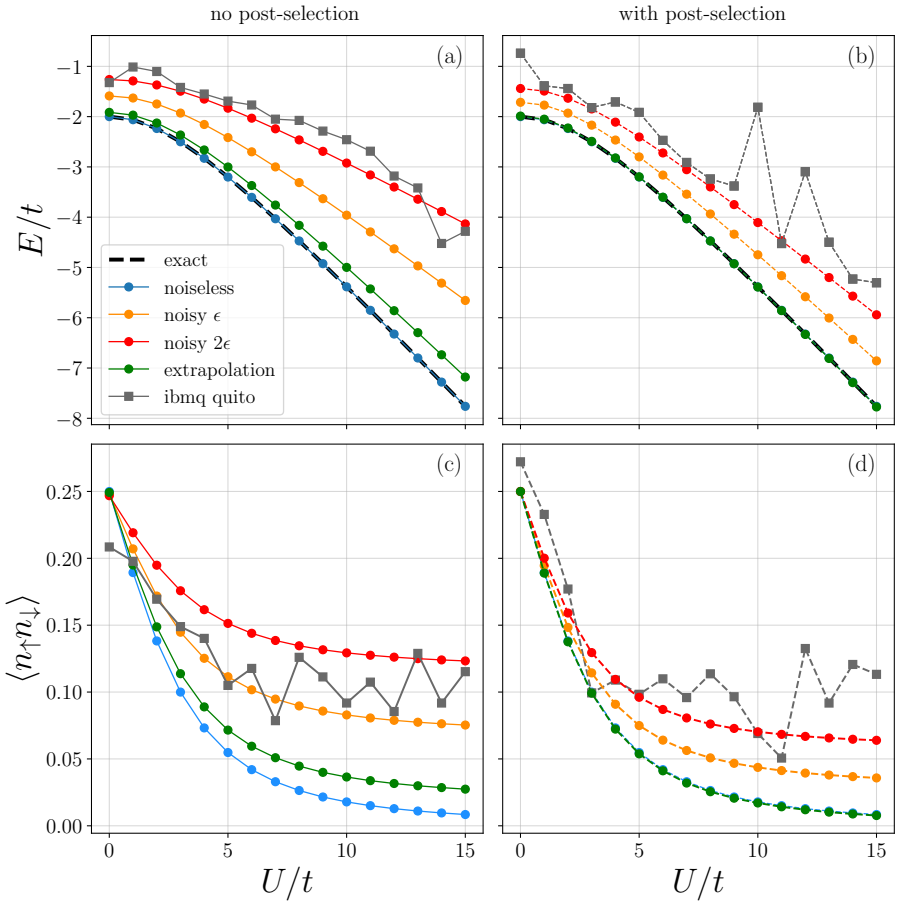

Figure 2.23: Noisy simulation with two level of noise, $\epsilon_1 = 3.10^{-3}$ and $\epsilon_2 = 10^{-2}$, and $2\epsilon_1, 2\epsilon_2$ and experimental data from IBM Quantum's `ibmq_quito`. Panels (a) and (c) ((b) and (d)) show the energy and the double occupancies as a function of U without (with) post-selection.

.

2.8 Conclusion

In this chapter, we have explored the possibility of using quantum computers to find the ground state of interacting fermionic systems with the VQE algorithm. To be more specific, we investigated the Variational Hamiltonian Ansatz (VHA) [47] through the example of the one-dimensional Hubbard model. This ansatz is inspired by the natural idea of adiabatic evolution, in which a free fermion initial state is driven towards the correlated ground state by slowly increasing interaction in time. Each time steps are replaced by variational parameters in the hope of finding an optimized path to the ground state. We perform classical simulations of the VQE algorithm for an 8-site Hubbard chain which corresponds to 16 qubit simulations.

By calculating the energy error and the fidelity of the optimized states, we quantify the performances of the algorithm. Although low numbers of layers give satisfying results in weakly correlated regimes, higher circuit depths are required to target strongly interacting ground states. We study how well the approximated ground states capture the physics of the Hubbard model by investigating correlations built upon the free fermion Slater determinant. We observe that short-length circuits can capture well the localization of electrons as U increases. Long-range antiferromagnetic correlations are however harder to obtain despite high fidelity states and require a larger number of ansatz layers.

Finally, we test the ansatz against noise for a 2-site Hubbard model. We include noise models in our simulations based on density matrix calculations and compare them with experimental results from IBM Quantum's `ibmq_quito` device. Because of two-qubit gate errors results are greatly degraded, which indicates the practical limit of Trotterized-like ansätze. Zero-noise extrapolation enables us to qualitatively improve our noisy simulation results for both the energy and the number of doubly occupied sites. Further improvements should be aimed at both proposing relevant initial states requiring short circuits still exhibiting the right symmetries as well as bridging this scheme towards hardware-efficient approaches. Additionally, optimization barren plateaus or large overheads for expectation values sampling can also appear to be significant bottlenecks [19], and strategies to overcome these issues must be expored.

3 | State Preparation of Valence Bond States on a quantum computer: the example of the AKLT state

3.1 Introduction

In the previous chapter, we explored the possibility of finding ground states of quantum many-body systems thanks to a quantum computer. However, expressing ground states on correlated systems may not always be a herculean task, and there are instances where certain interesting states exhibit straightforward analytical representations. Conversely, accessing their dynamics can be much challenging as the states lose their simple structure, and require costly computational techniques. Furthermore, studying the physics around those exactly solvable points can also constitute a challenge. Using quantum computers for these classically difficult tasks is a promising approach.

For example, in the Quantum Phase Estimation (QPE) algorithm [56] or the Variational Quantum Eigensolver (VQE) [18, 19] introduced in the previous chapter, it is desirable to first prepare an initial state with a substantial overlap with the (unknown) exact ground state. Therefore, elaborating schemes allowing to prepare classically tractable states is an appealing and useful task in order to approach relevant problems on quantum computers.

In this chapter, we focus on the specific example of spin-1 chains as prototypical quantum systems whose ground states exhibit exotic properties while having a simple tractable form. To give a historical overview, in 1983, Haldane argued that spin chain properties fundamentally differ depending on the nature of the spins [21, 22]: while half-integer spin chains are gapless with power-law correlations, integer spin chains are gapped

and show exponentially decaying correlations. Only proved in the large spin limit at the time, his conjecture has been verified both experimentally [101, 102, 103] and numerically [104]. In 1987, Affleck, Kennedy, Lieb, and Tasaki discovered the so-called AKLT model [20] which describes a one-dimensional spin chain whose exact ground state exhibits a finite excitation gap and an exponential decay of the 2-point correlation function, thus providing a tractable example in favor of Haldane's prediction. It was found that the AKLT state possesses several unexpected properties such as a "hidden antiferromagnetic order", and spin-half edge states which can be understood in terms of a symmetry-protected topological phase (SPT) [105, 106, 107]. This "fractionalization" is reflected by non-trivial degeneracies in the entanglement spectrum [108]. Moreover, the AKLT state is one of the most famous examples of Matrix Product States (MPS) [23, 24], a class of states introduced to efficiently describe ground states of 1D local Hamiltonians. Finally, the AKLT states are considered promising candidates to perform one-way quantum computation [109, 110, 111, 112, 113, 114]. While in the circuit model of quantum computation, quantum information is encoded into qubits that are mostly isolated from each other except multiple-qubit gates are performed, the one-way model uses on the other hand an entangled resource state (such as the AKLT state) to perform computation by measuring individual spins.

Based on their simple constructions, we design schemes for generating the AKLT state on actual quantum computers. This quantum computer embedding of the AKLT chain adds to a handful of models that are exactly encodable on a quantum computer. Also, it should be noted that only a few actual experimental realizations of such states exist.

This chapter is organized as follows, after introducing the AKLT state in Sect. 3.2, we propose two schemes to produce a one-dimensional AKLT ground state on a qubit-based quantum computer. In Sect. 3.3, we follow the natural construction of the AKLT state by first preparing a product of singlet states between pairs of qubits and performing a projection onto the triplet $S = 1$ subspace for each spin-1 site. We also estimate the number of repetitions needed to successfully produce the AKLT state. In Sect. 3.5, we propose a scheme based on the MPS representation of the AKLT state to design a quantum circuit producing open-boundaries AKLT chains. Finally, we validate the two schemes experimentally on IBM Quantum's device `ibmq_lagos`.

3.2 The AKLT state

The 1D AKLT Hamiltonian is written as

$$H = \sum_i \left(\mathbf{S}_i \mathbf{S}_{i+1} + \frac{1}{3} (\mathbf{S}_i \mathbf{S}_{i+1})^2 \right), \tag{3.1}$$

where $\mathbf{S}_i$ is a spin S = 1 operator on site i. A spin state restricted to two adjacent sites i and $i+1$ can have a total spin of 0, 1, or 2. We note the projection onto the subspace $S = 2$ by $P_2(\mathbf{S}_i + \mathbf{S}_{i+1})$. It can be expressed as

$$P_2(\mathbf{S}_i + \mathbf{S}_{i+1}) = \frac{1}{2}(\mathbf{S}_i\mathbf{S}_{i+1}) + \frac{1}{6}(\mathbf{S}_i\mathbf{S}_{i+1})^2 + \frac{1}{3}. \tag{3.2}$$

Then, up to a constant, we can rewrite H as:

$$H = \sum_i H_i, \text{ with } H_i = 2P_2(\mathbf{S}_i + \mathbf{S}_{i+1}). \tag{3.3}$$

As projectors have eigenvalues equal to only 0 or 1, H is positive semi-definite, meaning that any state with an energy equal to zero is a ground state of H. Such states do exist and were originally formulated in Ref. [20]. To construct the exact ground states of H, each spin-1 site is described by a pair of spins 1/2 whose state is restricted to the triplet state basis. We note the triplet states by

$$|\Phi_{\alpha\beta}\rangle = \frac{1}{\sqrt{2}}\left(|\alpha\rangle \otimes |\beta\rangle + |\beta\rangle \otimes |\alpha\rangle\right), \tag{3.4}$$

where $\alpha, \beta = 0/1$ denote the eigenstates of S^z with eigenvalue $\pm 1/2$. Note that in this formulation $|\Phi_{\alpha\beta}\rangle$ do not have a norm of 1: $|\Phi_{00}\rangle = \sqrt{2}\,|00\rangle$, $|\Phi_{11}\rangle = \sqrt{2}\,|11\rangle$ and $|\Phi_{01}\rangle = |\Phi_{10}\rangle = \frac{1}{\sqrt{2}}(|01\rangle + |10\rangle)$. We then consider a chain of L spin-1 sites composed of $2L$ spin-1/2's. Two neighboring spin-1s indexed by i and $i+1$ are therefore described by 4 spins of 1/2. By putting two of these spin-1/2's in a singlet state $|\alpha\rangle \otimes |\beta\rangle\, \epsilon^{\alpha\beta}$ (where $\epsilon^{\alpha\beta}$ denotes the antisymmetric tensor with $\epsilon^{01} = 1$) with a total spin 0, we guarantee that 4 spin-1/2's cannot possess a total spin greater than 1. Therefore, we can construct the exact ground state of H by creating a singlet bound state between two spin-1/2's from two neighboring spin-1 sites, while ensuring that each pair of spin-1/2's forming a spin-1 remains in a symmetric triplet state. We denote $|\Omega_{\alpha\beta}\rangle$ the ground state of H, with α, β label the state of the two spins of 1/2 at both extremities of the chain, defined as

$$|\Omega_{\alpha\beta}\rangle \propto |\Phi_{\alpha\beta_1}\rangle \otimes |\Phi_{\alpha_2\beta_2}\rangle \otimes ... \otimes |\Phi_{\alpha_L\beta}\rangle\, \epsilon^{\beta_1\alpha_2}\epsilon^{\beta_2\alpha_3}...\epsilon^{\beta_{L-1}\alpha_L}. \tag{3.5}$$

A diagrammatic representation of the ground state is shown in Fig. 3.1. Each spin-1/2 of a given site forms a singlet with a spin-1/2 belonging to a neighboring site while the two spin-1/2's of each site are being symmetrized by a projection onto the triplet subspace.

This can be extended to a closed chain with periodic boundary conditions by creating a singlet between the two edge spin-1/2's, leading to the state $|\Omega\rangle = |\Omega_{\alpha\beta}\rangle\, \epsilon^{\beta\alpha}$.

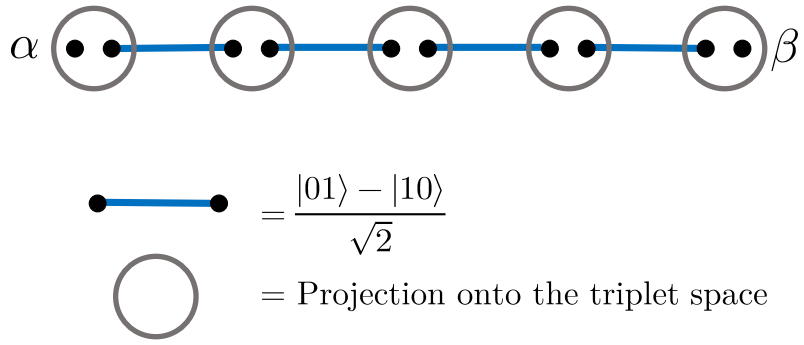

Figure 3.1: The AKLT state is a product of singlet states. Each pair of spin-1/2's is then projected onto the triplet subspace.

3.3 Projection by Quantum Phase Estimation

As explained in the previous chapter, the Quantum Phase Estimation (QPE) [56] algorithm allows to access the eigenvalue associated with an eigenvector $|\Psi\rangle$ of a unitary matrix U by entangling the input state with a register of ancilla qubits. When $|\Psi\rangle$ is a linear combination of eigenstates of U, measuring the ancilla qubit register will make $|\Psi\rangle$ collapse onto the eigenspace corresponding to the measured phase value. In Refs. [115, 116], it was proposed to use the QPE algorithm to project a state $|\Psi\rangle$ onto a specific eigenspace of a symmetry operator U. In the following paragraph, we describe in detail how this procedure allows us to discriminate between the singlet and triplet states of two qubits.

Let us consider two spin-1/2's (or qubits) in a state $|\varphi\rangle = c_0 |\varphi_0\rangle + c_1 |\varphi_1\rangle$ which is in a mixture of a singlet state $|\varphi_0\rangle = \frac{|01\rangle - |10\rangle}{\sqrt{2}}$ and a $S = 1$ triplet state $|\varphi_1\rangle$, which is itself a superposition of the three triplet states $|00\rangle, |11\rangle, \frac{|01\rangle + |10\rangle}{\sqrt{2}}$. The total spin operator S^2 for a pair of qubits is defined by

$$\begin{aligned} S^2 &= (\mathbf{S}_1 + \mathbf{S}_2)^2 \\ &= \frac{3}{2} I + \frac{1}{2}(X_1 X_2 + Y_1 Y_2 + Z_1 Z_2), \end{aligned} \tag{3.6}$$

where $\mathbf{S}_i = (S_i^x, S_i^y, S_i^z) = \frac{1}{2}(X_i, Y_i, Z_i)$ is the spin operator vector of spin-1/2 i, and X, Y and Z are the Pauli matrices. We defined the unitary SWAP gate by $\text{SWAP}\,|\alpha\rangle\,|\beta\rangle = |\beta\rangle\,|\alpha\rangle$. The SWAP gate has two eigenvalues ± 1 associated to the symmetric states ($S = 1$ states) and antisymmetric states ($S = 0$ state) respectively (one can note that $\text{SWAP} = -e^{i\pi S^2/2}$).

Here we describe how a SWAP gate controlled by an ancilla qubit (a cSWAP gate) can be used to project 2 qubits onto a specific spin subspace. Let us apply a cSWAP gate on to $|\varphi\rangle$ with the ancilla qubit steered in the $|+\rangle = \frac{|0\rangle+|1\rangle}{\sqrt{2}}$ state:

$$\begin{aligned}\text{cSWAP}\left(|+\rangle \otimes |\varphi\rangle\right) = &\frac{c_1}{\sqrt{2}}(|0\rangle + |1\rangle) \otimes |\varphi_1\rangle \\ &+ \frac{c_0}{\sqrt{2}}(|0\rangle - |1\rangle) \otimes |\varphi_0\rangle\,. \end{aligned} \tag{3.7}$$

Then, we perform a Hadamard gate onto the ancilla, which maps $|+\rangle$ to $|0\rangle$ and $|-\rangle = \frac{|0\rangle-|1\rangle}{\sqrt{2}}$ to $|1\rangle$, leading to the final state

$$|\tilde{\varphi}\rangle = c_0\,|1\rangle \otimes |\varphi_0\rangle + c_1\,|0\rangle \otimes |\varphi_1\rangle\,. \tag{3.8}$$

Finally, the ancilla qubit is measured in the $\{|0\rangle, |1\rangle\}$ basis. Measuring 1 projects the

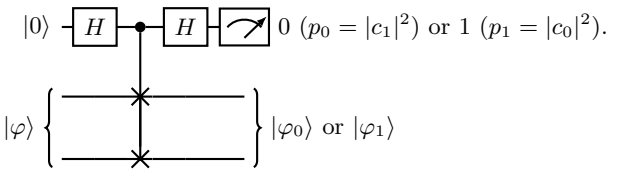

Figure 3.2: Schematic of circuit operating the projection onto the singlet or triplet subspace.

physical state $|\varphi_0\rangle$ into $|\varphi_1\rangle$ while measuring 0 projects into $|\varphi_0\rangle$. Therefore, the measurement of the ancilla qubit effectively performs a projection into the singlet or triplet subspace, with respective probabilities $|c_0|^2$ and $|c_1|^2$. The output of the measurement allows to discriminate between the two cases. Fig. 3.2 shows the corresponding quantum circuit to operate the projection.

3.4 Application to the 1D AKLT state

Now, we can expand this algorithm to a larger number of qubits in order to prepare the 1D AKLT state. We index the L spin-1's with the index $i \in [0, L-1]$ composed by two qubits labelled by $(2i, 2i+1)$. We prepare an initial state $|S_{\alpha\beta}\rangle$ as a product of singlet states formed between two neighboring qubits from two different spin-1 sites as

$$|S_{\alpha\beta}\rangle = |\alpha\rangle \otimes_{i=0}^{L-1} |s_{2i+1,2i+2}\rangle \, |\beta\rangle \,, \tag{3.9}$$

where $|\alpha\rangle$ and $|\beta\rangle$ are the states of the two qubits located at both ends and $|s_{n,m}\rangle$ is a singlet state formed between qubits n and m. Then, applying the scheme described above for each spin site i, we can project each pair of qubits onto their triplet subspace with a certain probability. We define the event $\mathcal{S}$ of successfully projecting all spin sites. The probability of obtaining $\mathcal{S}$, noted $p_{\mathcal{S}}$, is given by the overlap between the AKLT state $|\Omega_{\alpha\beta}\rangle$ and the initial state $|S_{\alpha\beta}\rangle$ as (see Appendix 3.8.1.1 for calculations details)

$$\begin{aligned} p_{\mathcal{S}} &= |\langle \Omega_{\alpha\beta} | S_{\alpha\beta} \rangle|^2, \\ &= \Big(\frac{1}{2}\Big)^{2L-1} \Big(\frac{3^L - 1}{2} + \delta_{\alpha\beta}\Big) \text{ for } L \text{ odd}, && (3.10) \\ &= \Big(\frac{1}{2}\Big)^{2L-1} \Big(\frac{3^L + 1}{2} - \delta_{\alpha\beta}\Big) \text{ for } L \text{ even}, && (3.11) \\ &\sim \Big(\frac{3}{4}\Big)^{L} \text{ for } L \gg 1. && (3.12) \end{aligned}$$

In a situation where L ancilla qubits are used to project the L qubit pairs and are all measured at once, we can define the average number of repetitions $N_{\mathcal{S}} = 1/p_{\mathcal{S}}$ needed to successfully project the initial state onto the AKLT ground state thanks to an average number of local projection N_P equals to $N_{\mathcal{S}} \times L$. However, the projection of a qubit pair is a local projection, and projecting two disconnected chains can be done independently and in parallel. We can therefore define two even sets of qubits A and B (each containing L_A and L_B pairs of qubits) interconnected with two-qubit spin-1 states. Those states are described as

$$|\omega_\alpha\rangle \propto |\Phi_{\alpha\beta_1}\rangle \otimes ... \otimes |\Phi_{\alpha_L\beta_L}\rangle \otimes |\alpha_{L+1}\rangle \, \times \epsilon^{\beta_1\alpha_2} ... \epsilon^{\beta_{L-1}\alpha_L} \epsilon^{\beta_L\alpha_{L+1}}. \tag{3.13}$$

Those two additional qubits will be the last projected pair of qubits to form an AKLT state of length $L = L_A + L_B + 1$, as depicted in Fig. 3.3a. The probability of successfully projecting the last pair is noted p_f. We call the events of successfully projecting A and B as $\mathcal{S}_A$ and $\mathcal{S}_B$. Therefore, the total success probability can be written as

$$p_{\mathcal{S}} = p_{\mathcal{S}_A} p_{\mathcal{S}_B} p_f. \tag{3.14}$$

Let us call $|\omega_\alpha^A \otimes \omega_\beta^B\rangle$ the normalized state describing two projected sub-chains of lengths L_A and L_B as described by Eq. (3.13) (see Appendix 3.8.1.1):

$$\begin{aligned} p_f &= |\langle \Omega_{\alpha\beta} | \omega_\alpha^A \otimes \omega_\beta^B \rangle|^2, \\ &= \frac{1}{2}\Big(\frac{3}{2} + \frac{\delta_{\alpha\beta} - 1/2}{3^{L-1}}\Big) \text{ for } L \text{ odd}, && (3.15) \\ &= \frac{1}{2}\Big(\frac{3}{2} - \frac{\delta_{\alpha\beta} - 1/2}{3^{L-1}}\Big) \text{ for } L \text{ even}, && (3.16) \\ &\sim \frac{3}{4} \text{ for } L \gg 1. && (3.17) \end{aligned}$$

For periodic boundary conditions, we divide the chain into 2 open sub-chains, as shown in Fig3.3b. The qubit on the left-hand side of chain A is connected by the qubit on the left-hand side of chain B, by forming a triplet state. Likewise, the qubit on the right-hand side of chain A is connected by the qubit on the right-hand side of chain B, by forming a triplet state. The sub-chains are described by

$$|\omega\rangle \propto |\beta_0\rangle\, |\Phi_{\alpha_1\beta_1}\rangle \otimes ... \otimes |\Phi_{\alpha_L\beta_L}\rangle \otimes |\alpha_{L+1}\rangle \times \epsilon^{\beta_0\alpha_1}\epsilon^{\beta_1\alpha_2}...\epsilon^{\beta_{L-1}\alpha_L}\epsilon^{\beta_L\alpha_{L+1}}. \tag{3.18}$$

The probability of successfully projecting the last two sites connecting the two ends of two subchains $|\omega^A\rangle$ and $|\omega^B\rangle$ reads as

$$\begin{aligned} p_f &= |\langle \Omega | \omega^A \otimes \omega^B \rangle|^2, \\ &= \frac{9}{16}(1 - \frac{1}{3^{L-1}}) \text{ for } L \text{ odd}, && (3.19) \\ &= \frac{9}{16}(1 + \frac{1}{3^{L-1}}) \text{ for } L \text{ even}, && (3.20) \\ &\sim \frac{9}{16} \text{ for } L \gg 1. && (3.21) \end{aligned}$$

It should be noted that because of periodic boundary conditions, the full chain $|\Omega\rangle$ does not have dangling edge spin-1/2's, thus $\left|\omega^A\right\rangle$ and $\left|\omega^B\right\rangle$ appear without subscripts α and β.

To better estimate the number of repetitions needed to produce the AKLT state, we define an effective number of projections $\tilde{N}_P$ needed. For an open chain, it can be defined as the number of repetitions needed to successfully project the final site multiplied by the average number of repetitions needed to project the two sub-chains of size L_A and L_B as

$$\tilde{N}_P(L) = (1/p_f) \times (\tilde{N}_P(L_A) + \tilde{N}_P(L_B) + 1). \tag{3.22}$$

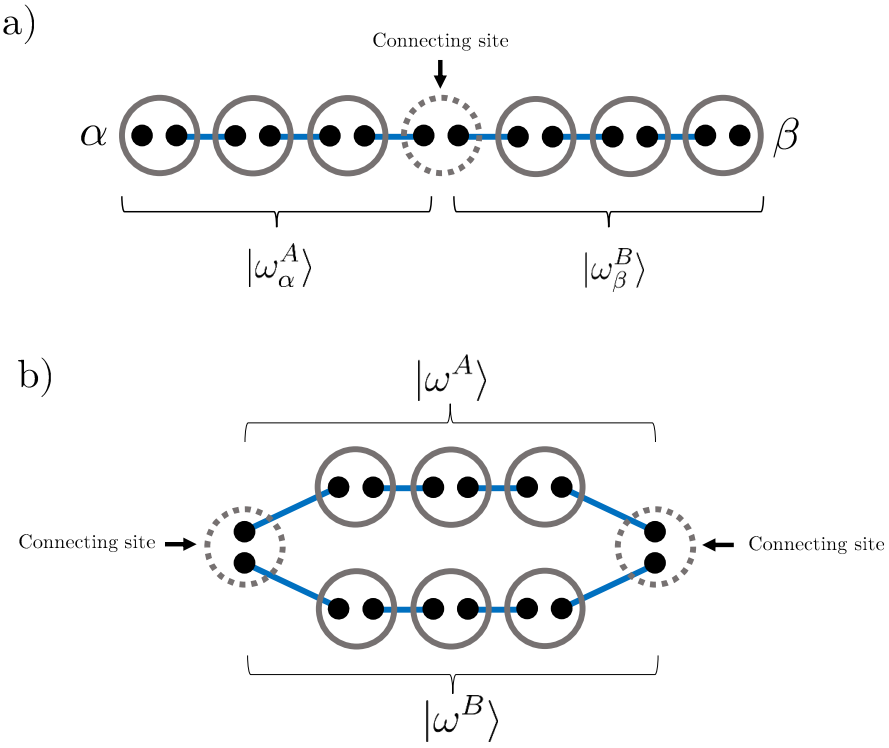

Figure 3.3: Schematic of the two subchains forming an AKLT state after projection of the connecting sites for (a) open boundary conditions and (b) periodic boundary conditions.

Similarly, for a closed chain, $\tilde{N}_P$ is defined as the average number of projections needed to project two sub-chains of size L_A and L_B (here $L = L_A + L_B + 2$) multiplied by the number of repetitions needed to successfully project the last two connecting sites. It can be calculated as

$$\tilde{N}_P(L) = (1/p_f) \times (\tilde{N}_P(L_A) + \tilde{N}_P(L_B) + 2). \tag{3.23}$$

A schematic of the procedure is shown in Fig. 3.4. In Table 3.1, we compare the average number of projections needed to successfully prepare AKLT states as a function of the boundary conditions with and without parallel projections for $L = 10$, 30, 60, and 100 spin sites. We observe that taking advantage of parallel projections drastically reduces the number of repetitions needed by several orders of magnitude, and makes this scheme feasible for large system sizes.

L	α, β	N_P	$\tilde{N}_P$
10	0,0	178	29
	1,0	178	24
	closed	178	16
30	0,0	1.68×10^5	81
	1,0	1.68×10^5	83
	closed	1.68×10^5	68
60	0,0	1.88×10^9	219
	1,0	1.88×10^9	221
	closed	1.88×10^9	181
100	0,0	3.12×10^{14}	633
	1,0	3.12×10^{14}	550
	closed	3.12×10^{14}	406

Table 3.1: Table comparing the average number of projection N_P and the average effective number of projection N_P needed to produce the 1D AKLT state for different lengths L and boundary conditions α, β.

3.5 Matrix Product State circuit

In this section we propose an alternative scheme to produce the open boundary AKLT state based on the Matrix Product State (MPS) formalism [23, 24]. MPSs will be introduced more extensively in the Chapter 4, but we make a concise overview here. Let us consider N spins living in a local Hilbert space $\mathcal{H}_{loc}$ of dimension d. Let $\{|\sigma\rangle\}$ be an orthonormal basis of $\mathcal{H}_{loc}$. A general many-body state $|\Psi\rangle$ living in $\mathcal{H} = \bigotimes_{i=1}^{N} \mathcal{H}_{loc}$ can be written as:

$$|\Psi\rangle = \sum_{\sigma_1,...,\sigma_N} \Psi_{\sigma_1...\sigma_N} |\sigma_1...\sigma_N\rangle \,, \tag{3.24}$$

where $\Psi_{\sigma_1...\sigma_N} \in \mathbb{C}$ and $|\sigma_1...\sigma_N\rangle = |\sigma_1\rangle \otimes ... \otimes |\sigma_N\rangle$. A MPS is a class of quantum many-body states where the coefficients $\Psi_{\sigma_1...\sigma_N}$ are obtained by contracting matrices $\{A_n^{\sigma_n}\}$ together [117, 118]. For an open boundary state, a MPS reads as:

$$|\Psi_{\text{MPS}}\rangle = \sum_{\{\sigma_n\}} \sum_{\{\alpha_n\}} A_{\alpha_1}^{[1]\sigma_1} A_{\alpha_1\alpha_2}^{[2]\sigma_2} ... A_{\alpha_N}^{[N]\sigma_N} |\sigma_1\sigma_2...\sigma_N\rangle \,, \tag{3.25}$$

where $A^{[n]\sigma_n}$ for $2 \leq n \leq N-1$ are complex matrices of dimension $\chi_{n-1} \times \chi_n$, where χ_n is called the bond dimension. At the boundaries, the tensors $A^{[1]\sigma_1}$ and $A^{[N]\sigma_N}$ are vectors of dimension χ_1 and χ_{N-1}. A MPS can be written into an orthogonal form by choosing the tensors to be orthogonal. Here we focus on the right-orthogonal form which corresponds to the following constraints on the A tensors:

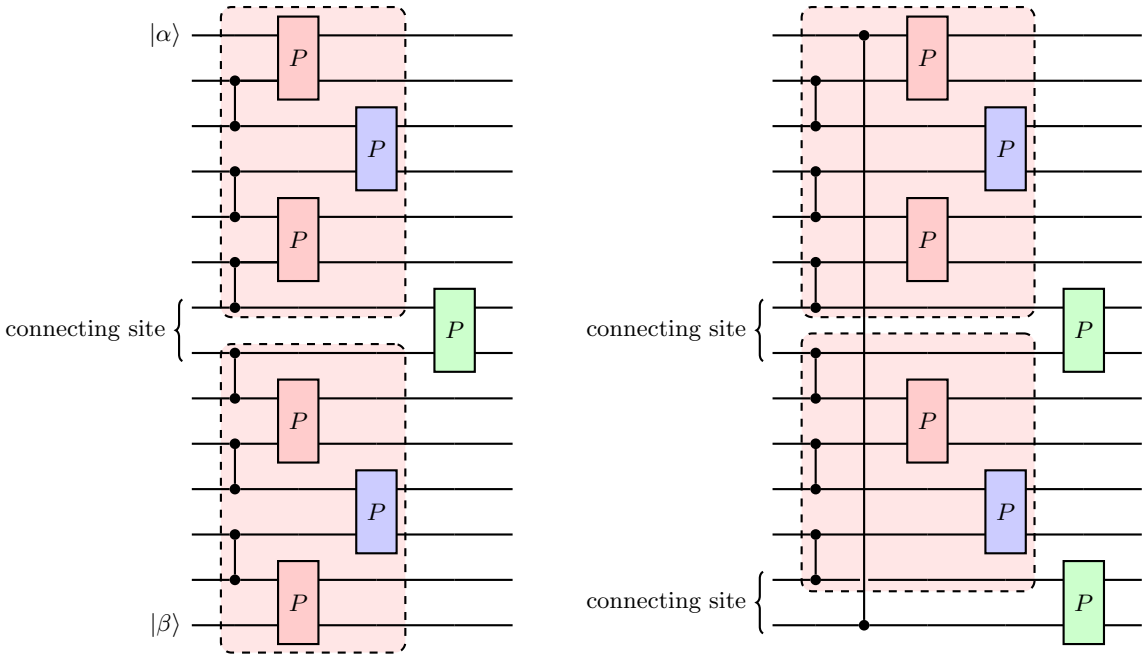

(a) Open chain with $L = 7$ sites

(b) Closed chain with $L = 7$ sites

Figure 3.4: Circuit with projectors denoted by the gate P (ancilla qubits are not displayed for clarity). The two red shared boxes show the subsets A and B that can be prepared in parallel and independently. Each gate P of the same color can be performed in parallel. The final site f is the last site to be projected (green P gate here). This is the only projection that requires a full reset of the state in case of a fail.

$$\sum_{\sigma_n} A^{[n]\sigma_n} A^{[n]\sigma_n \dagger} = \mathbb{1}. \tag{3.26}$$

For the 1D-AKLT state, the right-normalized tensors corresponding to the three S^z eigenstates $|+1\rangle, |\tilde{0}\rangle$ and $|-1\rangle$ read

$$A^{+1} = \sqrt{\frac{2}{3}} \begin{pmatrix} 0 & 1 \\ 0 & 0 \end{pmatrix} \ , \ A^{\tilde{0}} = \sqrt{\frac{1}{3}} \begin{pmatrix} -1 & 0 \\ 0 & 1 \end{pmatrix}, \tag{3.27}$$

$$A^{-1} = \sqrt{\frac{2}{3}} \begin{pmatrix} 0 & 0 \\ -1 & 0 \end{pmatrix}. \tag{3.28}$$

At the boundaries, the corresponding tensors read as

$$A^{[1]\sigma} = v^T A^\sigma, \tag{3.29}$$

where $v = \begin{pmatrix} 1 \\ 0 \end{pmatrix}$ if one choose the free spin-1/2 to be in the state $|0\rangle$ or $\begin{pmatrix} 0 \\ 1 \end{pmatrix}$ if we choose it to be in $|1\rangle$. The last site tensor corresponds to a projection onto the triplet subspace:

$$A^{[N]\sigma} = P^{\sigma} v, \tag{3.30}$$

where

$$P^{+1} = \begin{pmatrix} 1 & 0 \\ 0 & 0 \end{pmatrix}, P^{\tilde{0}} = \frac{1}{\sqrt{2}} \begin{pmatrix} 0 & 1 \\ 1 & 0 \end{pmatrix}, P^{-1} = \begin{pmatrix} 0 & 0 \\ 0 & 1 \end{pmatrix}. \tag{3.31}$$

The encoding of MPS in quantum circuits has been recently applied in [119, 120, 121, 122, 123, 124, 125], and will also be further introduced in Chapter 4. This offers a promising pathway to extend efficient classical methods beyond their limitations, such as performing time evolution or representing highly entangled states. To implement the AKLT state as a MPS on a qubit-based quantum computer, we choose to represent the physical spin-1 sites by using two qubits per site with the following mapping: $|+1\rangle = |00\rangle, |\tilde{0}\rangle = |01\rangle, |-1\rangle = |11\rangle$. The last state $|10\rangle$ is attributed to the singlet state $|S\rangle$ which is unphysical when representing spin-1 states. We therefore assign a tensor A^S to the singlet state that we set equal to $\begin{pmatrix} 0 & 0 \\ 0 & 0 \end{pmatrix}$. We embed those tensors into 3-qubit gates applied to a reference state as shown in Fig. 3.5, where two qubits are used to represent the physical spin-1 sites while 1 qubit encodes the bond state. The corresponding unitary matrix U encoding the tensors $A^{\sigma}_{\alpha_{n-1}\alpha_n}$ is defined as:

$$U = \sum_{\sigma_n \gamma} \sum_{\alpha_{n-1}\alpha_n} U_{(i \otimes \alpha_{n-1}),(\alpha_n \otimes \gamma)} \, |\sigma_n, \alpha_{n-1}\rangle \langle \alpha_n, \gamma|, \tag{3.32}$$

with $A^{\sigma} = U_{(i \otimes \alpha_{n-1}),(\alpha_n \otimes +1)}$ and the physical indices σ_n, γ are composed indices representing the 2-qubit states. The other matrix coefficients are to be defined up to the unitary constraints. In this work, they were calculated numerically as the tangent subspace of the tensors A^{σ}.

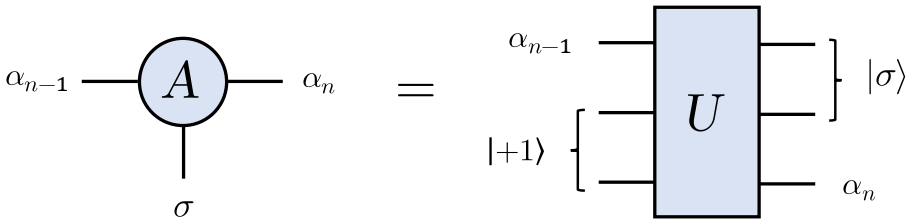

Figure 3.5: The tensors are mapped into a 3-qubit gate applied onto a reference state.

However, the last tensors $A^{[N]}$ cannot be performed by a unitary transformation as it performs a projection onto the subspace $\{|00\rangle, |01\rangle, |11\rangle\}$ from the 2-qubit Hilbert space. To circumvent this, we effectively perform this projection by using an ancilla qubit. Let us first write a general form of the state before applying the projection on the last site:

$$|\Psi\rangle = |\Psi_0\rangle |00\rangle + |\Psi_1\rangle |10\rangle , \tag{3.33}$$

where $|\Psi_0\rangle$ ($|\Psi_1\rangle$) is the state representing the first $N-1$ spin sites entangled with the bond state $|0\rangle$ ($|1\rangle$). The incoming reference state for the last qubit is chosen to be $|0\rangle$. From this, we see that we must perform the following operation: $|00\rangle \to |00\rangle$ and $|10\rangle \to \frac{1}{\sqrt{2}} |01\rangle$. We start by applying onto the 2 qubits representing the last spin site U_N defined as

$$U_N = \begin{pmatrix} 1 & 0 & 0 & 0 \\ 0 & \frac{1}{\sqrt{2}} & \frac{1}{\sqrt{2}} & 0 \\ 0 & -\frac{1}{\sqrt{2}} & \frac{1}{\sqrt{2}} & 0 \\ 0 & 0 & 0 & 1 \end{pmatrix} . \tag{3.34}$$

After applying U_N, we obtain

$$\underbrace{\left\{ |\Psi_0\rangle |00\rangle + |\Psi_1\rangle \sqrt{\frac{1}{2}} |01\rangle \right\}}_{\text{what we want}} + \underbrace{\left\{ |\Psi_1\rangle \sqrt{\frac{1}{2}} |10\rangle \right\}}_{\text{unphysical}} . \tag{3.35}$$

The undesired state differs from the physical one by the state of the first qubit representing the last spin site as shown in red in Eq. 3.35. We entangle this state with an ancilla qubit in the $|+\rangle$ state by performing a CZ gate (a Z gate controlled by a second qubit) between the two qubits. Finally, after applying a Hadamard gate onto the ancilla, we obtain the following state:

$$|\Psi_{\text{tot}}\rangle = \underbrace{\left\{ |\Psi_0\rangle |00\rangle + |\Psi_1\rangle \sqrt{\frac{1}{2}} |01\rangle \right\}}_{\text{what we want}} |0\rangle + \underbrace{\left\{ |\Psi_1\rangle \sqrt{\frac{1}{2}} |10\rangle \right\}}_{\text{unphysical}} |1\rangle . \tag{3.36}$$

Therefore, measuring the ancillary qubit in the Z-basis allows us to obtain the AKLT state if the measurement output is 0. The probability p of measuring 0 corresponds is related to the overlap between a fully projected AKLT chain of size L and an AKLT chain where the spin-1 site at one end has not been projected yet. Fig. 3.6 shows the corresponding

circuit. Using Eqs. 3.5 and 3.13, we calculate the probability p as (see Appendix 3.8.1.2)

$$p = |\langle \Omega_{\alpha\beta} | \omega_\alpha \otimes \beta \rangle|^2, \tag{3.37}$$

$$= \frac{3}{4}(1 - \frac{1}{3^{L-2}}) + \frac{1}{2 \times 3^{L-1}} \delta_{\alpha\beta} \text{ for } L \text{ odd }, \tag{3.38}$$

$$= \frac{3}{4}(1 - \frac{1}{3^{L-2}}) + \frac{1}{2 \times 3^{L-1}} (1 - \delta_{\alpha\beta}) \text{ for } L \text{ even}, \tag{3.39}$$

$$\sim \frac{3}{4} \text{ for } L \gg 1. \tag{3.40}$$

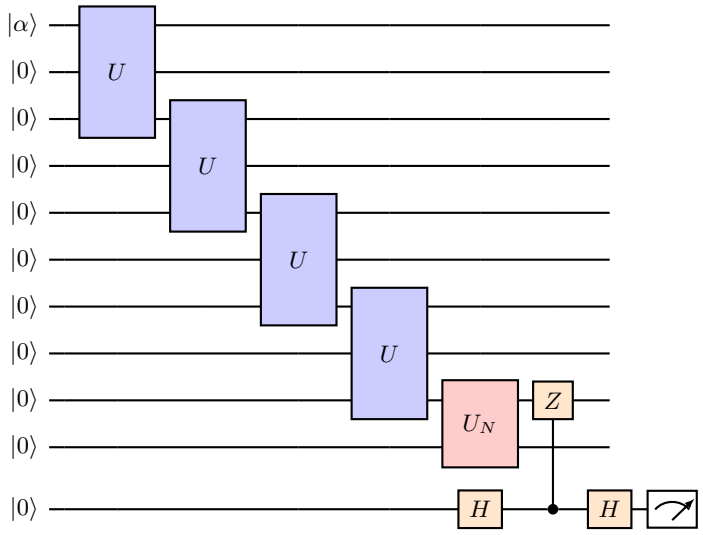

Figure 3.6: The MPS-inspired circuit to create an AKLT state of 5 sites. The state is successfully created if the measurement output of the ancilla is 0. The state of the first qubit $|\alpha\rangle$ define the boundary conditions of the states (same spin-1/2 states if $|\alpha\rangle = |0\rangle$ or opposite states if $|\alpha\rangle = |1\rangle$.

3.6 Comparison and experimental results

In this section, we compare the two methods detailed in the previous sections to prepare the AKLT state on a quantum computer. As both schemes require measurements of ancilla qubits, we compare the number of repetitions needed to successfully realize an AKLT state as a function of the chain size L. The number of repetitions needed is given by Eqs. 3.22 and 3.23 for the projective schemes. Fig. 3.7 shows that despite an exponential decrease of the overlap between the initial state composed out of singlets states with the projected AKLT state, it can still be obtained with a relatively low number of repetitions by preparing independent sub-chains. On the other hand, the MPS scheme needs only

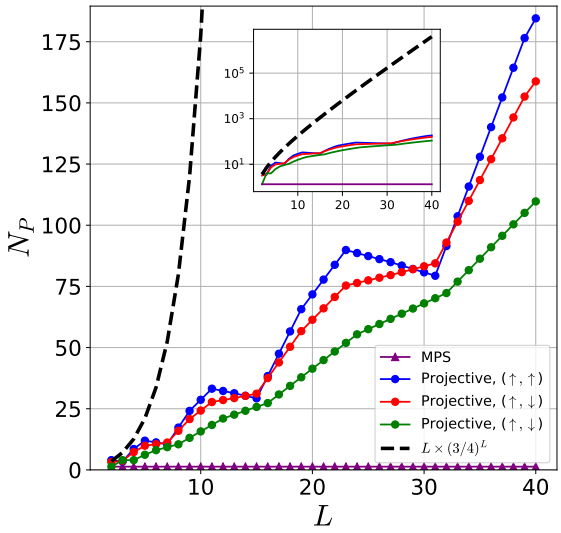

Figure 3.7: Number of repetitions N_P needed to produce the AKLT state as a function of the system size L for the different schemes. The inset shows the dependency on a log scale.

the measurement of one auxiliary qubit with a success probability $\sim 3/4$ when $L \gg 1$. Therefore, an average of $\sim 4/3$ repetitions is needed, providing a better scaling of the repetitions needed compared to the projective scheme.

With Fig. 3.8, we then compare the cost of the quantum circuits for both methods. To do so, we use the circuit transpiling tool from qiskit [6] to decompose the quantum circuits using CNOTs and one-qubit gates for a quantum computer with ideal connectivity (*i.e.* a topology that matches the circuit's connectivity) and for the device `ibmq_montreal` [6] that has 27 qubits. For all connectivities, the projective scheme requires less number of CNOTs than the MPS scheme. This can be explained by the decomposition of the gate U requiring 20 CNOTs while a cSWAP can be implemented with only 7 CNOTs. As the projective scheme requires one cSWAP per spin-1 site and the MPS scheme needs one U gate per site defined in Eq. 3.32 (expect for the last site where we use the U_N gate from Eq. 3.34). When implemented on a specific device, additional SWAP gates (decomposed as 3 CNOTs) are required to match its connectivity. By including the initial state preparation for the projective scheme and the last site projection for the MPS scheme, we can count the number of CNOTs gates for an ideal connectivity as:

$$N_{\text{CNOT}} = 7 \times L + L - 1 \text{ (Projection)}, \tag{3.41}$$

$$= 20 \times (L-1) + 3 \text{ (MPS)}. \tag{3.42}$$

Although the number of necessary repetitions increases significantly with the chain length,

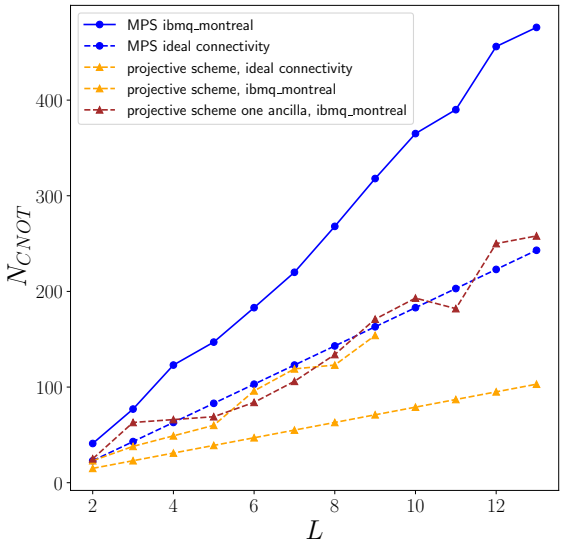

Figure 3.8: Number of CNOTs needed to realize the quantum circuits for the different schemes, obtained from the transpiled circuits from IBMQ.

the projection scheme can be a better candidate on small noisy quantum devices, where two-qubit gates are predominant sources of error. To test this, we implement both schemes on the 7-qubit IBM's `ibmq_lagos`, where we prepare 2-site AKLT states using 4 qubits and one ancilla qubit for the projection process for both the projective and MPS methods. To evaluate the quality of the resulting states, we perform quantum state tomography, which allows to reconstruct the density matrix of the state from the quantum device. The results are shown in Fig. 3.9. We compute the fidelity of the noisy state ρ with exact solutions $|\Psi_{\text{ex}}\rangle$ as $F = \langle\Psi_{\text{ex}}|\rho|\Psi_{\text{ex}}\rangle$. In these small instances, we indeed observe better fidelities from the projective method, which is explained by the cheaper circuit cost compared to the MPS method. However, for all the boundary conditions and preparation methods, we recover the main features of the exact density matrices.

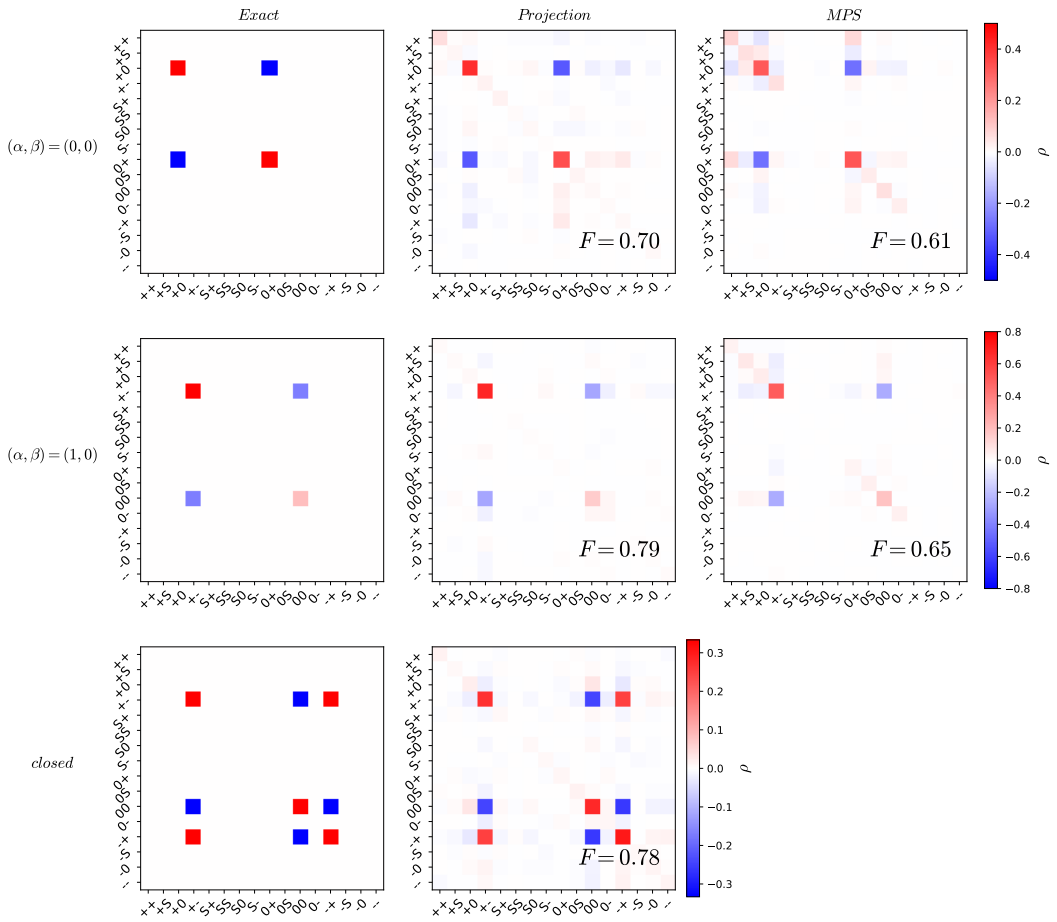

Figure 3.9: Experimental density matrices obtained by quantum state tomography from IBMQ's device `ibmq_lagos` for the two schemes and the different boundary conditions. The labels "+", "0", and "−" correspond to three triplet $S = 1$ states, and "S" to the singlet state.

3.7 Conclusion

We report two different methods to prepare the AKLT state on a digital quantum computer. The AKLT state describes an interacting antiferromagnetic spin-1 chain, where each spin is described by two spins of 1/2. Each spin-1/2 forms a singlet with a spin-1/2 from a neighboring spin-1 site, giving a valence-bound structure to the state. Each pair of spin-1/2's representing a spin-1 is then symmetrized and projected onto its $S = 1$ triplet state. Therefore, to encode a chain of L spin-1, we use $2L$ qubits, and form singlet states between neighboring qubits. Our first approach is based on a projective scheme to prepare the 1D AKLT state. It uses a SWAP operation controlled by an ancilla qubit acting on each qubit pair, which allows us to project onto the triplet by measuring the ancilla qubit with a probability of success. The second method we use is based on the MPS form of the AKLT state, which allows to design a quantum circuit embedding the associated tensors. We evaluate the average number of projections needed to successfully produce the AKLT state for both methods, as well as the required quantum resources. While the projective scheme requires a number of repetitions that scales weakly exponentially with the number of sites, it requires fewer CNOTs than the MPS scheme, the latest needing a constant number of repetitions as the system size gets larger. Finally, we test and validate our method on IBM Quantum's device `ibmq_lagos` by performing quantum state tomography on 2-site AKLT states and show that indeed the projective scheme produces states with higher overlaps with exact solutions at the cost of more circuit repetitions.

We believe that this work can have potential applications in testing and performing protocol of measurement-based quantum computation as the AKLT state can be used as a resource state, as well as the study of quantum spin-1 chains and their topological properties by quantum computing means. More, as detailed in the Appendix 3.8.2, the projective scheme can be extended to AKLT states on different lattice topologies. The methodology presented here can be utilized to create initial states for QPE, VQE, and QITE studies of spin-1 chains. We also acknowledge similar approaches that appeared during the conception of this work [126, 127, 128]. Ref. [126] takes inspiration of the MPS form of the AKLT states to elaborate a measurement-assisted protocol with constant depth circuits. Ref. [127] proposes similar approaches as our projective and MPS methods, with extended technical details. Ref. [128] performs an experimental benchmark of the projective method on a NISQ device.

3.8 Appendix

3.8.1 Probabilities calculation

3.8.1.1 Projective scheme

In the definition of the AKLT ground state $|\Omega_{\alpha\beta}\rangle$ given in Eq. 3.5, we note that $|\Omega_{\alpha\beta}\rangle$ does not have a norm of 1. From Ref. [20], we have that

$$\langle\Omega_{\gamma\delta}\,|\Omega_{\alpha\beta}\rangle = \frac{3^L-1}{2}\delta_{\alpha\gamma}\delta_{\beta\delta} + \delta_{\alpha\delta}\delta_{\beta\gamma} \text{ for } L \text{ odd}, \tag{3.43}$$

$$= \frac{3^L-1}{2}\delta_{\alpha\gamma}\delta_{\beta\delta} + \epsilon^{\alpha\beta}\epsilon^{\gamma\delta} \text{ for } L \text{ even}. \tag{3.44}$$

Therefore, the norm of $|\Omega_{\alpha\beta}\rangle$ is given by

$$\langle\Omega_{\alpha\beta}\,|\Omega_{\alpha\beta}\rangle = \frac{3^L-1}{2} + \delta_{\alpha\beta} \text{ for } L \text{ odd}, \tag{3.45}$$

$$= \frac{3^L-1}{2} + 1 - \delta_{\alpha\beta} \text{ for } L \text{ even}. \tag{3.46}$$

For a closed chain, we can evaluate the norm of the state from Eq. 3.43 as

$$\langle\Omega\,|\Omega\rangle = 3^L - 3 \text{ for } L \text{ odd} \tag{3.47}$$

$$= 3^L + 3 \text{ for } L \text{ even}. \tag{3.48}$$

To evaluate the effective number of projection processes needed to successfully prepare the AKLT state, we first define the probability $p_{\mathcal{S}}$ of successfully projecting each pair of spin-1/2's onto their triplet state from a singlet product state as defined in Eq. 3.9. The overlap between this initial state and the AKLT state is given by the overlap $\langle\Omega_{\alpha\beta}|S_{\alpha\beta}\rangle$ (up to normalization) as given by

$$\langle\Omega_{\alpha\beta}|S_{\alpha\beta}\rangle = \langle\Psi_{\alpha\beta'_1}|\alpha\beta_1\rangle\epsilon^{\beta'_1\alpha'_2}\epsilon^{\beta_1\alpha_2} \times ... \times \langle\Psi_{\alpha'_L\beta}|\alpha_L\beta\rangle\epsilon^{\beta'_{L-1}\alpha'_L}\epsilon^{\beta_{L-1}\alpha_L}. \tag{3.49}$$

As $\langle\Phi_{\alpha'\beta'}|\alpha\beta\rangle = \frac{1}{\sqrt{2}}(\delta_{\alpha\alpha'}\delta_{\beta\beta'} + \delta_{\alpha\beta'}\delta_{\alpha'\beta}) = \frac{1}{\sqrt{2}}\langle\Phi_{\alpha'\beta'}|\Phi_{\alpha\beta}\rangle$, we can rewrite Eq. 3.49 as:

$$\langle\Omega_{\alpha\beta}|S_{\alpha\beta}\rangle = \left(\frac{1}{\sqrt{2}}\right)^L\langle\Omega_{\alpha\beta}\,|\Omega_{\alpha\beta}\rangle\,. \tag{3.50}$$

Using Eqs. 3.45 and 3.50, we obtain the following expression of the probability $p_{\mathcal{S}}$ for a open chain

$$\begin{aligned} p_{\mathcal{S}} &= \frac{|\langle \Omega_{\alpha\beta}|S_{\alpha\beta}\rangle|^2}{|\langle \Omega_{\alpha\beta}|\Omega_{\alpha\beta}\rangle| \times |\langle S_{\alpha\beta}|S_{\alpha\beta}\rangle|} \\ &= \left(\frac{1}{2}\right)^{2L-1} |\langle \Omega_{\alpha\beta}|\Omega_{\alpha\beta}\rangle|, \end{aligned} \tag{3.51}$$

and for a closed chain we obtain that

$$\begin{aligned} p_{\mathcal{S}} &= \frac{|\langle \Omega|S\rangle|^2}{|\langle \Omega|\Omega\rangle| \times |\langle S|S\rangle|} \\ &= \left(\frac{1}{2}\right)^{2L} |\langle \Omega|\Omega\rangle|. \end{aligned} \tag{3.52}$$

To estimate the effective average number of projection required to producte the AKLT state, we need to calculate the probability p_f of successfully projecting of a spin site connecting two projected spin-1 chains as defined in Eq. 3.13. We first need to calculate the norm of the state $|\omega_\alpha\rangle$ as

$$\begin{aligned} \langle \omega_\alpha|\omega_\alpha\rangle = \langle \Phi_{\alpha\beta_1'}|\Phi_{\alpha\beta_1}\rangle \epsilon^{\beta_1'\alpha_2'}\epsilon^{\beta_1\alpha_2}\langle \Phi_{\alpha_L\beta_L'}|\Phi_{\alpha_L\beta_L}\rangle \epsilon^{\beta_{L-1}'\alpha_L'}\epsilon^{\beta_{L-1}\alpha_L}... \\ \times \langle \alpha_{L+1}'|\alpha_{L+1}\rangle \epsilon^{\beta_L'\alpha_{L+1}'}\epsilon^{\beta_L\alpha_{L+1}}. \end{aligned} \tag{3.53}$$

In the same spirit as in [20], this quantity can be calculated in a diagrammatic fashion as shown in Figure 3.10. We start by drawing the state $|\omega_\alpha\rangle$ twice. By applying the scalar product between the two $|\omega_\alpha\rangle$, i.e. $\langle \omega_\alpha|\omega_\alpha\rangle$, we can connect the two diagrams at each spin site in two different ways (see Figure 3.10a as $\langle \Phi_{\gamma\delta}|\Phi_{\alpha\beta}\rangle = \delta_{\gamma\alpha}\delta_{\delta\beta} + \delta_{\gamma\beta}\delta_{\delta\alpha}$. This will lead to two kinds of diagrams: diagrams containing a closed loop (see Figure 3.10b) and a unique diagram without a closed loop (see Figure 3.10c). To create a diagram with m loops, we need to choose m spin sites where the diagram will be closed, representing $\binom{L}{m}$ possibilities. As each loop represents the trace of the δ tensor $\delta_\alpha^\alpha = 2$, we can calculate the contribution of all diagrams containing loops as

$$\sum_{m=1}^{L} \binom{L}{m} 2^m = (1+2)^L - 1. \tag{3.54}$$

As the unique diagram without loop is simply be equal to $\delta_{\alpha\alpha} = 1$, we obtain that:

$$\langle \omega_\alpha|\omega_\alpha\rangle = 3^L. \tag{3.55}$$

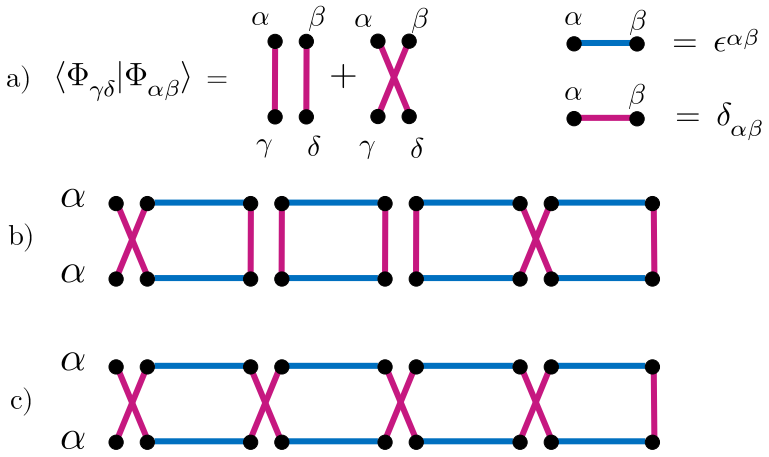

Figure 3.10: a) The scalar product at each spin site is as sum of two terms that connects the two diagrams. b) An example of a diagram with 2 loops which is equal to $\delta_{\alpha\alpha} \times 2^2$. c) The unique diagram without loop which is equal to $\delta_{\alpha\alpha} = 1$.

Finally, we consider two projected sub-chain of size L_A $|\omega_\alpha^A\rangle$ and L_B $|\omega_\alpha^B\rangle$. The state $|\omega_\alpha^A \otimes \omega_\alpha^B\rangle$ represents a chain of size $L = L_A + L_B + 1$ with one spin site not symmetrized yet. Therefore, it is straightforward to see that the overlap with the AKLT state of size L $|\Omega_{\alpha\beta}\rangle$ is given by $\langle\Omega_{\alpha\beta}|\omega_\alpha \otimes \omega_\beta\rangle = \frac{1}{\sqrt{2}}\langle\Omega_{\alpha\beta}|\Omega_{\alpha\beta}\rangle$. Therefore, the probability p_f can be calculated as

$$\begin{aligned} p_f &= \frac{|\langle\Omega_{\alpha\beta}|\omega_\alpha^A \otimes \omega_\beta^B\rangle|^2}{|\langle\Omega_{\alpha\beta}|\Omega_{\alpha\beta}\rangle| \times |\langle\omega_\alpha^A \otimes \omega_\beta^B|\omega_\alpha^A \otimes \omega_\beta^B\rangle|} \\ &= \frac{1}{2}\frac{|\langle\Omega_{\alpha\beta}|\Omega_{\alpha\beta}\rangle|}{|\langle\omega_\alpha^A \otimes \omega_\beta^B|\omega_\alpha^A \otimes \omega_\beta^B\rangle|} \\ &= \frac{|\langle\Omega_{\alpha\beta}|\Omega_{\alpha\beta}\rangle|}{2 \times 3^{L-1}}. \end{aligned} \tag{3.56}$$

For a closed chain, we proceed in a similar fashion and obtain that

$$\langle\omega|\omega\rangle = 2 \times 3^L, \tag{3.57}$$

which allows us to calculate the probability of projecting the two final sites connecting two sub-chains of size L_A and L_B to form a closed AKLT chain of length $L = L_A + L_B + 2$

as

$$\begin{aligned} p_f &= \frac{|\langle\Omega|\omega^A \otimes \omega^B\rangle|^2}{|\langle\Omega|\Omega\rangle| \times |\langle\omega^A \otimes \omega^B|\omega^A \otimes \omega^B\rangle|} \\ &= \frac{1}{4}\frac{|\langle\Omega|\Omega\rangle|}{|\langle\omega^A \otimes \omega^B|\omega^A \otimes \omega^B\rangle|} \\ &= \frac{|\langle\Omega|\Omega\rangle|}{16 \times 3^{L-2}}. \end{aligned} \tag{3.58}$$

3.8.1.2 MPS scheme

The probability p of successfully producing the AKLT state from the MPS scheme by measuring the unique ancilla qubit is equal to the probability of projection of the end site from a chain of size L with all spin sites projected but the last site on one end. Using Eq. 3.13, we define such state as

$$|\omega_{\alpha\beta}\rangle = |\omega_\alpha \otimes \beta\rangle\,. \tag{3.59}$$

Using Eqs. 3.55 and 3.59, we can write p as

$$\begin{aligned} p &= \frac{|\langle\Omega_{\alpha\beta}|\omega_{\alpha\beta}\rangle|^2}{|\langle\Omega_{\alpha\beta}|\Omega_{\alpha\beta}\rangle||\langle\omega_{\alpha\beta}|\omega_{\alpha\beta}\rangle|} \\ &= \frac{1}{2}\frac{|\langle\Omega_{\alpha\beta}|\Omega_{\alpha\beta}\rangle|}{|\langle\omega_{\alpha\beta}|\omega_{\alpha\beta}\rangle|} \\ &= \frac{1}{2}\frac{|\langle\Omega_{\alpha\beta}|\Omega_{\alpha\beta}\rangle|}{3^{L-1}}. \end{aligned} \tag{3.60}$$

3.8.2 Projection by Quantum Phase Estimation for S spin

Here we give details for the projection scheme in the case of using n qubits to represent a site with spin S. Let us consider n spin-1/2 or qubits. Each spin-1/2 possesses a spin vector operator defined a $\mathbf{S}_i = (S_i^x, S_i^y, S_i^z) = \frac{1}{2}(X_i, Y_i, Z_i)$, where X, Y and Z are the Pauli matrices. We can then define the total spin operator of the n spin-1/2's as

$$\begin{aligned} S^2 &= \left(\sum_{i=0}^{n-1} \mathbf{S}_i\right)^2 \\ &= \frac{3n}{4}I + \frac{1}{2}\sum_{i\neq j}(X_iX_j + Y_iY_j + Z_iZ_j). \end{aligned} \tag{3.61}$$

In order to project onto a specific spin subspace of the n qubits, we define the following unitary U as

$$U = e^{i2\pi S^2/\gamma + \phi_c}. \tag{3.62}$$

The eigenvalues of U are $\{e^{i2\pi S(S+1)/\gamma+\phi_c}\}$ for $S = 0, 1, ..., n/2$ for $n \geq 2$ even and $S = \frac{n}{2}$ for $n \geq 1$ odd. We note $\varphi_S = S(S+1)/\gamma + \phi_c$. Let us suppose that we want to project onto the specific subspace with total spin S^*. We want to find γ so that it is possible to distinguish between the different spin subspaces with a minimal number t of register qubits in the quantum phase estimation routine. We first define the phase difference between two spin value S and J as

$$\Delta\varphi(S, J) = |\phi_S - \phi_J| - \lfloor |\phi_S - \phi_J| \rfloor, \tag{3.63}$$

where $\lfloor . \rfloor$ defines the lower integer part.

The phase difference between the eigenphases associated with 2 different values of total spin needs to be greater than the resolution of the algorithm $\delta = 1/2^{t+1}$:

$$\Delta\varphi(S^*, S) > \frac{1}{2^{t+1}} \ \forall S \neq S^*. \tag{3.64}$$

3.8.2.1 3/2 AKLT state

This projective scheme can used to prepare AKLT states on a honeycomb lattice with spin-3/2's. Let us consider a spin-3/2 site composed by 3 spin-1/2's as depicted in 3.11. The total spin value can be either $S(S+1) = 15/4$ or $S(S+1) = 3/4$. Similary, we can define the unitary transformation

$$U = e^{i\pi(S^2 - 3/4)}. \tag{3.65}$$

U possesses then two eigenvalues, -1 if applied onto a $S = 3/2$ three qubit state or 1 if $S = 1/2$. Therefore, by applying U controlled by an ancilla qubit, we can project in a similar fashion the three qubit onto the $S = 3/2$ subspace.

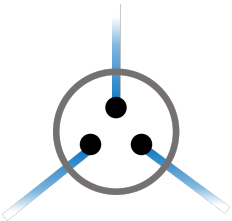

Figure 3.11: 3 qubits, forming valence singlet bound with neighbouring qubits, projected onto the 3/2 spin subspace.

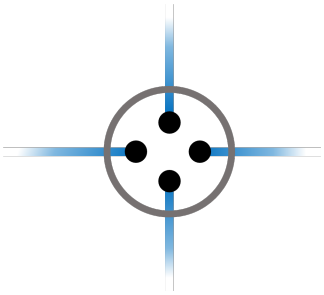

Figure 3.12: 4 qubits, forming valence singlet bound with neighboring qubits, projected onto the spin-1 subspace.

3.8.2.2 2D AKLT state

Let us consider the 2D AKLT state on a square lattice where each spin site possesses 4 neighbors and is therefore composed of 4 spin-1/2's. Similarly, each spin-1/2 is put in a maximally entangled singlet state with a neighboring spin-1/2 (see Fig. 3.12). We define the following unitary

$$U = e^{i2\pi S^2/3}, \tag{3.66}$$

where S^2 is the total spin operator for the 4 spin-1/2 system. For 4 spin-1/2's, the total spin can be $S = 0, 1$ or 2, so that $S^2 = S(S+1) = 0, 2$ or 6. Therefore, U has two eigenvalues: $e^{i2\pi\times 2/3}$ and $e^{i2\pi\times 0/3} = e^{i2\pi\times 6/3} = 1$. Let us decompose into binary fractions the two different phase associated to the two eigenvalues of U:

- $\varphi_0 = \varphi_2 = 0 = 0 \times \frac{1}{2}$.
- $\varphi_1 = \frac{2}{3} = 1 \times \frac{1}{2} + \delta$, $\delta = \frac{1}{6}$.

Let's suppose that we have $|\psi\rangle = c_0 |u_0\rangle + c_1 |u_1\rangle + c_2 |u_2\rangle$, with $|u_n\rangle = |S = n\rangle$. After the QPE process, we obtain the following state:

$$\begin{aligned} |\Psi\rangle = |0\rangle \otimes (c_0 |u_0\rangle + c_2 |u_2\rangle) \\ + c_1 \frac{1}{N} \sum_{k,x=0}^{N-1} e^{i2\pi(\tilde{\varphi}_1 - x)k/N} e^{i2\pi\delta k} |x\rangle \otimes |u_1\rangle . \end{aligned} \tag{3.67}$$

with $N = 2^t = 2^1 = 2$, and $\tilde{\varphi}_1$ being the nearest integer to $2^t\varphi_1$, ie $2^t(\varphi_1 - \delta)$.

Therefore, if one wants to project $|\Psi\rangle$ onto the subspace $S = 1$ i.e. onto $|u_1\rangle$ by

measuring the register qubit, it will be successfully done with a probability $Pr(1)$ as

$$Pr(1) = |c_1|^2 \frac{1}{N^2} \left| \frac{1 - e^{i2\pi\delta N}}{1 - e^{i2\pi\delta}} \right|^2 \tag{3.68}$$

$$= |c_1|^2 \times \frac{3}{4} \text{ for } \delta = \frac{1}{6} \text{ and } N = 2^t = 2. \tag{3.69}$$

The corresponding circuit is shown in Fig. 3.13.

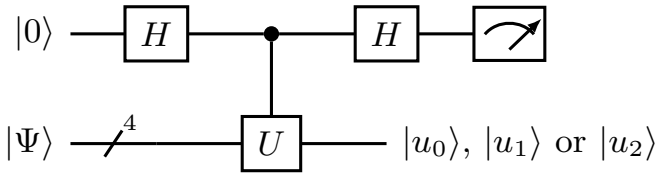

Figure 3.13: Schematic of circuit operating the projection onto one of the spin subspaces.

4 | Matrix Product States and Noisy Quantum Computers for Quantum Dynamics

4.1 Introduction

In this chapter, we address another endeavor of quantum many-body physics, namely the study of the dynamics of interacting spins. Given a quantum system described by an (time-independent) Hamiltonian H and a state $|\Psi\rangle$, studying the behavior of the system over time comes down to solving the Schrödinger equation

$$i\frac{\partial}{\partial t}|\Psi\rangle = H|\Psi\rangle\,. \tag{4.1}$$

Given an initial state $|\Psi_0\rangle$, the state describing the system at time t is calculated as

$$|\Psi(t)\rangle = e^{-iHt}|\Psi_0\rangle\,. \tag{4.2}$$

Assuming that $|\Psi_0\rangle$ is easy to prepare on a quantum computer, we can use a quantum device to implement the unitary transformation e^{-iHt} to perform the simulation in time of the quantum system of interest. Simulating quantum dynamics is a very natural task for a quantum computer as performing unitary evolution is at the heart of the quantum computing paradigm, and is believed to be one of the first applications of quantum computers. Algorithms have been proposed and tested to perform real-time simulation of many-body systems on a quantum computer [129, 130, 131, 132, 133, 134, 135, 136]. However, current devices still suffer from significant levels of noise, which strongly limits their capacities.

On the other hand, numerical computational techniques have been increasingly successful to study quantum systems. Among them, tensor networks provide an efficient

way to represent correlated quantum states [23, 25, 24, 26, 28, 29]. In one dimension, Matrix Product States (MPS) allow us to find ground states of local gapped Hamiltonian thanks to the famous density matrix renormalization group (DMRG) [137] algorithm or to simulate their dynamics with, for instance, the Time Evolution Block Decimation (TEBD) algorithm [76]. Moreover, tensor network techniques are competitive to simulate quantum computers in the presence of noise [14, 15, 138, 139]. However, physically relevant problems remain out of reach for state-of-the-art numerical methods, as they fail to represent highly entangled states. A prototypical example is the dynamics of global quenched quantum systems, where an initial state is abruptly driven by a Hamiltonian and is brought far-from-equilibrium. Such systems typically exhibit a ballistic growth of the entanglement with time [140, 141], implying that tensor network techniques can only access short-time dynamics.

In this chapter, we utilize the combination of MPS solutions that are tractable on a classical computer and quantum circuits on noisy quantum devices to study the dynamics of a paradigmatic spin chain Hamiltonian. After introducing the key concepts of MPS and their time-evolution in Sec.4.2, we detail the method used to optimize quantum circuits thanks to MPS in Sec. 4.3. In Sec. 4.4, we investigate the time evolution of a global quench in the one-dimensional transverse field Ising model where short-time simulations are performed by MPS techniques, leading to optimized quantum circuits that are extended for longer time simulations on a noisy quantum computer. To quantify our results, we use two metrics, the fidelity in Sec. 4.4.1 and the entanglement production in Sec. 4.4.2. In Sec. 4.5, noise mitigation techniques allow us to test our scheme on actual quantum devices from IBM Quantum [6]. Finally, in Sec. 4.6, we extend the QMPS approach by using tensor networks, namely Matrix Product Operators (MPO), to find more efficient circuits encoding the time-evolution operator, leading to a tensor-network-enhanced quantum simulation. This work is based on [142].

4.2 Matrix Product States and Time Evolution

4.2.1 Tensor networks, entanglement and rank of quantum states

Tensor networks offer a framework to manipulate high-dimensional data, stored in multi-dimensional arrays, or tensors, with a pictorial representation. Such data can be processed and operated on thanks to an efficient representation consisting of a network of interconnected tensors, each link corresponding to the sum over a common index. Fig. 4.1 shows simple examples of tensor contractions.

In quantum many-body physics, tensor networks allow to efficiently represent classes

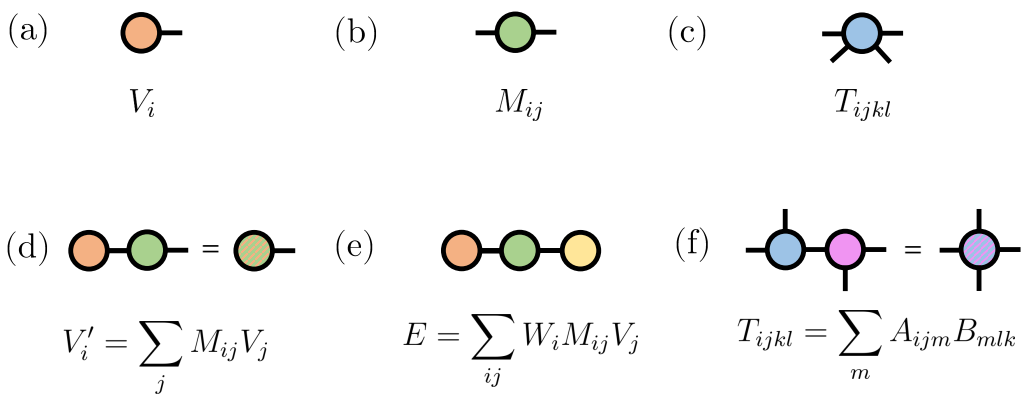

Figure 4.1: (a) A vector represented with a one-leg tensor. (b) A matrix represented with a two-leg tensor. (c) A tensor with four legs. (d) A vector-matrix multiplication. (e) A vector-matrix-vector multiplication, whose result is a scalar. (f) The one-index contraction of two rank 3 tensors, resulting in a rank 4 tensor.

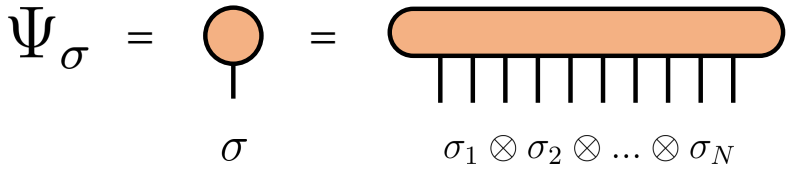

Figure 4.2: A N-qubit quantum state $|\Psi\rangle$ can be described by 2^N amplitudes $\{\Psi_\sigma\}$stored into a vector, represented by a one-legged tensor.

of quantum states, using their entanglement structure, while it should in principle require exponentially large vectors with respect to system size. Tensor networks have been particularly fruitful in computational quantum physics. At the forefront of tensor network algorithms, the density matrix renormalization group (DMRG) [137] algorithm combined with Matrix Product States (MPS) have been very popular to find efficiently ground states of interacting systems, performing particularly well for local gapped Hamiltonians where the short-range correlations are suited to the MPS structure.

At the heart of the power of tensor networks lies the representation of entanglement. It is precisely because of the difficulty of encoding entanglement that large correlated many-body systems are untractable. To illustrate this, let us consider N spins, each spin being described by a local Hilbert space $\mathcal{H}_{loc}$ of dimension $d = 2$. With this, a general many-body state $|\Psi\rangle$ living in $\mathcal{H} = \bigotimes_{i=1}^{N} \mathcal{H}_{loc}$ can be written as:

$$|\Psi\rangle = \sum_{\sigma=1}^{2^N} \Psi_\sigma |\sigma\rangle = \sum_{\sigma_1=0}^{1} \cdots \sum_{\sigma_N=0}^{1} \Psi_{\sigma_1 \ldots \sigma_N} |\sigma_1 \ldots \sigma_N\rangle . \tag{4.3}$$

Fig. 4.2 shows a naive pictorial tensor representation of a quantum state. However, quantum states with a small amount of entanglement should not require that many parameters. An intuitive example is the case of product states. Take an N-qubit generated only by single-qubit rotations. The resulting states can be written as a tensor product of single-qubit states as

$$|\psi\rangle = \otimes_{i=1}^{N} |\psi_i\rangle \,, \text{ with } |\psi_i\rangle = \alpha_i |0\rangle + \beta_i |1\rangle \,. \tag{4.4}$$

Although this product state lives in a 2^N-dimensional Hilbert space, only a set of $2N$ amplitudes $\{\alpha_i, \beta_i\}$ is necessary to fully describe the state, as the system described by $|\psi\rangle$ is effectively N individual qubit systems rather than one many-body system.

To quantify how "many-body" or how entangled is a state, the entanglement or Von Neumann entropy S_{vN} is a key metric. To calculate S_{vN}, we need to consider a bipartition of the state of the Hilbert space as $\mathcal{H} = \mathcal{H}_A \otimes \mathcal{H}_B$, where $\mathcal{H}_A$ ($\mathcal{H}_B$) denotes the Hilbert space of the subsystem A (B). The subsystem A (B) contains N_A (N_B) spins. We can then rewrite $|\Psi\rangle$ as a superposition of tensor product states from $\mathcal{H}_A$ and $\mathcal{H}_B$:

$$|\Psi\rangle = \sum_{k=1}^{2^{\min(N_A, N_B)}} \lambda_k \left|\Psi_k^A\right\rangle \left|\Psi_k^B\right\rangle , \tag{4.5}$$

where $|\Psi_k^{A(B)}\rangle \in \mathcal{H}_{A(B)}$. The form of $|\Psi\rangle$ is called a Schmidt decomposition, and can be numerically obtained thanks to a Singular Value Decomposition (SVD) of the state/vector $|\Psi\rangle$. A SVD decomposition of a matrix M of dimension $m \times n$ consists in decomposing M as $M = U\Sigma V^\dagger$, where U is a $m \times r$ matrix (with $r = \min(m, n)$), Σ is a $r \times r$ diagonal matrix, and $V^\dagger$ a $r \times n$ matrix. U and V obey the following orthogonality properties: $U^\dagger U = V^\dagger V = \mathbb{1}$. The link between Schmidt decomposition and SVD is central in any tensor network algorithms, both conceptually and numerically. Fig. 4.3 shows a tensor network representation of the Schmidt decomposition. In this form in Eq. 4.5, it becomes possible to quantify the amount of entanglement betwen the subsystem A and B by defining S_{vN} as

$$S_{\text{vN}} = -\text{Tr}_B[\rho_B \log_2(\rho_B)] \tag{4.6}$$

$$= -\text{Tr}_A[\rho_A \log_2(\rho_A)], \tag{4.7}$$

where ρ_L are the reduced density matrices defined as $\rho_{A(B)} = \text{Tr}_{B(A)}(\rho)$. Using the

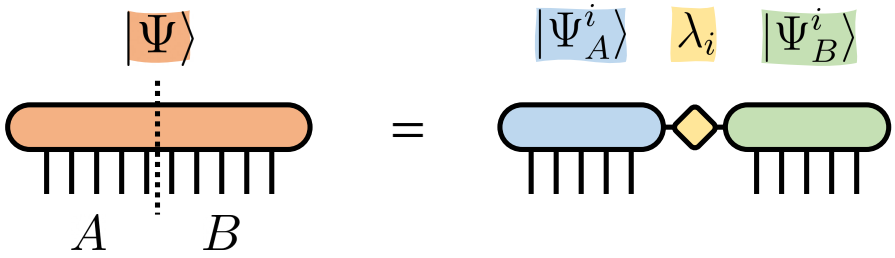

Figure 4.3: The schematic represention of a Schmidt decomposition of a state $|\Psi\rangle$ between two subsystems A and B.

Schmidt decomposition of $|\Psi\rangle$ as in Eq. 4.5, we directly obtain S_{vN} as

$$S_{\text{vN}} = -\sum_{k=1}^{2^{\min(N_A,N_B)}} \lambda_k^2 \log_2 \lambda_k^2. \tag{4.8}$$

We can identify two limit cases: when $\lambda_1 = 1$ and $\lambda_{k>1} = 0$, $|\Psi\rangle$ is a product state between A and B, and the two subsystems are disjoint and not entangled. As a consequence, $S_{\text{vN}} = 0$. On the other hand, if all the Schmidt values are equal, i.e. $\forall k$, $\lambda_k = 1/\sqrt{2^{\min(N_A,N_B)}}$ (as $\langle\Psi|\Psi\rangle = \sum_{k=1}^{2^{\min(N_A,N_B)}} \lambda_k^2 = 1$), $|\Psi\rangle$ is maximally entangled, S_{vN} reaches its maximum value $\min(N_A, N_B)$. In this case, we need an exponential number of parameters $\{\lambda_k\}$ to describe $|\Psi\rangle$.

In an intermediate case, only a fraction of the Schmidt values are non-zero. The number of non-zero Schmidt values is called the Schmidt rank, and, along with the entanglement entropy, reflects the degree of complexity of the state. With Eq. 4.5, we see that we can use a tensor network to represent a many-body state with a number of parameters that less than 2^N, as depicted in Fig. 4.3. These considerations are key to understand why tensor networks provide a resource-efficient approach to study quantum many-body problems.

4.2.2 The Matrix Product State ansatz

In this work, we employ numerical simulations based on MPS, which are a class of one-dimensional many-body quantum states that allow an efficient representation of entanglement. MPS are motivated by the concepts of Schmidt decomposition and entanglement as introduced in Sec. 4.2.1. We find the structure of MPS by extending the Schmidt decomposition between two subsystems. From a state $|\Psi\rangle$, we can perform a Schmidt decomposition between every qubit and the rest of the system, as pictured in Fig. 4.4. We then have a description of the tensor $\Psi_{\sigma_1 \ldots \sigma_N}$ as a one-dimensional network of local

tensors, describing the states of individual qubits, that form bonds between neighboring sites. This is from this structure that MPSs are defined.

To be more specific, we define the MPSs as the class of states where the amplitudes are obtained by contracting matrices $\{\Gamma^{[n]\sigma_n}\}$ together with Schmidt values $\{\lambda^{[n]}\}$ as depicted in Fig. 4.5a, such that

$$|\Psi_{\text{MPS}}\rangle = \sum_{\{\sigma_n\}} \sum_{\{\alpha_n\}} \Gamma^{[1]\sigma_1}_{\alpha_1} \lambda^{[1]}_{\alpha_1} \Gamma^{[2]\sigma_2}_{\alpha_1\alpha_2} \lambda^{[2]}_{\alpha_2} ... \Gamma^{[N]\sigma_N}_{\alpha_N} |\sigma_1\sigma_2...\sigma_N\rangle \,, \tag{4.9}$$

where $\Gamma^{[n]\sigma_n}$ for $2 \leq n \leq N-1$ are complex matrices of dimension $\chi_{n-1} \times \chi_n$, where χ_n is called the bond dimension between spin sites n and $n+1$. At the boundaries, the tensors $\Gamma^{[1]\sigma_1}$ and $\Gamma^{[N]\sigma_N}$ are vectors of dimension χ_1 and χ_{N-1}. The bond dimension of a MPS dictates the storage cost of the state, scaling as $\mathcal{O}(N\chi^2)$, and is a key element to understand how entangled the MPS can be. Indeed, we calculate the entanglement entropy at the bond between sites $(n, n+1)$ as $S_{\text{vN}} = -\sum_{k=1}^{\chi_n} (\lambda_k^{[n]})^2 \log_2 (\lambda_k^{[n]})^2$. Therefore the maximal amount of entanglement entropy between the subsystems on the right and left of the bond is equal to $\log_2 \chi_n$. This highlights that the amount of entanglement in a MPS is directly related to the dimensions of its tensors and therefore to its storage cost. By increasing the bond dimension of a MPS, as sketched in 4.5b, we can span a larger part of the many-body Hilbert space, which makes the MPS more expressive.

4.2.3 Contraction, expectation value and canonical forms

We have seen that MPSs allow us to encode many-body quantum states at a controlled cost. In order to perform computations such as calculating overlaps between MPSs or expectation values, we can take advantage of the MPS structure to contract efficiently

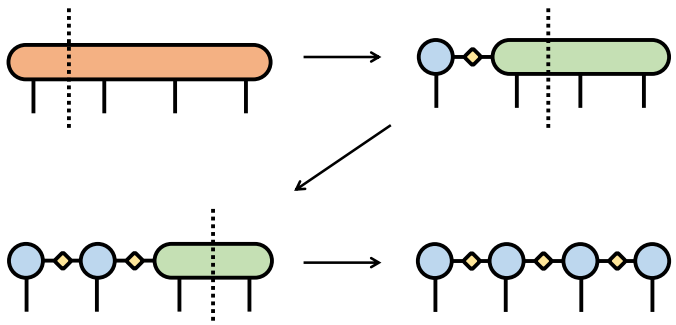

Figure 4.4: A general state can be turned into a MPS thanks to a series of SVD at each bond.

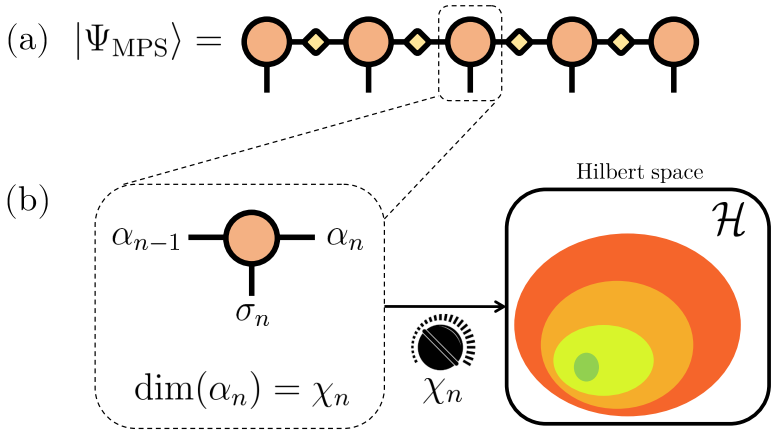

Figure 4.5: (a) The schematic of the MPS structure, based on Schmidt decomposition's principle. (b) A MPS is built from local tensors. A key parameter is the bond dimension χ that corresponds to dimension of the indices forming the bonds between local tensors. By increasing χ, the MPS can span a larger part of the many-body Hilbert space and therefore is more expressive.

the indices. Indeed, a crucial point in tensor network calculations is finding efficient contraction schemes, as the order of index contraction can have a drastic impact on the tractability of a computation. Figs 4.6a&b shows an example where the same computation is performed at two different costs depending on the chosen contraction scheme. Fig. 4.6c highlights this with the example of calculating the overlap between two MPSs $|\Psi_1\rangle$ and $|\Psi_2\rangle$ of bond dimension χ and local state dimension d, with N sites. This computation involves contracting N indices of dimension d and $2(N-1)$ indices of dimension χ. A brute force contraction leads to a cost $\mathcal{O}((d\chi^2)^N)$, which scales exponentially with the system size. However, it is possible to make this computation tractable by "zipping" two MPSs from one end to the other, site by site. At each step, the contraction from one site to the next comes at a cost of $\mathcal{O}(d\chi^3)$, leading to an overall cost scaling $\mathcal{O}(Nd\chi^3)$, making the computation tractable. Similarly, one can compute the expectation value of an observable by inserting the tensor representation of the observable between the tensor network representing $\langle\Psi|$ and $|\Psi\rangle$ and use the same contraction strategy. Fig. 4.6d shows an example of such computation with a one-qubit observable.

Further optimization can be achieved by taking advantage that the tensors composing a MPS are defined up to a choice of gauge. Indeed, as shown in Fig. 4.6e1., two neighboring tensors can be redefined by inserting a matrix X and its inverse X^{-1} at the bond. This degree of freedom allows one to choose tensors with isometries conditions. In particular, we can set the following properties for the tensors composing the MPS:

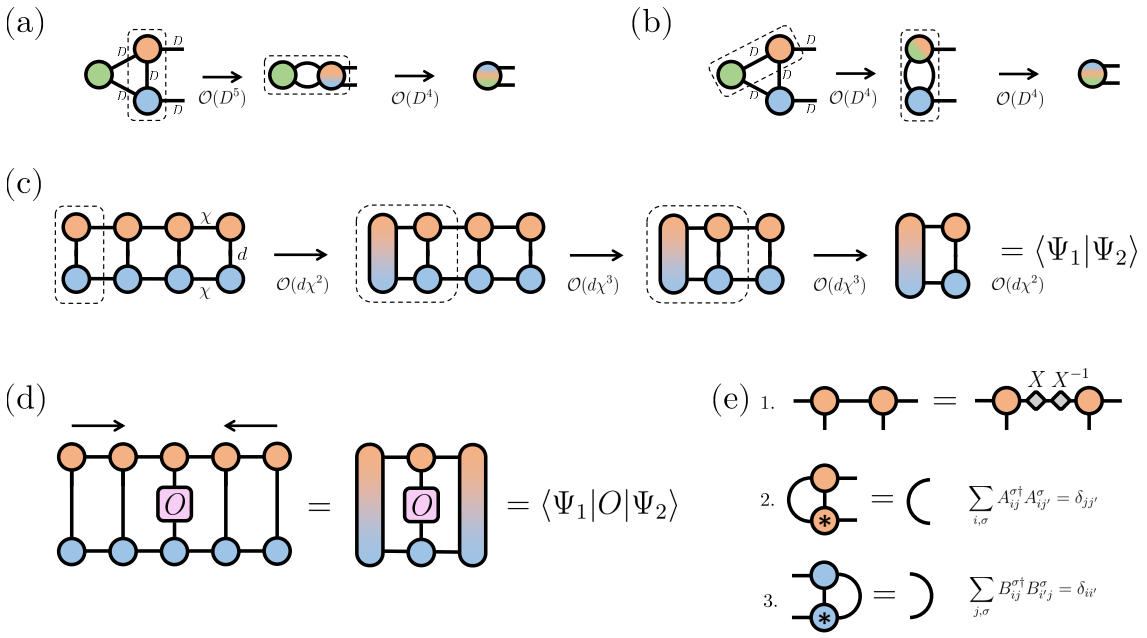

Figure 4.6: (a) The contraction of three tensors where each index has a dimension D. By contracting the blue and orange tensors first, as depicted with the dashed box, the overall cost is $\mathcal{O}(D^5)$. (b) By contraction the green and blue tensors first, the same compution is now made at a cost $\mathcal{O}(D^4)$.

1. A tensor A^{σ}_{ij} is said to be in a left-canonical form if $\sum_{i,\sigma} A^{\sigma *}_{ij} A^{\sigma}_{ij'} = \delta_{jj'}$.
2. A tensor B^{σ}_{ij} is said to be in a right-canonical form if $\sum_{j,\sigma} B^{\sigma *}_{ij} B^{\sigma}_{i'j} = \delta_{ii'}$.

Such properties can be obtained thanks to the properties of the SVD decomposition. Indeed, performing an SVD decomposition on two neighboring tensors $(i, i+1)$ leaves the tensor at site i in a left-canonical form, while the tensor at site $i+1$ is in a right-canonical form. For example, performing SVDs from left to right along the whole MPS puts the state in a left-canonical form. Having such properties is particularly advantageous when evaluating an observable. Indeed, taking the example of Fig. 4.6d where we evaluate a one-qubit observable at site i, putting the tensors left/right to i in a left/right-canonical form allows to simplify the contraction by simply using identities on the left and right of site i.

4.2.4 Time evolution with MPS

In this chapter, we aim at benchmarking the capabilities of quantum computers compared to standard MPS techniques for time evolution [27]. Here we make a brief introduction to time-dependent simulations with MPS. Let us consider a one-dimensional system

formed by L spin-1/2's, put into an initial state $|\Psi_0\rangle$ that is suddenly driven under a Hamiltonian H at $t > 0$. The time-evolved state reads as

$$|\Psi(t)\rangle = e^{-iHt} |\Psi_0\rangle . \tag{4.10}$$

To simulate time evolution with MPS, we use the so-called TEBD algorithm or Trotter-Suzuki decomposition method [76]. For simplicity, we consider an Hamiltonian $H = \sum_{i=1}^{L-1} h_{i,i+1}$ as a sum of local Hamiltonians. In general, e^{-iHt} can be represented by a (untractable) unitary matrix of exponentially large with respect to system size. Therefore, we approximate the time propagator $U(t) = e^{-iHt}$ by performing time steps of duration dt thanks to the standard first-order Trotter-Suzuki's formula as

$$U(t) \simeq \prod_{n=1}^{t/dt} U_1(dt) = \prod_{n=1}^{t/dt} \prod_{i \text{ even}} e^{-ih_{i,i+1}dt} \prod_{j \text{ odd}} e^{-ih_{j,j+1}dt}. \tag{4.11}$$

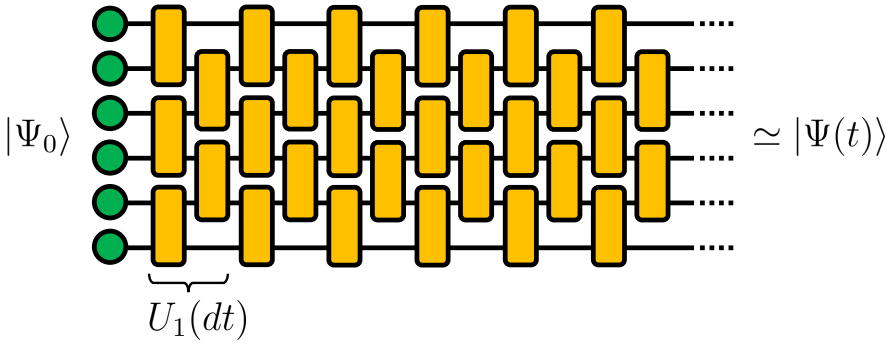

Figure 4.7: A quantum circuit representation of the TEBD algorithm. Starting from an initial product state $|\Psi_0\rangle$, represented with the green local tensors, the time-evolution operator is approximated by a 1st-order Trotter operator U_1. We successively apply quantum gates (the yellow four-legged tensors) on pairs of neighboring sites.

The error coming from approximating e^{-iHt} with the first-order Trotter-Suzuki from Eq. 4.11 scales as $\mathcal{O}(tdt)$. As shown in Fig. 4.7, the simulation consists of applying a quantum circuit to the MPS. At each time step, we apply local unitary transformations $e^{-ih_{i,i+1}dt}$ between two neighboring sites, which leads to an update of the corresponding tensors. The difficulty for MPS techniques to simulate quantum dynamics (or quantum circuits) arises from the resulting growth of the bond dimension as we will explain now. As shown in Fig.4.8a, the procedure goes as:

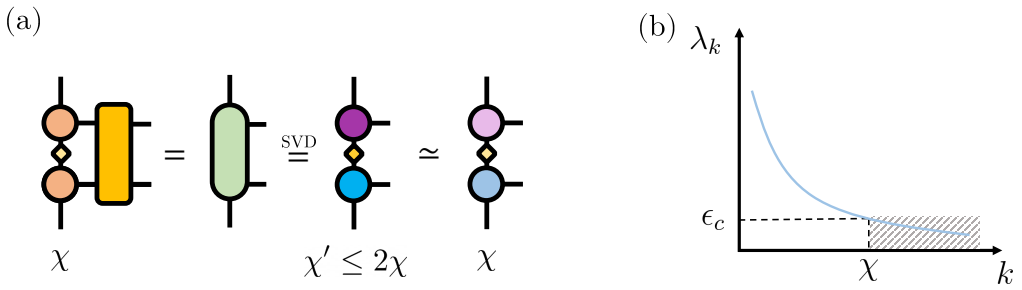

Figure 4.8: (a) Procedure to apply a local 2-qubit gate to a MPS. The contraction between the two tensors of adjacent sites with the gate is followed by a SVD. This leads in general to an increase of the bond dimension. (b) By looking at the new singular values, we can choose to truncate the MPS by only taking the χ-highest singular values or superior to a threshold ϵ_c.

1. We first contract the local tensors at site i and $i+1$:

$$\Theta^{\sigma_i\sigma_{i+1}}_{\alpha_{i-1}\alpha_{i+1}} = \sum_{\alpha_i} \Gamma^{[i]\sigma_i}_{\alpha_{i-1}\alpha_i} \lambda^{[i]}_{\alpha_i} \Gamma^{[i+1]\sigma_{i+1}}_{\alpha_i\alpha_{i+1}}. \tag{4.12}$$

2. We apply the local unitary u:

$$\tilde{\Theta}^{\sigma_i\sigma_{i+1}}_{\alpha_{i-1}\alpha_{i+1}} \sum_{s_i,s_{i+1}} \Theta^{s_i s_{i+1}}_{\alpha_{i-1}\alpha_{i+1}} u^{\sigma_i\sigma_{i+1}}_{s_i s_{i+1}}. \tag{4.13}$$

3. To retrieve the MPS structure, we need to split $\tilde{\Theta}$. To do so, we perform a SVD of the tensor: we put together the indices (σ_i, α_{i-1}) and $(\sigma_{i+1}, \alpha_{i+1})$ to form a matrix of size $2\chi_{i-1} \times 2\chi_{i+1}$. Then, the SVD allow us to rewrite Θ as $\Theta = XSY^\dagger$, where $X^\dagger X = Y^\dagger Y = \mathbb{1}$ and S is a diagonal matrix containing the singular values of Θ. We can identify now

$$\Gamma^{[i]} \leftarrow X,\ \lambda^{[i]} \leftarrow S \text{ and } \Gamma^{[i+1]} \leftarrow Y^\dagger. \tag{4.14}$$

4. However, we see now that applying a two-qubit gate has increased the bond dimension $\chi_i \leftarrow \chi'_i = 2\min(\chi_{i-1}, \chi_{i+1})$. This implies a exponential growth of the bond dimension with the simulation time, or equivalently, the circuit depth. A key step is to take advantage of the SVD used in step 3. As shown with Fig. 4.8b, we can decide to only keep the χ largest singular values and/or the singular values that are higher than a threshold ϵ_c, and keep the corresponding columns/rows of $\Gamma^{[i]}/\Gamma^{[i+1]}$.

To maintain the normalization of the state, we renormalize the singular values as:

$$\lambda_k^{[i]} \leftarrow \frac{\lambda_k^{[i]}}{\sqrt{\sum_{k=1}^{\chi_i'} \lambda_k^{[i]2}}}. \tag{4.15}$$

The fidelity F_{trunc} of the truncated state can be evaluated as

$$F_{\text{trunc}} = \frac{\sum_{k=1}^{\chi} \lambda_k^{[i]2}}{\sum_{k=1}^{\chi_i'} \lambda_k^{[i]2}}. \tag{4.16}$$

From this procedure, we understand that performing time evolution with MPSs can drastically increase their bond dimensions as the states will get more entangled. Bounding the bond dimension to a maximal value χ requires the truncation of the state, resulting in an approximate solution. By doing so, we keep control on the cost of the algorithm but we also limit the entanglement entropy carried by the MPS, and therefore its ability to efficiently simulate the dynamics of a quantum system.

4.2.5 Out-of-equilibrium dynamics: a challenge for MPS and Quantum Computers

We have seen that performing time evolution can be a challenge for MPSs, as the set maximum bond dimension limits the capacity to encode entangled states. A paradigmatic example where MPSs fail is the case of out-of-equilibrium dynamics, typically observed after a quantum quench. The quantum quench corresponds to a situation where a quantum system is prepared in an initial state $|\Psi_0\rangle$, that is the ground state of the Hamiltonian H_0 describing the system. However, At $t = 0$, the system's Hamiltonian is brutally changed to $H \neq H_0$. At this moment, the system described by $|\Psi_0\rangle$ is no longer at equilibrium and contains excited states of H. The dynamics of the system can be described with the propagation of excitations that spread into the system and create entanglement between two subparts of the system. As a result, the entanglement entropy grows ballistically with time [140, 141]. Fig. 4.9 summarizes the principle of quantum quenches.

The linear increase of the entanglement entropy is the reason for the intractability of such simulations. Indeed, the maximum entanglement entropy S_{vN} of a MPS with bond dimension χ is $\log_2 \chi$, or equivalently, to represent a state whose entanglement entropy is S_{vN}, we need to use an MPS with a minimal bond dimension $2^{S_{\text{vN}}}$. If we have $S_{\text{vN}}(t) \simeq \gamma t$, we conclude that the required bond dimension scales exponentially with the simulation time, limiting MPS techniques to short-time dynamics only.

To illustrate this, we consider here the paradigmatic one-dimensional spin-1/2 Ising

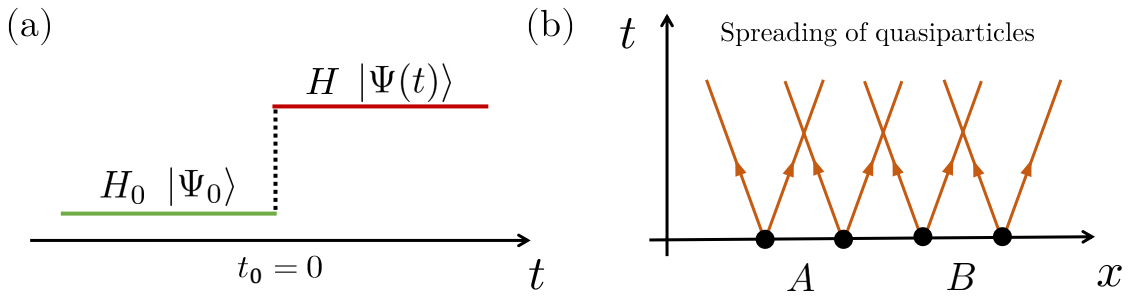

Figure 4.9: (a) A system described by the Hamiltonian H is described by its ground state $|\Psi_0\rangle$. At $t_0 = 0$, the Hamiltonian of the system is suddenly changed to H. The system is then described by $|\Psi(t)\rangle = e^{iHt}|\Psi_0\rangle$. (b) As $|\Psi_0\rangle$ is not the ground state of H, the system is put out-of-equilibrium with excitations spreading through the system as quasiparticles, creating entanglement between distant regions A and B of the system.

model with a transverse field. The corresponding Hamiltonian is defined as

$$H = -J\sum_{i=1}^{L-1} X_i X_{i+1} - h\sum_{i=1}^{L} Z_i, \tag{4.17}$$

where L is the number of spin sites on the chain, J is the interaction strength between neighboring spins and h is the transverse field value. The spin operators X_i and Z_i are equals to $\begin{pmatrix} 0 & 1 \\ 1 & 0 \end{pmatrix}$ and $\begin{pmatrix} 1 & 0 \\ 0 & -1 \end{pmatrix}$ respectively.

$$h_{i,i+1} = -JX_iX_{i+1} - \frac{h}{2}(Z_i + Z_{i+1})\ \forall i \in [2, L-2], \tag{4.18}$$

$$h_{1,2} = -JX_1X_2 - h(Z_1 + \frac{1}{2}Z_2), \tag{4.19}$$

$$h_{L-1,L} = -JX_{L-1}X_L - h(\frac{1}{2}Z_{L-1} + Z_L). \tag{4.20}$$

$$\tag{4.21}$$

The initial state is chosen to be a Néel state defined as $|\uparrow\downarrow\uparrow\downarrow ...\rangle$. Fig. 4.10 shows the entanglement entropy at the middle of the chain $S_{\text{vN}}^{L/2}$ as a function of time for MPS with different bond dimensions for the critical point $J/h = 1$. This model and parameter choice will be kept throughout the rest of this work. We observe that for a given bond dimension, the resulting entanglement entropy saturates at $\log_2 \chi$, showing that the simulation is only an approximation beyond the corresponding simulation time. Increasing the maximum bond dimension allows us to push this barrier for longer simulation times.

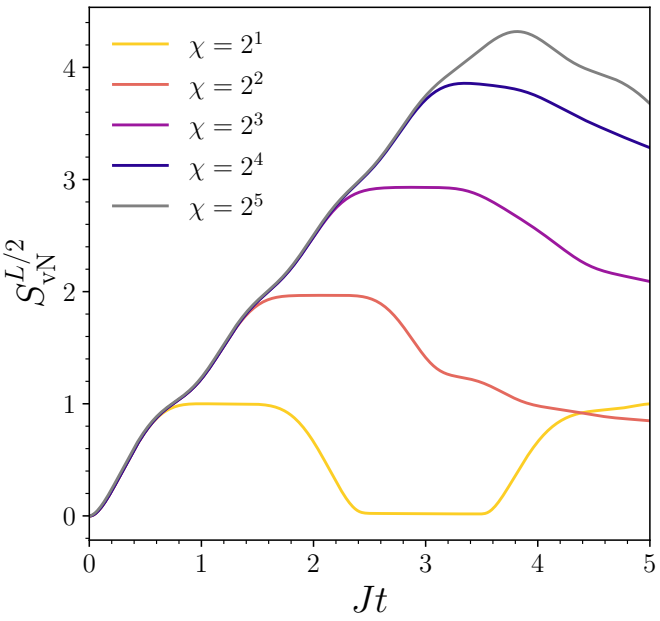

Figure 4.10: The von Neumann entropy S_{vN} as a function of time from MPS states with different bond dimensions χ for $L = 10$ spin sites under a global quench. S_{vN} grows ballistically with time and saturates at $\log_2 \chi$. For 10 sites, the MPS of bond dimension 2^5 is not truncated and therefore is exact.

Out-of-equilibrium dynamics constitute a good benchmark problem for quantum computers with a condensed matter perspective. On the one hand, state-of-the-art tensor network techniques are fundamentally limited by their capacity to represent entanglement. On the other hand, quantum computers hold the promise to circumvent this problem by directly manipulating entangled qubit states, but noise occurring in current quantum devices also strongly limits their performances. Being able to simulate quantum dynamics with quantum computers beyond simulation times out-of-reach of classical methods is an interesting and relevant challenge. In the next sections, we explain that we can benefit from using MPSs in their tractable regime to enhance quantum simulations.

4.3 Optimizing Quantum Circuits with Matrix Product States

In Section 4.2, we detailed the MPS formalism, and how it can be used to simulate the dynamics of quantum systems, but most importantly its bottleneck, lying in their ability to represent states with a high degree of entanglement. On the other hand, quantum computers do not suffer from this in principle as they naturally use entanglement but are limited by noise. Representing MPSs with efficient quantum circuits is an appealing

challenge as it offers a promising pathway to extend classical methods beyond their limitations, such as performing time evolution as investigated here, while optimizing the use of quantum resources.

The preparation of MPS states with qubits was first presented in [143]. Later, techniques were developed to generate quantum circuits approximating a given MPS [144, 145, 146], or alternatively optimize quantum circuits using a MPS representation [147]. Among potential applications, it has been proposed to initialize parametrized quantum circuits with classically optimized tensor network states [148, 149, 150]. Tensor networks have also inspired classes of variational quantum circuits [151, 152, 153, 154, 136, 155] and have been experimentally realized on quantum devices [156, 157, 158, 159]. Embedding tensor networks into quantum algorithms has also been explored in the context of DMFT calculations [160].

In this section, we use the algorithm defined in [147]. The goal here is to classically optimize a quantum circuit $|\Psi_{\mathrm{QC}}\rangle$ with a MPS so that $|\Psi_{\mathrm{QC}}\rangle$ approximate the time-evolved state $|\Psi(t)\rangle = e^{-iHt}|\Psi_0\rangle$. The depth of the quantum circuit is chosen accordingly with the maximum bond dimension so that the MPS can represent exactly the resulting state. To represent the time-evolved states as quantum circuits, we use a circuit ansatz defined as:

$$|\Psi_{\mathrm{QC}}(t)\rangle = \prod_k U_k(t)\,|\Psi_0\rangle\,, \tag{4.22}$$

where $U_k(t)$ are unitary gates that compose the circuit acting on the initial state $|\Psi_0\rangle$. To approximate the state at time $t+dt$, we first evolve $|\Psi_{\mathrm{QC}}(t)\rangle$ by applying the (trotterized) time-evolution operator $U(dt) \simeq e^{-iHdt}$ (see Eq. 4.11). To obtain $|\Psi_{\mathrm{QC}}(t+dt)\rangle = \prod_k U_k(t+dt)\,|\Psi_0\rangle$, we classically optimize the unitaries $U_k(t+dt)$ to maximize the overlap with $U(dt)\,|\Psi_{\mathrm{QC}}(t)\rangle$. To do so, we iteratively optimize each unitary U_k to maximize the overlap F_k between the target state $|\Phi\rangle$ and $|\Psi\rangle = \prod_k U_k\,|\Psi_0\rangle$ as

$$F_k = \langle\Phi|(\prod_{i>k} U_i)U_k \prod_{j<k} U_j\,|\Psi_0\rangle \tag{4.23}$$

$$= \langle\Phi_{k+1}|U_k\,|\Psi_{k-1}\rangle \tag{4.24}$$

$$= \mathrm{Tr}(E_k U_k), \tag{4.25}$$

where the environment tensor E_k is defined as

$$E_k = \mathrm{Tr}_{\overline{k}}(|\Psi_{k-1}\rangle\,\langle\Phi_{k+1}|). \tag{4.26}$$

Here $\mathrm{Tr}_{\overline{k}}(.)$ operates the trace over all qubits but the qubits acted on by the unitary U_k. Graphically, E_k is calculated by contracting all qubit indices except the ones involved in

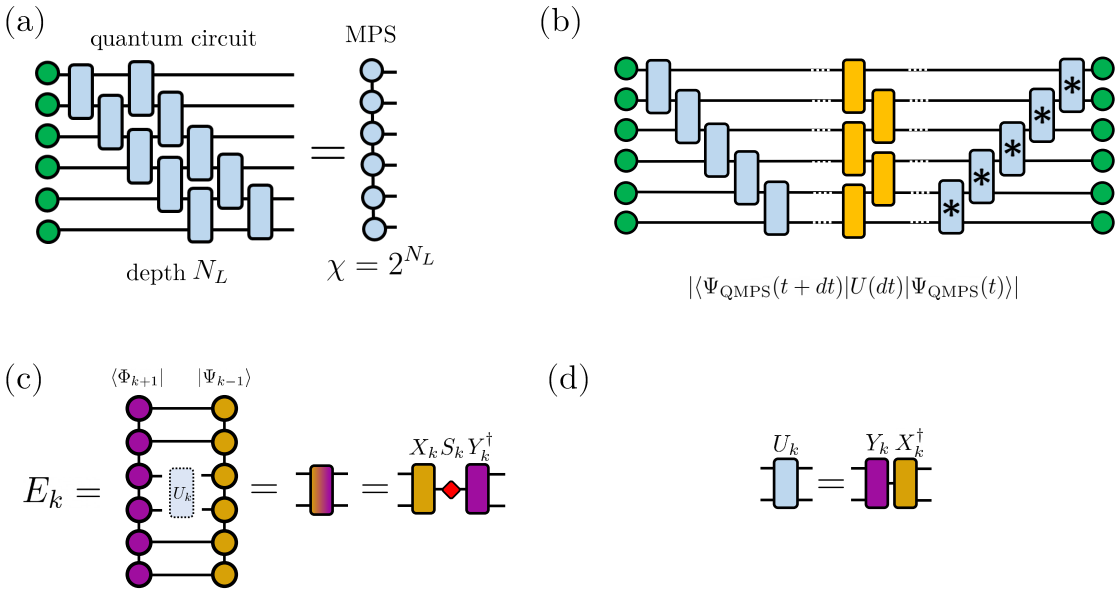

Figure 4.11: (a) A state prepared by a short-depth circuit can be efficiently represented by a MPS. More specifically, in the case of the sequential circuit with N_L layers, a MPS of bond dimension 2^{N_L} describes exactly the resulting state. (b) To perform time-evolution with MPSs while keeping a quantum circuit representation, we optimize the gate to maximize the overlap between $|\Psi_{\mathrm{QC}}(t+dt)\rangle$ and $U(dt)\,|\Psi_{\mathrm{QC}}(t)\rangle$. (c) In the optimization process, we obtain the environment tensor E_k by contracting the desired MPS and the QMPS to optimize having removed the gate U_k. (d) The unitary U_k is updated from the SVD of E_k.

the unitary operation U_k. By forming a SVD of E_k, we rewrite E_k as

$$E_k = X_k S_k Y_k^\dagger. \tag{4.27}$$

From Eq. 4.27 he unitary U_k is then updated according to [161] by

$$U_k \leftarrow Y_k X_k^\dagger. \tag{4.28}$$

This optimization step is performed for each unitary U_k consecutively. The procedure is sketched in Fig. 4.11. The whole process is repeated until either a convergence criterion is reached or a maximum number of sweeps is reached. Here the convergence is reached when performing a sweep does not improve the fidelity up to a specific threshold.

The resulting circuits will be mentioned as Quantum Matrix Product States (QMPS) throughout this manuscript. In Fig. 4.12, we show the performance obtained from the

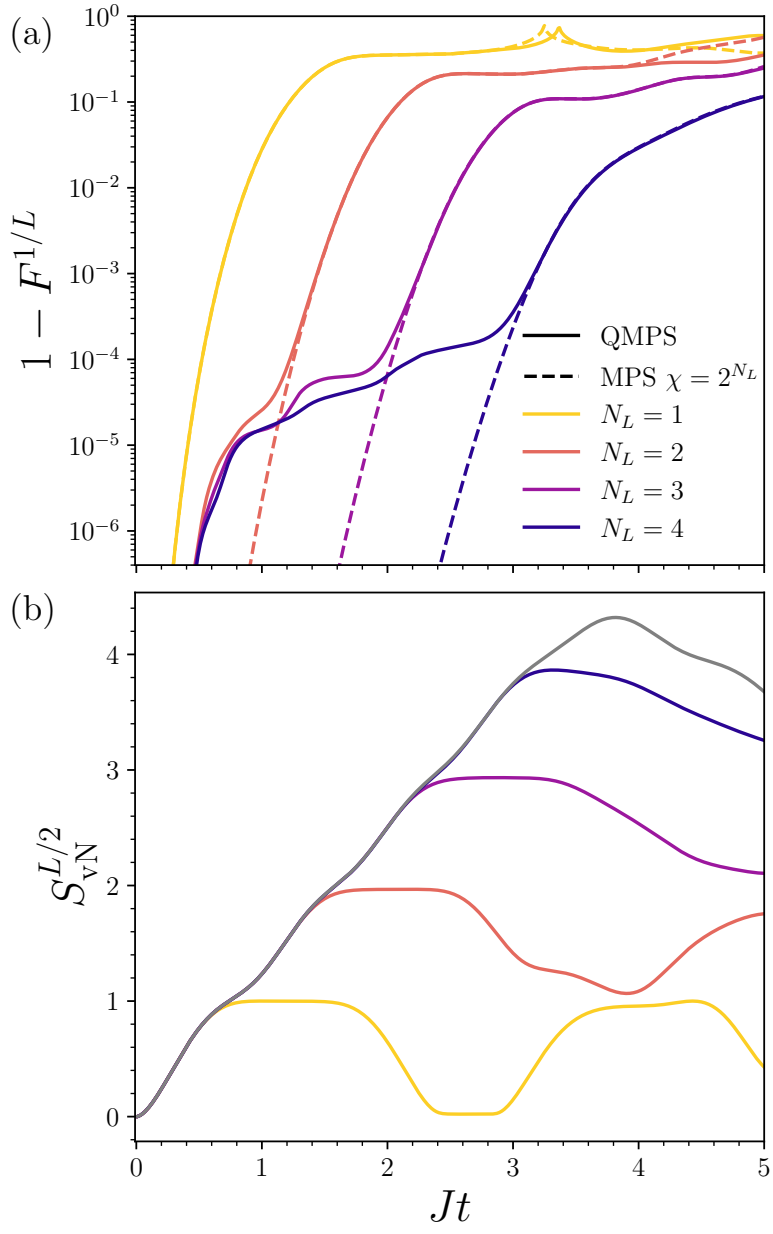

Figure 4.12: The infidelity per site (a) and the entanglement entropy (b) as a function of time for classically optimized quantum circuits of different number of layers N_L and for MPS for corresponding bond dimension $\chi = 2^{N_L}$.

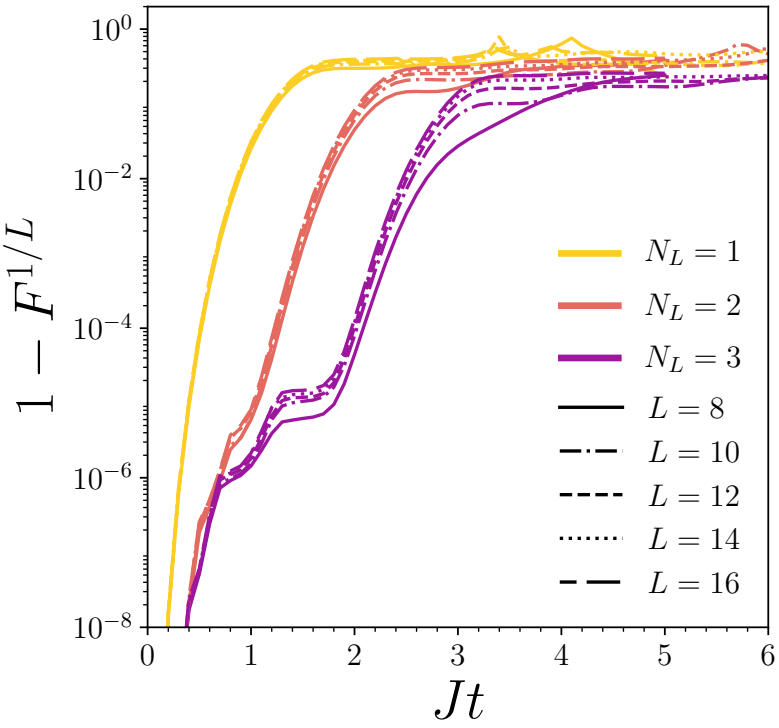

Figure 4.13: Infidelity per site versus time for the classically optimized quantum circuits for $L = 8, 10, 12, 14$ and 16, optimized with $dt = 0.1$.

optimized QMPS $|\Psi_{\mathrm{QC}}(t)\rangle$. We use the same ansatz $|\Psi_{\mathrm{QC}}(t)\rangle$ used in [147], which consists of staircase layers of two-qubit gates. We take exact time-evolved MPSs with a time step $\delta t = 0.01$ (in $1/J$ units, as it will be implicitly assumed throughout the rest of the chapter) as a reference solution $|\Psi_{\mathrm{ref}}(t)\rangle$. In Fig. 4.12a, we evaluate the quality of the QMPS states of different layers with the infidelity per site calculated as $1 - F^{1/L}$, where $F = |\langle\Psi_{\mathrm{ref}}(t)|\Psi_{\mathrm{QC}}(t)\rangle|^2$. As a QMPS of depth N_L can be represented by a MPS of bond dimension $\chi = 2^{N_L}$, we also compare QMPS with MPS solutions of corresponding χ. We observe that while MPS solutions are quasi-exact in short-time regimes, QMPS have slightly larger infidelities. This can be attributed to the optimization hyperparameters (number of sweeps and convergence threshold, here set to 2000 and 10^{-10}), the cumulated error at each time step as well as the choice of the ansatz. However, the fidelities remain satisfyingly high. With Fig. 4.12b, we observe the same behavior as in Fig 4.10 in terms of entanglement entropy. Most importantly, both techniques fail at the same simulation time, when the entanglement entropy reaches its maximum with respect to N_L and χ. In this example, QMPS states demonstrate similar strengths (and weaknesses) to MPSs while being implementable on a quantum computer.

With Fig. 4.13, we also address the performances of this method for different numbers of layers and different system sizes. We observe that the infidelity per site $1 - F^{1/L}$ is a relevant metric to consider here as it exhibits a behavior independent of the system size. This can be explained as the errors with MPSs come from the truncation of the bond dimension when applying local two-qubit gates. As this operation is local (acting on only two qubits at the time), we can expect the truncation error to be independent of the system size. When the system gets larger, the error per gate remains similar, but more gates are applied (each time step requiring $\mathcal{O}(L)$ gates). The global error is approximated by the product of two-qubit gate truncation errors, leading to the observed behavior.

4.4 Combining MPS and Quantum Computers: Noisy Simulations

In Section 4.3, we displayed the capacity of QMPS to efficiently represent tensor network states as quantum circuits. This opens the possibility to extend classical simulations toward regimes where high levels of entanglement are required. By implementing QMPSs on quantum computers, it becomes possible to manipulate these states and generate more entanglement. With the example of quantum dynamics, this offers the possibility to carry a simulation further in time by breaking the classical entanglement barrier. In this Section, we attempt to combine time-evolved MPS brought to their entanglement saturation time and quantum computers. We use the best of worlds: the short-time dynamics is efficiently performed by tensor network techniques while running Trotter circuits on a noisy quantum device would be ineffective. Instead, we use optimized short-depth quantum circuits to encode the classical solutions and only perform Trotter steps to reach longer simulation time thanks to the quantum computer. This hybrid classical-quantum procedure is summarized in Fig. 4.14. Our analysis covers the fidelity in Sec. 4.4.1 as well as the amount of entanglement carried by the noisy states in Sec. 4.4.2.

To model noisy quantum computers, we perform exact density matrix calculations including a depolarizing channel. After each two-qubit gate, the density matrix undergoes the following transformation:

$$\rho \to (1-\epsilon)\rho + \frac{\epsilon}{15}\sum_{K\in\mathcal{K}} K_k \rho K_k^\dagger, \tag{4.29}$$

where $\mathcal{K} = \{I, X, Y, Z\}^{\otimes 2}\backslash\{I \otimes I\}$ and ϵ is the error rate. This transformation models the gate errors with an incoherent stochastic noise. Although it does not capture all noise phenomena happening in a real quantum device, it describes one of the most prominent

error sources of NISQ devices. Moreover, coherent noise can be converted into depolarizing noise with techniques like randomized compiling [162]. Therefore simulating noisy quantum computers under such a model gives interesting and physically relevant insights into their performances.

4.4.1 Fidelity

To evaluate the quality of the states $|\Psi(t)\rangle$ or $\rho(t)$ obtained from the MPS techniques and noisy quantum computers, we calculate their overlap with a reference solution $|\Psi_{\text{ref}}(t)\rangle$. As in Sec. 4.3, we choose this reference solution to be an exact solution time-evolved with a time step $dt = 0.01$. For a noisy state $\rho(t)$, the fidelity is calculated as $F = \langle\Psi_{\text{ref}}(t)|\rho(t)|\Psi_{\text{ref}}(t)\rangle$.

We perform noisy simulations of the quantum circuits for Trotterized time evolution with and without QMPS and compare their fidelities. As density matrix calculations are computationally more costly than state vectors or MPS simulations, we focus on $L = 10$ spins with a QMPS of depth $N_L = 3$ (and a MPS of bond dimension $\chi = 2^3$ accordingly). However, in order to compare systems of different sizes, we again use the infidelity per site defined as $1 - F^{1/L}$. Fig. 4.15a shows the infidelity per site as a function of time with a two-qubit error rate equal to $10^{-2}, 10^{-3}$ and 10^{-4} and a time step dt set to 0.01.

First, we observe that a MPS provides much better results for short-time dynamics. Second, using a QMPS as a starting point leads to better fidelities compared to pure Trotter quantum circuits, especially for short-time simulation. This is naturally expected as they use limited quantum resources while capturing efficiently the time evolution in this regime. Therefore, the main advantage of QMPS with noisy quantum computers exists for a longer simulation time.

It is worth pointing out that in those results, the time step dt has been set to 0.01, which leads to large circuit depth but reduces significantly the Trotter errors. In Fig. 4.15b, the Trotter steps are performed on the noisy quantum computer with a time step $dt = 0.1$. It shows that for realistic noise levels between 10^{-2} and 10^{-3}, the main source of error remains the noise while infidelities for smaller error rates are bounded by the Trotter errors.

Under a depolarizing noise, the fidelity of a noisy state can be well approximated by $(1-\epsilon)^{L\times D}$ with L the system size and D the depth of the circuit. Consequently, the fidelity of the Trotterized states is estimated as

$$F_{\text{Trot.}} \sim (1-\epsilon)^{Lt/dt}, \tag{4.30}$$

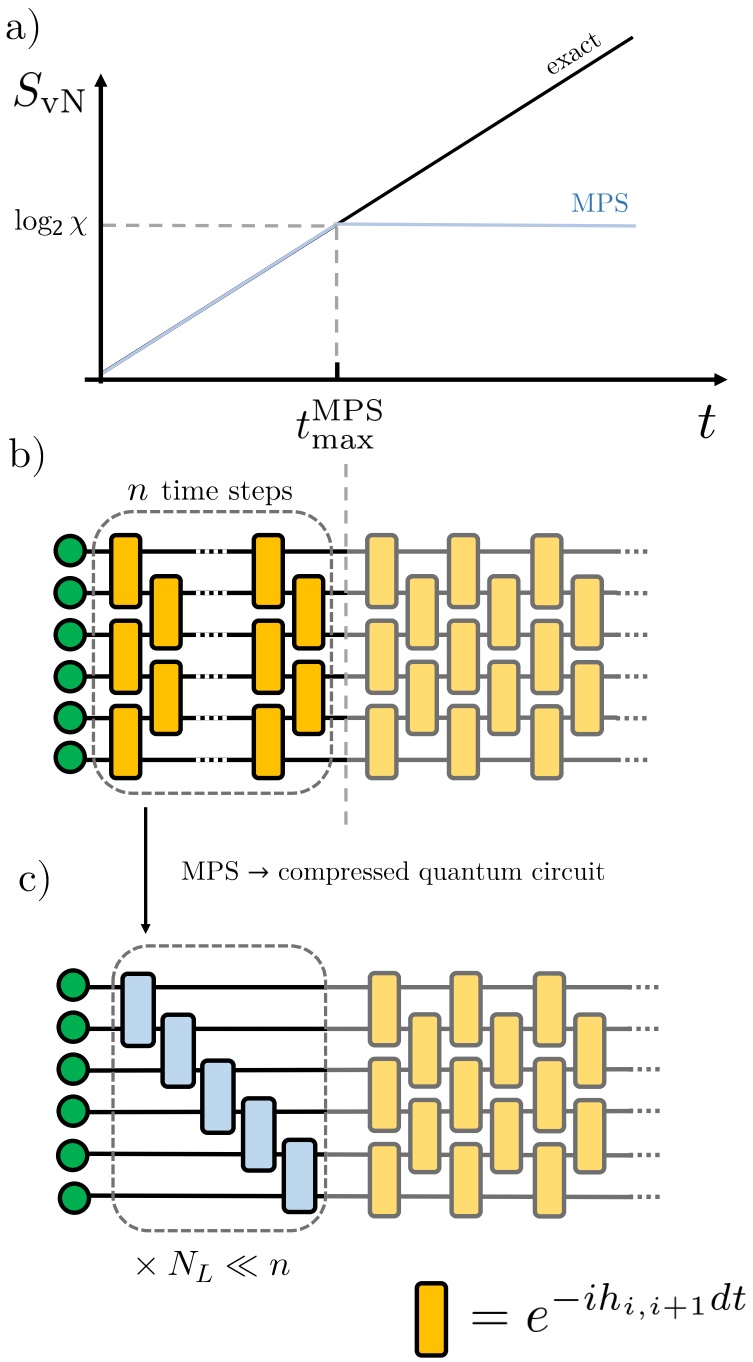

Figure 4.14: (a) Classical MPS of dimension χ can only access short-time dynamics. The maximum simulated time $t_{\mathrm{max}}^{\mathrm{MPS}}$ is defined as the time when MPS's entanglement entropy reaches $\log_2 \chi$. (b) The quantum circuit corresponds to the TEBD algorithm. The time-evolved state at time $t \leq t_{\mathrm{max}}^{\mathrm{MPS}}$ can be classically represented by a MPS and can be efficiently represented by a circuit (c) of depth N_L. In the case of sequential circuits as displayed here, the depth $N_L \sim \log_2 \chi$. The time evolution can be carried further on the quantum computer.

while for the QMPS it can be written as $(1-\epsilon)^{LN_L} \times f_{\text{QMPS}}$, where f_{QMPS} is the fidelity of the classically optimized QMPS. For $t \lesssim t_{\text{max}}^{\text{MPS}}$, as shown in Fig. 4.12a, f_{QMPS} can be crudely taken as $f_{\text{QMPS}} \sim 1$. Therefore, we can approximate the fidelity of the extended QMPS by

$$F_{\text{QMPS + Trot.}} \sim (1-\epsilon)^{L(N_L+(t-t_{\text{max}}^{\text{MPS}})/dt)}. \tag{4.31}$$

Fig. 4.16 shows diagrams of the advantage of noisy Trotter evolution with and without QMPS over MPS solutions with different maximum bond dimensions with respect to the simulation time and the noise level. It leads to the two following conclusions: First, for simulation time longer than $t_{\text{max}}^{\text{MPS}}$, a noisy time evolution can have a larger fidelity only if the noise level is sufficiently low. With the example of $L = 10$ spin sites and $dt = 0.01$, the error rate ϵ needs to be lower than 10^{-3} to reach an advantage. Second, using a QMPS as a starting point makes it possible to beat the MPS with a larger error rate than a simple Trotterized quantum circuit and therefore bridge between the classical and quantum advantage domains.

We emphasize again that the noise map used here only takes into account gate errors. Despite being predominant in current devices, it does not capture all the relevant sources of error. For example, phase and amplitude damping or cross-talk noise also are relevant noises occurring in quantum devices and play a major role in their performances. Reducing the circuit depth becomes even more crucial, and therefore using classical knowledge in the form of QMPS provides a way to better use limited quantum resources.

4.4.2 Entanglement Entropy

The key bottleneck of tensor network techniques lies in their limited capacity to encode entanglement, while quantum computers naturally use entanglement. However, the noise inherent to quantum devices prevents them from running deep quantum circuits, and therefore they are also limited in terms of entanglement production. After having looked at the fidelity, we propose here to consider the entanglement as a performance metric to compare MPS solutions with noisy quantum circuits. The depolarizing noise model used here captures the effect of noise on entanglement production. Indeed, it can be understood as a process of non-destructive local measurements, where the density gets mixed with states with a lower entanglement level. Therefore, after applying a two-qubit gate, there exists a competition between the entanglement generated by the gate and the noise occurring that reduces the quantum correlations. To quantify the growth of quantum correlations in a noisy circuit, we use the operator entanglement entropy of the density matrix which was introduced in [138, 139], in the context of the simulation of noisy circuits with MPS techniques. In the case of density matrix calculations, the

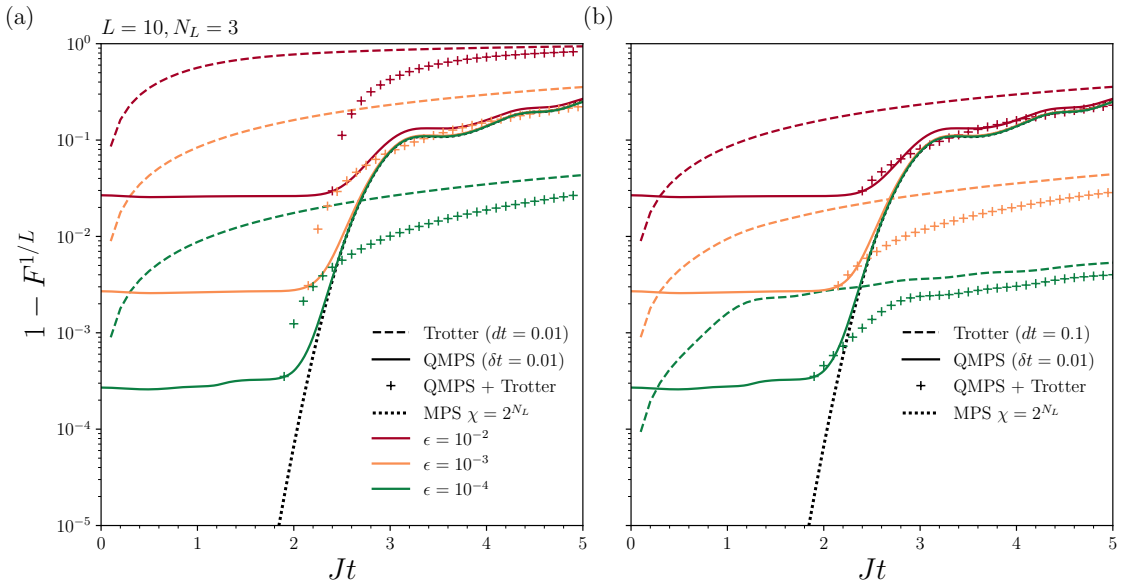

Figure 4.15: The infidelity per site as a function time for different noise level in the case of $L = 10$ and an optimized circuit of depth $N_L = 3$. The time step δt used for the MPS time evolution was set to 0.01. The dashed lines correspond to noisy Trotter circuits with a time step (a) $dt = 0.01$ and (b) $dt = 0.1$, while continuous lines represent the noisy QMPS circuits with a time step $\delta t = 0.01$. The cross points show the infidelity of QMPS evolved under Trotter circuits with a time step dt on a noisy device. The dotted line corresponds the infidelity of the MPS with bond dimension $\chi = 2^{N_L}$.

operator entanglement entropy S_{op} can be obtained thanks to a Schmidt decomposition of the density matrix ρ for a cut between subsystems A and B:

$$\rho = \sum_{\alpha=1}^{2^L} \lambda_\alpha \rho_\alpha^A \otimes \rho_\alpha^B, \tag{4.32}$$

where ρ_α^A and ρ_α^B are reduced density matrices for the two subsystems of pure states, and $\{\lambda_\alpha\}$ are the Schmidt values. Here λ_α corresponds to the classical probability of finding the state in $\rho_\alpha^A \otimes \rho_\alpha^B$ in the mixed state ρ. From this decomposition, the operator entanglement entropy is defined as

$$S_{\text{op}} = -\sum_\alpha \frac{\lambda_\alpha^2}{\sum_\beta \lambda_\beta^2} \log_2 \left(\frac{\lambda_\alpha^2}{\sum_\beta \lambda_\beta^2} \right). \tag{4.33}$$

As detailed in [138], it is important to note that although S_{op} does not distinguish between quantum and classical correlations, it vanishes for the maximally mixed state $\rho = \mathbb{1}/2^L$ that is typically obtained in the deep circuit limit under a depolarizing noise. Moreover,

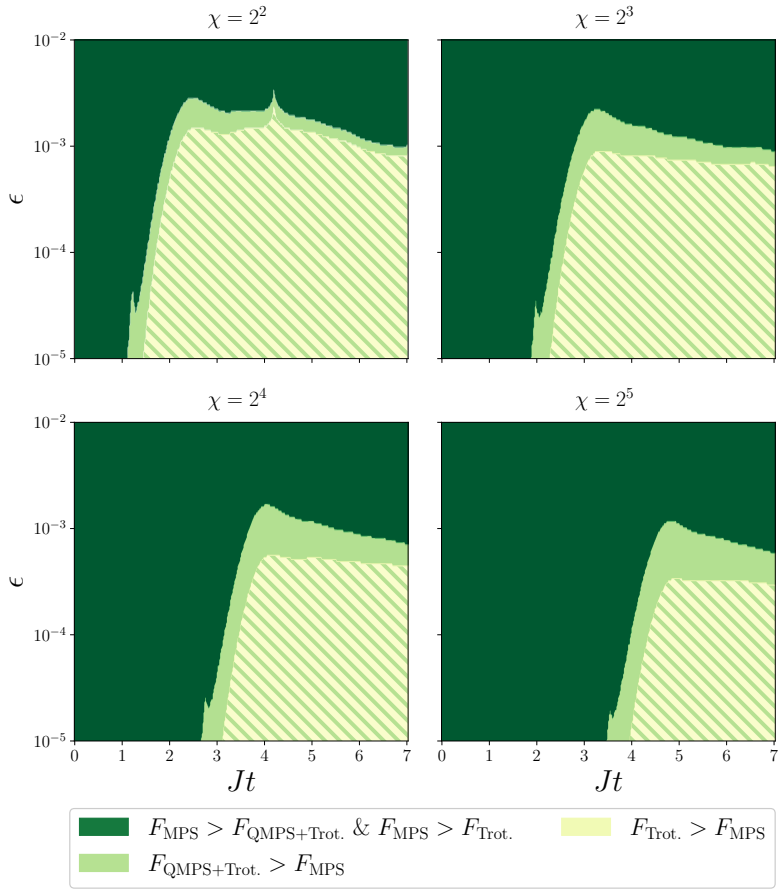

Figure 4.16: For different bond dimensions, an estimation of the diagram of practical advantage over the MPS in terms of fidelity as a function of time and noise level of the two-qubit gates with $L = 18$ spin sites. The domains are defined as follows: dark green: no advantage over the MPS, green: advantage with the combinaison of the QMPS and Trotter evolution on the noisy quantum device, and light green: advantage with the Trotter evolution on the quantum computer with or without the QMPS. The fidelities for the noisy states are estimated with Eqs. 4.30 and 4.31.

the von Neumann entropy is related to the entanglement entropy operator (for pure states only) as, $S_{\text{op}} = 2S_{\text{vN}}$, which allows for a comparison with noiseless simulations.

Fig. 4.17 displays this competition between the entanglement growth and noise. The operator entanglement entropy increases as we perform more Trotter steps until a maximum simulation time (or equivalently a maximum circuit depth) where a maximum is reached, before decreasing to zero. To beat classical MPS solutions and reach a practical quantum advantage, it seems necessary to find the best use of quantum resources. As the limited amount of entanglement is the bottleneck of MPS techniques, we propose a protocol based on the production of entanglement to finetune the time step dt. We first model the density matrix of the noisy state ρ as a mixture of the pure state density matrix $\rho_0 = |\Psi\rangle\langle\Psi|$ and a maximally mixed state $\mathbb{1}/2^L$ as

$$\rho = \alpha\rho_0 + (1-\alpha)\frac{\mathbb{1}}{2^L},\ \alpha \in [0,1]. \tag{4.34}$$

From this ansatz, Ref. [139] showed that, in the limit of $1/2^L \gg 1$, S_{op} can be approximated

$$S_{\text{op}}(\rho) \simeq \frac{S_{\text{op}}(\rho_0)}{1+\frac{1}{2^L\alpha^2}} \tag{4.35}$$

$$= \frac{2S_{\text{vN}}(|\Psi\rangle)}{1+\frac{1}{2^L\alpha^2}}. \tag{4.36}$$

We choose the coefficient $\alpha = (1-\epsilon)^{(L\times D)} \simeq e^{-\epsilon DL}$ where D is the circuit depth. In the context of the study of global quenched quantum systems, the entanglement entropy grows linearly with time such that $S_{\text{vN}}(|\Psi(t)\rangle) = \gamma t$. Plugging this along with $D = t/dt$ into Eq. 4.35, we obtain that

$$S_{\text{op}}(t) \simeq \frac{2\gamma t}{1+e^{\frac{t-t^*}{w}}}, \tag{4.37}$$

with $t^* = \frac{\ln 2 dt}{2\epsilon}$ and $w = \frac{dt}{2\epsilon L}$. Therefore, the maximum simulation time t_{max} is defined as the time where S_{op} reaches its maximum before decreasing to zero. By inspecting Eq. 4.37, the operator entanglement entropy results from the product of the noiseless operator entanglement entropy and a step function, transitioning from one to zero at a specific time point $t = t^*$, with a characteristic width w. Thus, t_{max} is approximated by

$$t_{\text{max}} \equiv t^* - w \tag{4.38}$$

$$= \frac{dt}{2\epsilon}(\ln 2 - \frac{1}{L}) \underset{L\to+\infty}{\longrightarrow} \frac{\ln 2 dt}{2\epsilon}. \tag{4.39}$$

Is it important to notice that $t_{\max}$ becomes independent of system size for large L, which makes the following conclusions valid for larger system sizes than the one simulated here. In the regime of small dts where the entanglement per Trotter step remains γdt, one can use Eq. 4.38 to estimate the best time step dt to reach a simulation time equal to $t_{\max}$. Despite being introduced in [139] for time-evolution under random unitaries, this model provides a good estimate of $t_{\max}$ in the case of Hamiltonian digital simulation as shown with Fig. 4.18.

However, this can be adapted when Trotter steps are applied to a QMPS initial state. For $t = t_{\max}^{\mathrm{MPS}}$ reached by a circuit of depth N_L, the operator entanglement entropy with noise can be estimated as:

$$S_{\mathrm{op}}(t_{\max}^{\mathrm{MPS}}) \simeq \frac{2\gamma t_{\max}^{\mathrm{MPS}}}{1 + \frac{e^{2\epsilon N_L L}}{2^L}}. \tag{4.40}$$

In practice, $\epsilon N_L \ll 1$, and thus $S_{\mathrm{op}}(t_{\max}^{\mathrm{MPS}}) \simeq 2\gamma t_{\max}^{\mathrm{MPS}}$. Equivalently, this assumes that the noise level is sufficiently low so that the QMPS can be implemented without entanglement loss. Therefore we can simply modify the estimation by taking

$$S_{\mathrm{op}}(t) \simeq \frac{2\gamma(t + t_{\max}^{\mathrm{MPS}})}{1 + e^{\frac{t-t^*}{w}}}. \tag{4.41}$$

The optimal time step dt_{opt} to reach the peak of entanglement at the desired time simulation t_{sim} as

$$dt_{\mathrm{opt}} = \frac{2\epsilon}{\ln 2}(t_{\mathrm{sim}} - t_{\max}^{\mathrm{MPS}}). \tag{4.42}$$

Eq. 4.42 shows that using the QMPS allows to perform a digital quantum simulation with a better time resolution and lower Trotter errors than Trotter circuits while reaching at least the same level of operator entanglement entropy.

4.5 Experimental results

In our numerical study, we have considered quantum circuits built from two-qubit gates under a depolarizing noise. In this Section, we explore the benefits of combining QMPS and quantum computers on actual quantum devices from IBM Quantum [6].

To evaluate the performance of the quantum devices, we follow the dynamics of the transverse field Ising model by measuring the magnetization $\langle Z_i \rangle$ of each spin 1/2 in time and compare with both exact MPS and truncated MPS solutions. Starting from an antiferromagnetic product state of size $L = 4$ and $L = 8$, we perform quantum simulations implementing Trotter and QMPS+Trotter circuits. We use optimized QMPS with $N_L = 1$

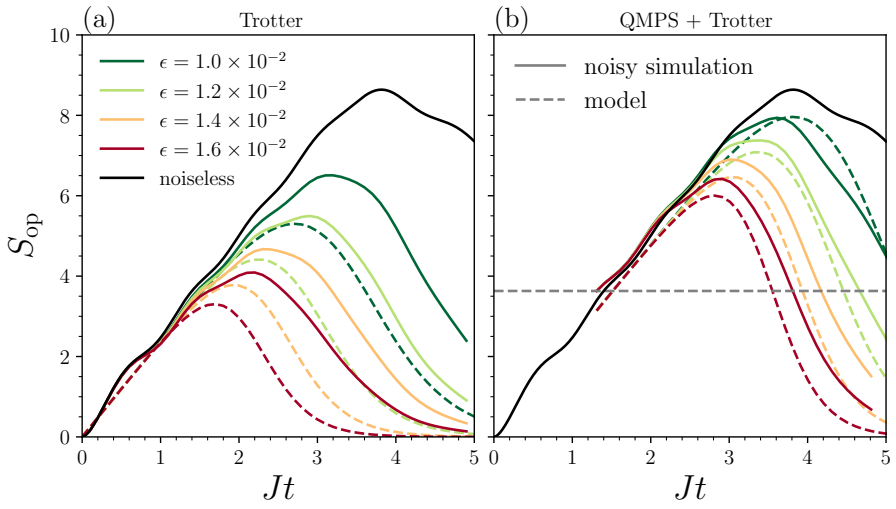

Figure 4.17: Operator entanglement entropy S_{op} versus time for different noise levels in (a) noisy Trotter circuits (b) noisy QMPS + Trotter circuits for $L = 10$ and $dt = 0.1$. The solid lines correspond to the noisy simulations while the dashed lines represent the model expressed in Eqs. (4.37) and (4.41).

and 2 layers implemented as initial states, which encode time-evolved MPS states brought to their entanglement saturation time, here $t_{\mathrm{max}}^{\mathrm{MPS}} = 0.8$ for $L = 4$, $N_L = 1$ and $t_{\mathrm{max}}^{\mathrm{MPS}} = 1.6$ for $L = 8$, $N_L = 2$. For both instances, the corresponding QMPS allows capturing half of the maximum entanglement entropy with respect to the system size. The time step of the Trotter steps dt was set to 0.1.

To make the best use of the current quantum devices, we employ several error mitigation strategies such as Pauli twirling, dynamical decoupling, measurement error mitigation, and pulse-scaling as implemented in qiskit [163] and qiskit-research [164], which have been utilized in previous works [165, 166, 167]. We also select the physical qubits to use considering their experimental error rates. To efficiently implement the QMPS circuits defined by optimized unitary matrices, we use the pulse-efficient decomposition as suggested in [168], which leverages native cross-resonance gates from IBMQ superconducting devices. Instead of using a CNOT-based decomposition, we express our two-qubit gates as a sequence of R_{xx}, R_{yy}, and R_{zz} gates (and single-qubit rotations). Each of these two-qubit rotations is performed by a native cross-resonance pulse. A native cross-resonance pulse realizes a $R_{zx}(\theta)$ gate in a shorter duration than a CNOT and therefore makes better use of the limited coherence time.

To implement the Trotter circuits, we simplify the circuits by using R_{xx} and R_z gates. Similarly, the R_{xx} gates are also performed by a pulse-efficient R_{zx} gate. When evolving the QMPS initial states prepared by sequential circuits, the Trotter steps are performed

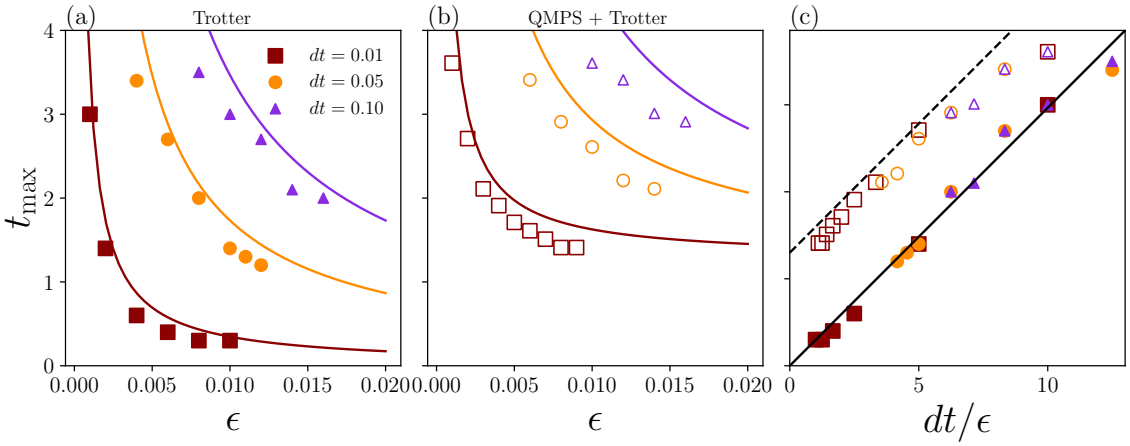

Figure 4.18: Time $t_{\max}$ corresponding to the maximum operator entanglement entropy reached by the noisy circuit, as a function of the ratio dt/ϵ for $dt = 0.01, 0.05$ and 0.1. The noise error rates were taken from 2×10^{-2} to 10^{-3}.

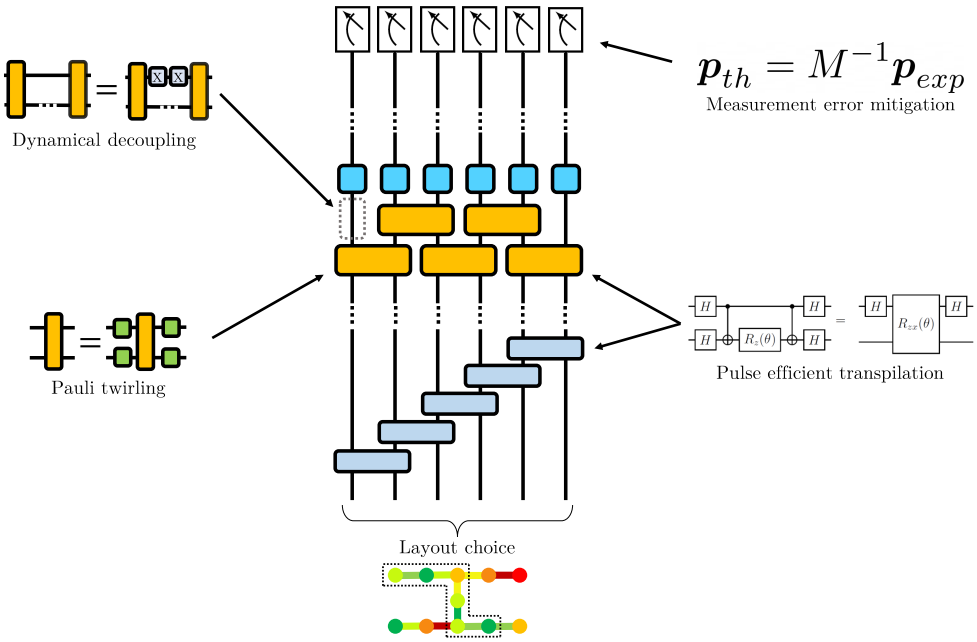

Figure 4.19: A summary of the error mitigation techniques used for the Trotter and QMPS+Trotter simulations.

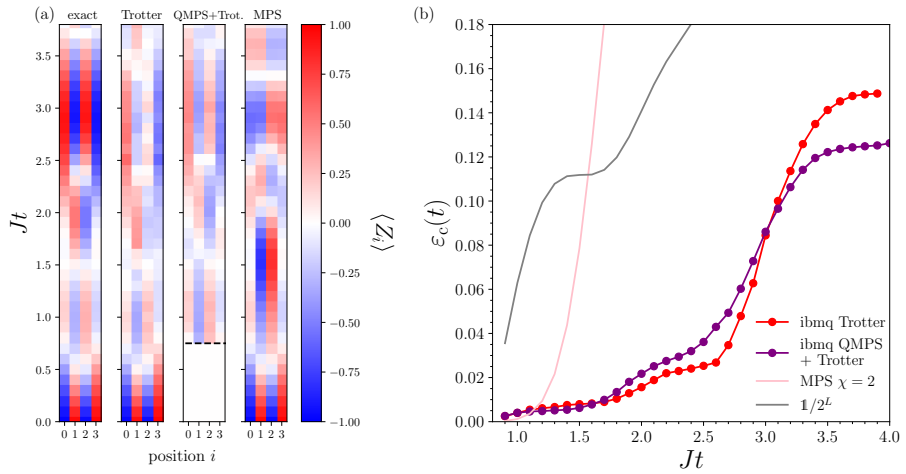

Figure 4.20: Evolution in time of the local magnetization for a $L = 4$ quantum Ising chain. The QMPS is described with 1 sequential layer of two-qubit gates, optimized via a MPS of dimension 2. (a) Colorplot showing the magnetization for exact and truncated MPS solutions as well as Trotter and QMPS+Trotter circuits from `ibm_auckland`. (b) The cumulated error in local magnetizations over time for the MPS solution, the QPU results, and a maximally mixed state $\mathbb{1}/2^L$.

in a sequential fashion instead of brickwall circuits to minimize the idle time of the qubits. To mitigate coherent errors, we average over 5 instances of Pauli twirls, which consist in applying single-qubit Pauli gates before and after an R_{xx} gate. The Pauli gates are randomly chosen from the set of Pauli transformations that leave the R_{xx} gate invariant. Finally, to measure expectation values, we use 100,000 shots per Pauli-twirled circuit. Fig. 4.19 summarizes the error mitigation techniques employed here.

Figures 4.20 and 4.21 show the results obtained from `ibmq_auckland` for $L = 4$ and $L = 8$ respectively. We compute the local magnetization from the QPU and compare with both exact and MPS of bond dimension $\chi = 2^{N_L}$ simulations. In order to quantify the performances of the different methods, we use the cumulated error of the local magnetizations over time as in [167], which we define as:

$$\varepsilon_c(t) = \frac{1}{t - t_{\max}^{\mathrm{MPS}}} \int_{t_{\max}^{\mathrm{MPS}}}^{t} dt' \frac{1}{L} \sum_{i=1}^{L} |\langle Z_i \rangle(t') - \langle Z_i \rangle_{\mathrm{exact}}(t')|^2 \tag{4.43}$$

We first observe that the time evolution with Trotter circuits allows us to recover the short time dynamics and are competitive against the low bond dimension MPSs used here that fail beyond their $t_{\max}^{\mathrm{MPS}}$. This is especially true for local magnetization in the bulk of the spin chain where the entanglement entropy gets the largest. However, as expected, the quality of the results degrades as the circuit gets deeper. On the other hand,

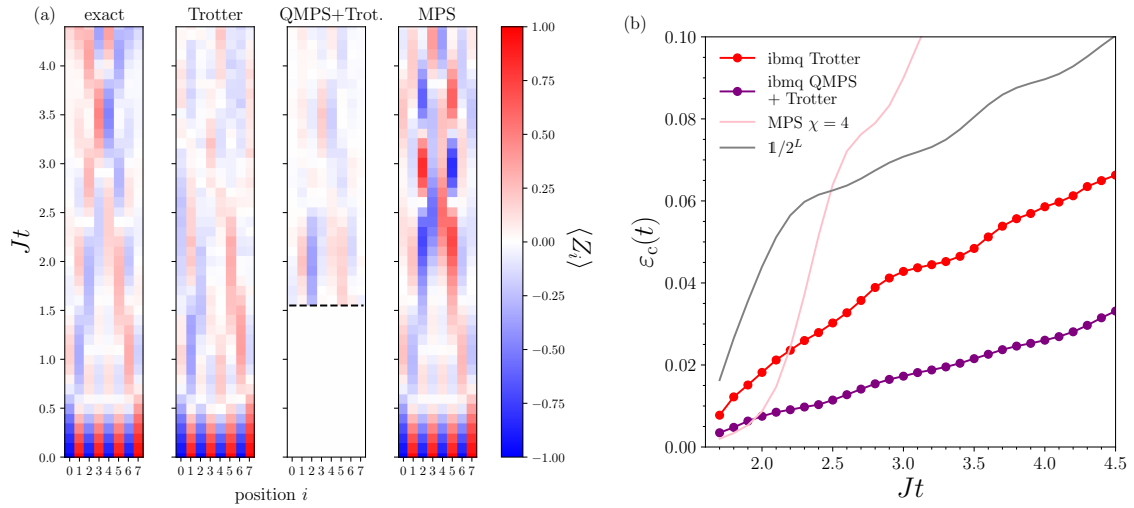

Figure 4.21: Evolution in time of the local magnetization for a L=8 quantum Ising chain. The QMPS is described with 2 sequential layers of two qubit gates, optimized via a MPS of dimension 4. (a) Colorplot for exact and truncated MPS solutions as well as Trotter and QMPS+Trotter circuits from `ibm_auckland`. (b) The cumulated error in local magnetizations over time for the MPS solution, the QPU results and a maximally mixed state $\mathbb{1}/2^L$.

starting the simulation from a QMPS produces better results and beats the corresponding MPS. In Figs 4.20a and 4.21a, we observe qualitatively the key features of the local magnetization for longer times than both Trotter evolution from the quantum device and from the corresponding MPS solution. With Figs. 4.20b and 4.21b, the cumulated error $\varepsilon_c(t)$ allows for more quantitative comparisons. For the 4-qubit example (Fig. 4.20), the cumulated errors for the Trotter and QMPS+Trotter circuits are comparable. The QMPS + Trotter scheme gains a slight advantage only for longer times. Indeed, with a $N_L = 1$ QMPS, the saving in terms of two-qubit gates is not substantial. However on the 8-qubit simulation (Fig. 4.21), the $N_L = 2$ QMPS offers a larger gain in terms of circuit depth. This translates into a significant improvement in the cumulated error. The local magnetizations as a function of time are displayed in Appendix 4.7.

In these two small instances, we demonstrate that a low-bond dimension MPS can be extended by a quantum computer, which allows one to study the dynamics of a quantum system beyond the MPS capabilities. Extending these experiments for larger instances combined with MPS of larger bond dimensions could lead to interesting insights into the capacities of current quantum devices.

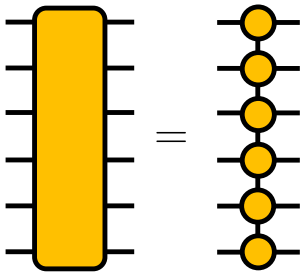

Figure 4.22: An operator such as a unitary transformation can be represented by a MPO, a one-dimensional tensor network.

4.6 Optimizing quantum circuits with Matrix Product Operators: towards a fully tensor-network-optimized quantum simulation

In the work above, we have been simulating the dynamics of a quantum spin system. To do this, we have used the TEBD algorithm that can be run either with MPSs or on a quantum computer. Assuming MPSs with a fixed bond dimension, we pushed the MPSs simulation with a quantum circuit representation to its limit. To continue the simulation, we bring the QMPS state to a quantum computer to run the rest of the quantum circuit.

Despite having reached the classical limit (set by the bond dimension) for the time-evolved state, it remains possible to further classically manipulate and optimize parts of the quantum circuit that will be run onto the QMPS. In this section, we propose to find better quantum circuits for the Trotter time evolution by leveraging Matrix Product Operators (MPO). As shown in Fig. 4.22, we use a one-dimensional tensor network structure similar to MPSs to encode an operator acting on a quantum state.

Similarly to a MPS, a MPO is also characterized by its bond dimension, which relates the classical cost to store and manipulate the operator. To exactly represent a general N-qubit operator, we need a MPO of bond dimension $4^{N/2} = 2^N$. However, quantum circuits that generate a moderate amount of entanglement can be efficiently encoded as MPOs of moderate bond dimension. In this section, we compress Trotter quantum circuits into short-depth quantum circuits. We use the same approach as the one used for the optimization of QMPSs. First, as shown in Fig. 4.23a that sequential quantum circuit of depth N_L^{MPO} can be represented exactly as a MPO of bond dimension $4^{N_L^{\text{MPO}}}$. These circuits will be our ansatz to encode Trotter circuits. Fig. 4.23b shows that a MPO representation of the Trotter circuits can be obtained by performing the TEBD algorithm on the identity MPO defined as the tensor product of the single-qubit identity operators

$\otimes_{i=1}^{L}\mathbb{1}_i$, whose MPO pictorial representation is simply L parallel lines. Then, the gates are applied sequentially onto pairs of local tensors, which are then split by an SVD, in the same fashion as the MPS algorithm. By doing so for n Trotter steps, we obtain the MPO approximation for the time evolution operator at time ndt. We fix the bond dimension to $4^{N_L^{\text{MPO}}}$, which limits the simulation time or circuit depth that we can efficiently encode as a MPO. Here we use Trotter circuits with $dt = 0.01$ as our reference circuits.

To evaluate the fidelity F_{op} between two unitaries U and V of dimension 2^L acting on L qubits, we use the Frobenius norm defined as

$$F_{\text{op}} = \frac{\text{Tr}(U^\dagger V)}{2^L}. \tag{4.44}$$

Calculating $\text{Tr}(U^\dagger V)$ where two U and V are MPOs of bond dimension χ_{MPO} with local physical dimension d (= 2 in case of qubits) can be done by contracting the tensor network shown in Fig.4.22c, whose computational cost scales as $\mathcal{O}(L(d^2\chi_{\text{MPO}})^3)$. It is important that if the MPS simulations and QMPS optimizations are performed with bond dimension χ_{MPS} (with computational scaling as $\mathcal{O}(L(d\chi_{\text{MPS}}^3)$), the maximum MPO bond dimension χ_{MPO} must be set accordingly as χ_{MPS}/d ($\chi_{\text{MPS}}/2$ for qubits). We also emphasize that exact MPS simulations can be done with a bond dimension $2^{L/2}$. Therefore, the maximum relevant MPO bond dimension is bounded by $2^{L/2}/2 = 2^{L/2-1}$, which leads to a maximum number of layers equal to $\log_4(2^{L/2-1})$.

In the same fashion as for QMPSs, we want to maximize the overlap between the quantum circuit ansatz from Fig.4.22a (that we will call Quantum Matrix Product Operator or QMPO) and the MPO approximation of the time evolution operator U_{Tr}. To optimize a given unitary U_k from the QMPO, we calculate the environment tensor of U_k by removing the gate from the overlap tensor contraction. The gate U_k is then updated from the SVD of the environment tensor. We perform optimization sweeps with a maximum number of sweeps set to $n_{\text{sweep}} = 100$. The convergence is reached when performing an optimization sweep does not improve the fidelity more than 10^{-8}. Note that similar approaches [169, 170] proposed to optimize quantum circuits for quantum simulation with MPOs by minimizing variational parameters of a given quantum circuit ansatz with an optimizer, while here the optimization is performed by a purely tensor network technique.

In Fig. 4.24, we show the operator infidelity per site for a chain of $L = 12$ sites for $N_L^{\text{MPO}} = 1$ and 2 as a function of time $t = ndt$, where $dt = 0.01$. We observe as expected that the short-time evolution is efficiently captured by the QMPOs, but degrades over time as the fixed number of layers bounds the entanglement entropy that is carried by the quantum circuits. We compare the performances of the QMPOs with 1st-order Trotter circuits employing the same number of layers (i.e. same number of gates) with time step

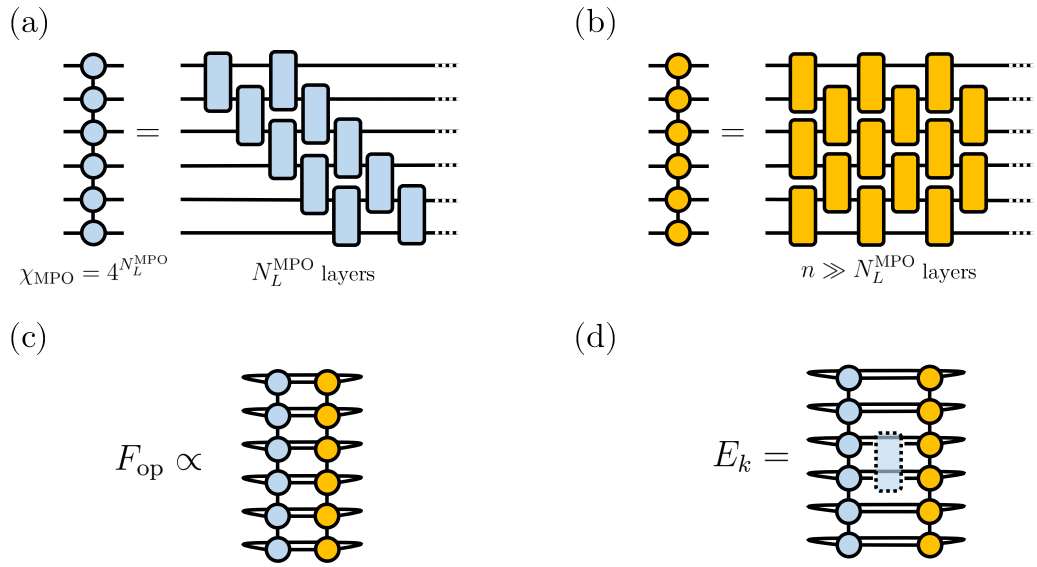

Figure 4.23: (a) A sequential quantum circuit of depth N_L^{MPO} can be exactly encoded as an MPO of bond dimension $4^{N_L^{\text{MPO}}}$. (b) The Trotter circuit approximating the time-evolution operator can also be encoded as an MPO by performing a TEBD scheme on the identity MPO. A MPO will be able to efficiently encode a number n of time steps that is limited by its bond dimension. (c) The overlap between two MPOs representing quantum circuits can be calculated from the contraction of the input and output physical indices of the two MPOs. (c) To find the unitary U_k that maximises the overlap between two MPOs, we compute its environment tensor E_k.

$dt = t/N_L^{\text{MPO}}$. While the QMPO errors are coming from the optimization process and the choice of the ansatz, the Trotter circuits suffer from errors inherent to the Trotter approximation. However, as shown in 4.24, the optimized QMPOs offer better operator fidelities than the Trotter circuits at a constant number of gates. Note that higher-order of the Trotter approximation can be used to lower the errors. While using higher-order Trotter circuits only increases the overhead of the QMPO optimization procedure, it results in the use of more quantum resources and therefore more noise when run on an actual device.

We can now perform fully tensor-network-optimized quantum simulations by using QMPS and QMPO, which we will label as "QMPSO" simulations. In this framework, tensor networks assist the quantum simulation by providing all the ingredients (i.e. the initial state and the quantum circuits) to perform time evolution with fewer quantum resources. To do so, we define a maximum simulation for the MPS/QMPS as $t_{\text{max}}^{\text{MPS}}$ as well as for the MPO/QMPO $t_{\text{max}}^{\text{MPO}}$. While To reach a simulation time $t > t_{\text{max}}^{\text{MPS}}$, we decompose

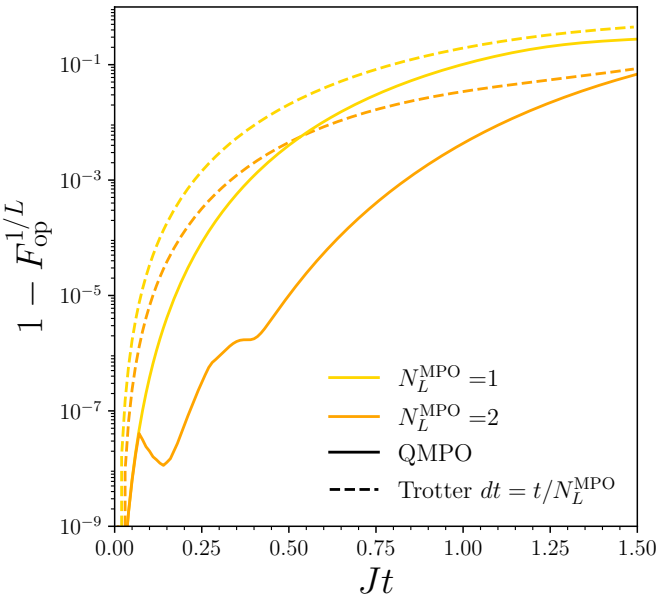

Figure 4.24: The operator infidelity per site for the QMPO solutions for different number of layers N_L^{MPO} against time for $L = 12$ sites. We compare the QMPO circuits with 1st-order Trotter circuits of same depth with a corresponding time step $dt = t/N_L^{\mathrm{MPO}}$.

t as $t = t_{\mathrm{max}}^{\mathrm{MPS}} + M \times t_{\mathrm{max}}^{\mathrm{MPO}} + \Delta t$, where $M = \lfloor \frac{t - t_{\mathrm{max}}^{\mathrm{MPS}}}{t_{\mathrm{max}}^{\mathrm{MPO}}} \rfloor$. By denoting quantum circuits for the QMPS and QMPO by $U_{\mathrm{QMPS}}(t)$ and $U_{\mathrm{QMPO}}(t)$, the time-evolved state is given by

$$|\Psi_{\mathrm{QMPSO}}(t)\rangle = U_{\mathrm{QMPO}}(\Delta t) U_{\mathrm{QMPO}}(t_{\mathrm{max}}^{\mathrm{MPO}})^M U_{\mathrm{QMPS}}(t_{\mathrm{max}}^{\mathrm{MPS}}) |\Psi_0\rangle . \tag{4.45}$$

Instead of performing costly density matrix simulations, we use the phenomenological rule for the fidelity by multiplying the noiseless fidelity of the resulting states by $e^{-\epsilon N_g}$ with ϵ being the error rate for a two-qubit unitary and N_g the number of gates. Fig. 4.25 shows the results for the case of 12 sites. We compare the performances of the QMPSO scheme in terms of fidelity against MPS solutions with bond dimension $\chi_{\mathrm{MPS}} = 2^3$ and 2^5, which correspond respectively to $N_L^{\mathrm{MPS}} = 3$ and $N_L^{\mathrm{MPO}} = 1$ and $N_L^{\mathrm{MPS}} = 5$ and $N_L^{\mathrm{MPO}} = 2$.

We observe that the same circuit can be realized by a noisy quantum device and beat an MPS of a set bond dimension by optimizing the quantum circuit with tensor network tools used here with a controlled classical cost. Using QMPS together with QMPO is a powerful technique that makes the best use of classical resources for quantum simulation. As optimizing QMPOs requires a larger bond dimension than QMPSs, initializing the simulation with an optimized QMPS allows us to reach longer times and make better use of the available classical resources. It allows us to perform quantum simulation with small time steps, limiting Trotter errors, while using much shorter quantum circuits. With Fig.

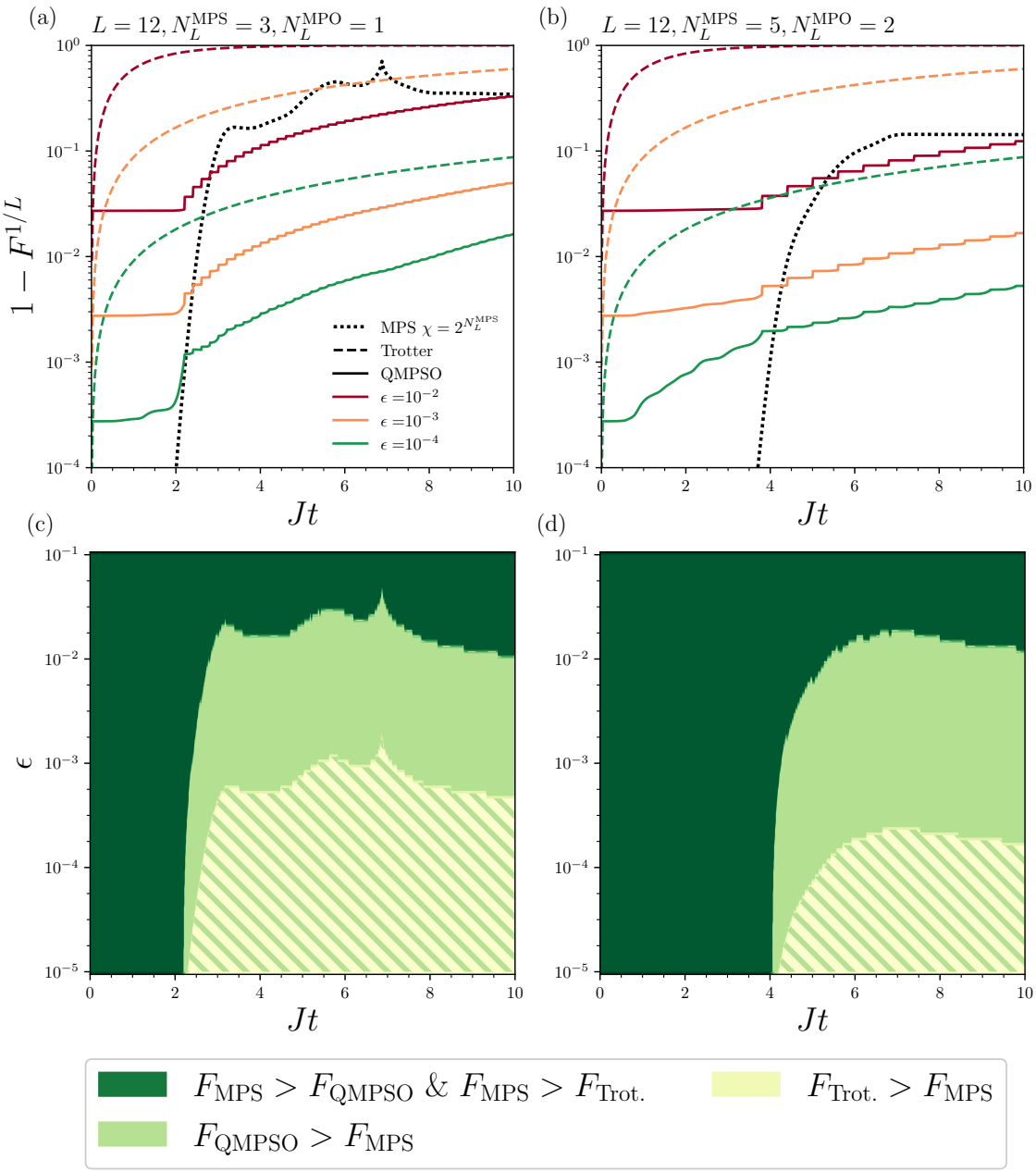

Figure 4.25: The infidelity per site for the QMPSO scheme for different error rate against the MPS solution for (a) $\chi_{\mathrm{MPS}} = 2^3, N_L^{\mathrm{MPS}} = 3$, $t_{\mathrm{max}}^{\mathrm{MPS}} = 2.2$, $N_L^{\mathrm{MPO}} = 1$ and $t_{\mathrm{max}}^{\mathrm{MPO}} = 0.15$ and (b) $\chi_{\mathrm{MPS}} = 2^5, N_L^{\mathrm{MPS}} = 5$,$t_{\mathrm{max}}^{\mathrm{MPS}} = 3.8$, $N_L^{\mathrm{MPO}} = 2$ and $t_{\mathrm{max}}^{\mathrm{MPO}} = 0.6$. The plots (c) and (c) represent the diagram of advantage.

4.25c&d, we see that running the Trotter circuit on a noisy device would require noise level orders of magnitude lower to be able to beat the classical MPS, while the QMPSO simulation offers an advantage in this example with noise level close to current NISQ performances.

4.7 Conclusion

In this chapter, we have investigated the interplay between classical MPS techniques and noisy quantum computers for digital simulations of 1D spin systems. While MPSs are constrained by their bond dimension, which limits their capacity to represent highly entangled states, quantum computers suffer from experimental noise. Combining classically tractable MPSs and efficient quantum circuits is therefore essential to get the most out of quantum devices. In order to bridge the gap between MPSs and quantum computers, we have used tensor network techniques to encode MPSs into classically optimized quantum circuits (QMPS). We propose here to take QMPSs brought to their maximal capacities and use noisy quantum computers to break the MPS entanglement barrier. This relay from classical to quantum computers enables us to make efficient use of limited quantum resources to reach a higher level of entanglement. To illustrate this protocol, we have studied a global quench of the critical transverse field Ising Hamiltonian. In this system, the entanglement entropy exhibits a ballistic growth with time, which makes almost impossible the simulation of the system's dynamics over long timescales with MPS-based approaches.

Through density matrix calculations, we have simulated noisy quantum circuits under a depolarizing noise and characterized the resulting states with their fidelity as well as with the operator entanglement entropy, which quantifies the non-trivial correlations that build up in the noisy quantum circuits. We have compared the ability of quantum computers to beat MPS techniques with respect to target simulation times and the noise level of the devices. The use of QMPSs can provide a significant improvement over the Trotter-Suzuki time-evolution as it reduces the circuit depth and reduces the error rate requirements for practical advantage. The production of entanglement is also a key component of quantum simulation. From this perspective, we have demonstrated that combining MPSs and quantum computers is a promising approach in order to reach an entanglement level beyond classical capabilities for physically relevant problems in condensed matter physics. We also have provided guidance on the choice of the Trotter time step to reach a specific time while maximizing the entanglement production. Finally, we tested experimentally this protocol on actual quantum devices from IBM Quantum [6]. We observe improved results thanks to the use of QMPSs compared to Trotter simulations. We also demonstrated in small instances the ability of current devices to beat a low bond dimension MPS solution. Comparing QPU computations with MPSs with different bond dimensions could also provide interesting insights into the performances of quantum computers with respect to a given classical complexity.

However, we emphasize that the MPS ansatz is particularly suited for 1D spin systems

with local interactions, but becomes less efficient for 2D systems or systems with long-range interactions, while a quantum computer can be designed with the appropriate topology. Other tensor network topologies and their relationships with quantum circuits could also be considered. Moreover, time-evolution with Trotter-Suzuki circuits leads to high depth $D = t/dt$ that are particularly inefficient in terms of noise and entanglement production. On the other hand, the QMPS representation shows that circuits of depth D are sufficient to encode time-evolved states with an entanglement entropy $S_{\mathrm{vN}} \lesssim D$. To address this challenge, we utilize Matrix Product Operators to enhance the efficiency of the quantum circuit for time evolution. Simultaneously, we leverage classical resources to generate efficient quantum circuits that execute time evolution with reduced quantum resource requirements. Within this framework, classical techniques supply all the components for the quantum simulation, with the quantum computer exclusively responsible for preparing the resulting state.

Appendix of Chapter 4

Here we show the local magnetization of the quantum simulations carried on `ibm_auckland` for each site. Fig. 4.26 show the results obtained for the 4 qubit instance, while Fig. 4.27 displays the 8 qubit data. On the 4 qubit example, both schemes (Trotter vs QMPS+Trotter) offer similar performances as noted in 4.5. We also observe discrepancies with respect to site that manifest the quality variability of the qubits and their couplings. Similar behaviors are observed in the 8 qubit examples. However, the QMPS used here allows to reach longer times efficiently which translates into a substantial gain in terms of the number of two-qubit gates. As a result, the measured local magnetizations show a good match with exact magnetizations at times immediately following time $t_{\text{max}}^{\text{MPS}}$ and capture the correct behavior over longer times.

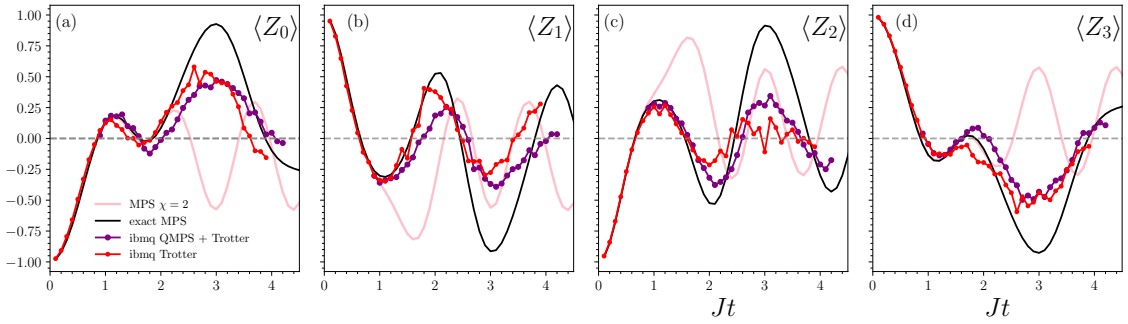

Figure 4.26: Local magnetization of each site from the 4-qubit simulation.

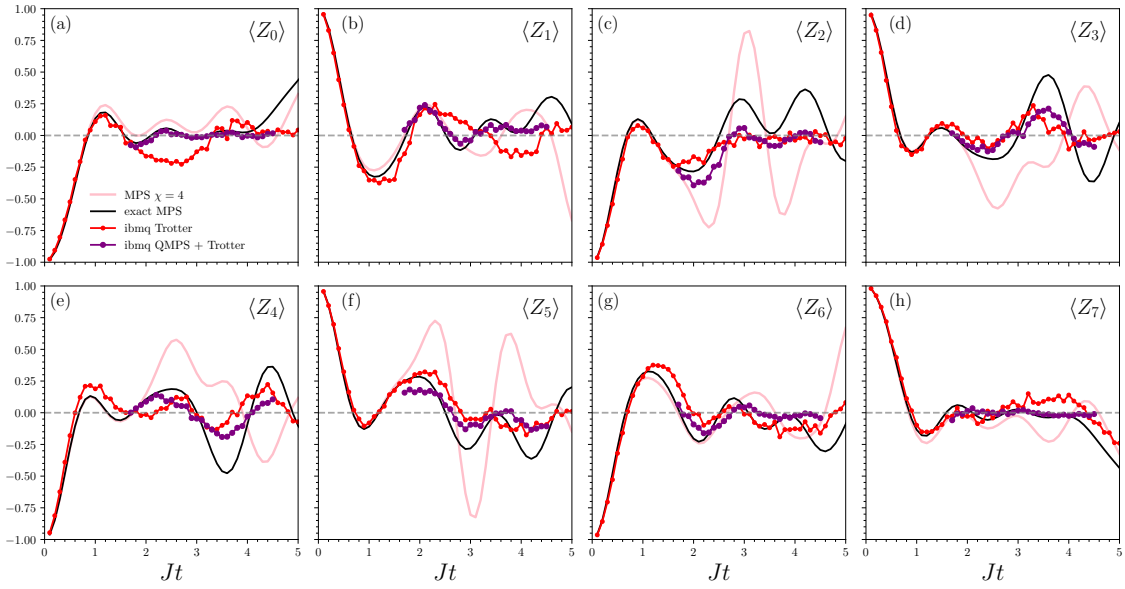

Figure 4.27: Local magnetization of each site from the 8-qubit simulation.

Bibliography

[1] C. H. Bennett. Logical reversibility of computation. *IBM Journal of Research and Development*, 17(6):525–532, November 1973.

[2] R.P. Poplavskii. Thermodynamic models of information processes. *Uspekhi Fizicheskih Nauk*, 115(3):465, 1975.

[3] Paul Benioff. The computer as a physical system: A microscopic quantum mechanical hamiltonian model of computers as represented by turing machines. *Journal of Statistical Physics*, 22(5):563–591, May 1980.

[4] Tommaso Toffoli. Reversible computing. In *Automata, Languages and Programming*, pages 632–644. Springer Berlin Heidelberg, 1980.

[5] Paul A. Benioff. Quantum mechanical hamiltonian models of discrete processes that erase their own histories: Application to turing machines. *International Journal of Theoretical Physics*, 21(3-4):177–201, April 1982.

[6] IBM Quantum, 2022. https://quantum-computing.ibm.com/services.

[7] John Preskill. Quantum computing in the NISQ era and beyond. *Quantum*, 2:79, 2018.

[8] Peter W. Shor. Algorithms for quantum computation: discrete logarithms and factoring. *Proceedings 35th Annual Symposium on Foundations of Computer Science*, pages 124–134, 1994.

[9] Peter W. Shor. Polynomial-time algorithms for prime factorization and discrete logarithms on a quantum computer. *SIAM Rev.*, 41:303–332, 1995.

[10] Frank Arute, Kunal Arya, Ryan Babbush, Dave Bacon, Joseph C. Bardin, Rami Barends, Rupak Biswas, Sergio Boixo, Fernando G. S. L. Brandao, David A. Buell, Brian Burkett, Yu Chen, Zijun Chen, Ben Chiaro, Roberto Collins, William Courtney, Andrew Dunsworth, Edward Farhi, Brooks Foxen, Austin Fowler, Craig Gidney,

Marissa Giustina, Rob Graff, Keith Guerin, Steve Habegger, Matthew P. Harrigan, Michael J. Hartmann, Alan Ho, Markus Hoffmann, Trent Huang, Travis S. Humble, Sergei V. Isakov, Evan Jeffrey, Zhang Jiang, Dvir Kafri, Kostyantyn Kechedzhi, Julian Kelly, Paul V. Klimov, Sergey Knysh, Alexander Korotkov, Fedor Kostritsa, David Landhuis, Mike Lindmark, Erik Lucero, Dmitry Lyakh, Salvatore Mandrà, Jarrod R. McClean, Matthew McEwen, Anthony Megrant, Xiao Mi, Kristel Michielsen, Masoud Mohseni, Josh Mutus, Ofer Naaman, Matthew Neeley, Charles Neill, Murphy Yuezhen Niu, Eric Ostby, Andre Petukhov, John C. Platt, Chris Quintana, Eleanor G. Rieffel, Pedram Roushan, Nicholas C. Rubin, Daniel Sank, Kevin J. Satzinger, Vadim Smelyanskiy, Kevin J. Sung, Matthew D. Trevithick, Amit Vainsencher, Benjamin Villalonga, Theodore White, Z. Jamie Yao, Ping Yeh, Adam Zalcman, Hartmut Neven, and John M. Martinis. Quantum supremacy using a programmable superconducting processor. *Nature*, 574(7779):505–510, October 2019.

[11] Han-Sen Zhong, Hui Wang, Yu-Hao Deng, Ming-Cheng Chen, Li-Chao Peng, Yi-Han Luo, Jian Qin, Dian Wu, Xing Ding, Yi Hu, et al. Quantum computational advantage using photons. *Science*, 370(6523):1460–1463, 2020.

[12] Han-Sen Zhong, Yu-Hao Deng, Jian Qin, Hui Wang, Ming-Cheng Chen, Li-Chao Peng, Yi-Han Luo, Dian Wu, Si-Qiu Gong, Hao Su, Yi Hu, Peng Hu, Xiao-Yan Yang, Wei-Jun Zhang, Hao Li, Yuxuan Li, Xiao Jiang, Lin Gan, Guangwen Yang, Lixing You, Zhen Wang, Li Li, Nai-Le Liu, Jelmer J. Renema, Chao-Yang Lu, and Jian-Wei Pan. Phase-programmable gaussian boson sampling using stimulated squeezed light. *Physical Review Letters*, 127(18), oct 2021.

[13] Yulin Wu, Wan-Su Bao, Sirui Cao, Fusheng Chen, Ming-Cheng Chen, Xiawei Chen, Tung-Hsun Chung, Hui Deng, Yajie Du, Daojin Fan, Ming Gong, Cheng Guo, Chu Guo, Shaojun Guo, Lianchen Han, Linyin Hong, He-Liang Huang, Yong-Heng Huo, Liping Li, Na Li, Shaowei Li, Yuan Li, Futian Liang, Chun Lin, Jin Lin, Haoran Qian, Dan Qiao, Hao Rong, Hong Su, Lihua Sun, Liangyuan Wang, Shiyu Wang, Dachao Wu, Yu Xu, Kai Yan, Weifeng Yang, Yang Yang, Yangsen Ye, Jianghan Yin, Chong Ying, Jiale Yu, Chen Zha, Cha Zhang, Haibin Zhang, Kaili Zhang, Yiming Zhang, Han Zhao, Youwei Zhao, Liang Zhou, Qingling Zhu, Chao-Yang Lu, Cheng-Zhi Peng, Xiaobo Zhu, and Jian-Wei Pan. Strong quantum computational advantage using a superconducting quantum processor. *Physical Review Letters*, 127(18), oct 2021.

[14] Yiqing Zhou, E. Miles Stoudenmire, and Xavier Waintal. What Limits the Simu-

lation of Quantum Computers? *Physical Review X*, 10(4):041038, November 2020. Publisher: American Physical Society.

[15] Thomas Ayral, Thibaud Louvet, Yiqing Zhou, Cyprien Lambert, E. Miles Stoudenmire, and Xavier Waintal. A density-matrix renormalization group algorithm for simulating quantum circuits with a finite fidelity, August 2022. arXiv:2207.05612 [cond-mat, physics:quant-ph].

[16] Feng Pan, Keyang Chen, and Pan Zhang. Solving the sampling problem of the sycamore quantum circuits. *Physical Review Letters*, 129(9), aug 2022.

[17] Jacob F. F. Bulmer, Bryn A. Bell, Rachel S. Chadwick, Alex E. Jones, Diana Moise, Alessandro Rigazzi, Jan Thorbecke, Utz-Uwe Haus, Thomas Van Vaerenbergh, Raj B. Patel, Ian A. Walmsley, and Anthony Laing. The boundary for quantum advantage in gaussian boson sampling. *Science Advances*, 8(4), jan 2022.

[18] Alberto Peruzzo, Jarrod McClean, Peter Shadbolt, Man-Hong Yung, Xiao-Qi Zhou, Peter J Love, Alán Aspuru-Guzik, and Jeremy L O'brien. A variational eigenvalue solver on a photonic quantum processor. *Nature communications*, 5(1):1–7, 2014.

[19] Jules Tilly, Hongxiang Chen, Shuxiang Cao, Dario Picozzi, Kanav Setia, Ying Li, Edward Grant, Leonard Wossnig, Ivan Rungger, George H. Booth, and Jonathan Tennyson. The variational quantum eigensolver: A review of methods and best practices. *Physics Reports*, 986:1–128, nov 2022.

[20] Ian Affleck, Tom Kennedy, Elliott H. Lieb, and Hal Tasaki. Rigorous results on valence-bond ground states in antiferromagnets. *Phys. Rev. Lett.*, 59:799–802, Aug 1987.

[21] F. D. M. Haldane. Nonlinear field theory of large-spin heisenberg antiferromagnets: Semiclassically quantized solitons of the one-dimensional easy-axis néel state. *Phys. Rev. Lett.*, 50:1153–1156, Apr 1983.

[22] F Duncan M Haldane. Continuum dynamics of the 1-d heisenberg antiferromagnet: Identification with the o (3) nonlinear sigma model. *Physics letters a*, 93(9):464–468, 1983.

[23] J. Ignacio Cirac, David Pérez-García, Norbert Schuch, and Frank Verstraete. Matrix product states and projected entangled pair states: Concepts, symmetries, theorems. *Rev. Mod. Phys.*, 93:045003, Dec 2021.

[24] Román Orús. A practical introduction to tensor networks: Matrix product states and projected entangled pair states. *Annals of Physics*, 349:117–158, oct 2014.

[25] Ulrich Schollwöck. The density-matrix renormalization group in the age of matrix product states. *Annals of Physics*, 326(1):96–192, jan 2011.

[26] Simone Montangero. *Introduction to Tensor Network Methods*. Springer International Publishing, 2018.

[27] Sebastian Paeckel, Thomas Köhler, Andreas Swoboda, Salvatore R. Manmana, Ulrich Schollwöck, and Claudius Hubig. Time-evolution methods for matrix-product states. *Annals of Physics*, 411:167998, dec 2019.

[28] Shi-Ju Ran, Emanuele Tirrito, Cheng Peng, Xi Chen, Luca Tagliacozzo, Gang Su, and Maciej Lewenstein. *Tensor Network Contractions*. Springer International Publishing, 2020.

[29] Kouichi Okunishi, Tomotoshi Nishino, and Hiroshi Ueda. Developments in the tensor network — from statistical mechanics to quantum entanglement. *Journal of the Physical Society of Japan*, 91(6), jun 2022.

[30] Michael A. Nielsen and Isaac L. Chuang. *Quantum Computation and Quantum Information: 10th Anniversary Edition*. Cambridge University Press, 2010.

[31] A. Einstein, B. Podolsky, and N. Rosen. Can quantum-mechanical description of physical reality be considered complete? *Physical Review*, 47(10):777–780, May 1935.

[32] J. S. Bell. On the einstein podolsky rosen paradox. *Physics Physique Fizika*, 1:195–200, Nov 1964.

[33] Stuart J. Freedman and John F. Clauser. Experimental test of local hidden-variable theories. *Physical Review Letters*, 28(14):938–941, April 1972.

[34] Alain Aspect, Philippe Grangier, and Gérard Roger. Experimental tests of realistic local theories via bell's theorem. *Physical Review Letters*, 47(7):460–463, August 1981.

[35] Gregor Weihs, Thomas Jennewein, Christoph Simon, Harald Weinfurter, and Anton Zeilinger. Violation of bell's inequality under strict einstein locality conditions. *Physical Review Letters*, 81(23):5039–5043, December 1998.

[36] Wikipedia. XOR gate — Wikipedia, the free encyclopedia. http://en.wikipedia.org/w/index.php?title=XOR%20gate&oldid=1175099522, 2023. [Online; accessed 09-October-2023].

[37] G. Vidal and C. M. Dawson. Universal quantum circuit for two-qubit transformations with three controlled-NOT gates. *Physical Review A*, 69(1), jan 2004.

[38] Alexei Y. Kitaev. Quantum computations: algorithms and error correction. *Russian Mathematical Surveys*, 52:1191–1249, 1997.

[39] Adriano Barenco, Charles H. Bennett, Richard Cleve, David P. DiVincenzo, Norman Margolus, Peter Shor, Tycho Sleator, John A. Smolin, and Harald Weinfurter. Elementary gates for quantum computation. *Physical Review A*, 52(5):3457–3467, nov 1995.

[40] Daniel Gottesman. The heisenberg representation of quantum computers, 1998.

[41] Wikipedia. Quantum logic gate — Wikipedia, the free encyclopedia. http://en.wikipedia.org/w/index.php?title=Quantum%20logic%20gate&oldid=1178752367, 2023. [Online; accessed 09-October-2023].

[42] Thomas Ayral, Pauline Besserve, Denis Lacroix, and Edgar Andres Ruiz Guzman. Quantum computing with and for many-body physics. *The European Physical Journal A*, 59(10):227, 2023.

[43] David P. DiVincenzo. The physical implementation of quantum computation. *Fortschritte der Physik*, 48(9-11):771–783, sep 2000.

[44] Easwar Magesan, Jay M. Gambetta, and Joseph Emerson. Characterizing quantum gates via randomized benchmarking. *Phys. Rev. A*, 85:042311, 2012.

[45] E. Anderson, Z. Bai, C. Bischof, L. S. Blackford, J. Demmel, J. Dongarra, J. Du Croz, A. Greenbaum, S. Hammarling, A. McKenney, and D. Sorensen. *LAPACK Users' Guide*. Society for Industrial and Applied Mathematics, January 1999.

[46] Richard P Feynman. Simulating physics with computers. In *Feynman and computation*, pages 133–153. CRC Press, 2018.

[47] Dave Wecker, Matthew B. Hastings, and Matthias Troyer. Progress towards practical quantum variational algorithms. *Phys. Rev. A*, 92:042303, 2015.

[48] Jan-Michael Reiner, Frank Wilhelm-Mauch, Gerd Schön, and Michael Marthaler. Finding the ground state of the Hubbard model by variational methods on a quantum computer with gate errors. *Quantum Sci. Technol.*, 4:035005, 2019.

[49] Kristan Temme, Sergey Bravyi, and Jay M. Gambetta. Error mitigation for short-depth quantum circuits. *Phys. Rev. Lett.*, 119:180509, 2017.

[50] Abhinav Kandala. Error mitigation extends the computational reach of a noisy quantum processor. *Nature*, 567:491–495, 2019.

[51] Chris Cade, Lana Mineh, Ashley Montanaro, and Stasja Stanisic. Strategies for solving the Fermi-Hubbard model on near-term quantum computers. *Phys. Rev. B*, 102:235122, 2020.

[52] Zhenyu Cai. Resource estimation for quantum variational simulations of the Hubbard model. *Phys. Rev. Applied*, 14:014059, 2020.

[53] Roeland Wiersema, Cunlu Zhou, Yvette de Sereville, Juan Felipe Carrasquilla, Yong Baek Kim, and Henry Yuen. Exploring entanglement and optimization within the Hamiltonian variational ansatz. *PRX Quantum*, 1:020319, 2020.

[54] Edward Farhi, Jeffrey Goldstone, and Sam Gutmann. A quantum approximate optimization algorithm. *arXiv:1411.4028*, 2014.

[55] Baptiste Anselme Martin, Pascal Simon, and Marko J. Rančić. Simulating strongly interacting hubbard chains with the variational hamiltonian ansatz on a quantum computer. *Phys. Rev. Res.*, 4:023190, Jun 2022.

[56] A Yu Kitaev. Quantum measurements and the abelian stabilizer problem. *arXiv preprint quant-ph/9511026*, 1995.

[57] Aram W. Harrow, Avinatan Hassidim, and Seth Lloyd. Quantum algorithm for linear systems of equations. *Physical Review Letters*, 103(15), oct 2009.

[58] P. W. Anderson. Infrared catastrophe in fermi gases with local scattering potentials. *Phys. Rev. Lett.*, 18:1049–1051, Jun 1967.

[59] Seunghoon Lee, Joonho Lee, Huanchen Zhai, Yu Tong, Alexander M. Dalzell, Ashutosh Kumar, Phillip Helms, Johnnie Gray, Zhi-Hao Cui, Wenyuan Liu, Michael Kastoryano, Ryan Babbush, John Preskill, David R. Reichman, Earl T. Campbell, Edward F. Valeev, Lin Lin, and Garnet Kin-Lic Chan. Evaluating the evidence for exponential quantum advantage in ground-state quantum chemistry. *Nature Communications*, 14(1), apr 2023.

[60] D. R. Hartree. The wave mechanics of an atom with a non-coulomb central field. part ii. some results and discussion. *Mathematical Proceedings of the Cambridge Philosophical Society*, 24(1):111–132, 1928.

[61] J. C. Slater. Note on hartree's method. *Phys. Rev.*, 35:210–211, Jan 1930.

[62] V. Fock. Näherungsmethode zur lösung des quantenmechanischen mehrkörperproblems. *Zeitschrift für Physik*, 61:126–148.

[63] W. M. C. Foulkes, L. Mitas, R. J. Needs, and G. Rajagopal. Quantum monte carlo simulations of solids. *Rev. Mod. Phys.*, 73:33–83, Jan 2001.

[64] Robert Jastrow. Many-body problem with strong forces. *Phys. Rev.*, 98:1479–1484, Jun 1955.

[65] Abhinav Kandala, Antonio Mezzacapo, Kristan Temme, Maika Takita, Markus Brink, Jerry M. Chow, and Jay M. Gambetta. Hardware-efficient variational quantum eigensolver for small molecules and quantum magnets. *Nature*, 549:242–246, 2017.

[66] Sukin Sim, Peter D. Johnson, and Alan Aspuru-Guzik. Expressibility and entangling capability of parameterized quantum circuits for hybrid quantum-classical algorithms. *Adv. Quantum Technol.*, 2:190070, 2019.

[67] Jarrod R. McClean, Sergio Boixo, Vadim N. Smelyanskiy, Ryan Babbush, and Hartmut Neven. Barren plateaus in quantum neural network training landscapes. *Nat Commun*, 9:4812, 2018.

[68] Jonathan Romero. Strategies for quantum computing molecular energies using the unitary coupled cluster ansatz. *Quantum Sci. Technol.*, 4:014008, 2019.

[69] Pierre-Luc Dallaire-Demers, Jonathan Romero, Libor Veis, Sukin Sim, and Alan Aspuru-Guzik. Low-depth circuit ansatz for preparing correlated fermionic states on a quantum computer. *Quantum Sci. Technol.*, 4:045005, 2019.

[70] Gian-Luca R. Anselmetti. Local, expressive, quantum-number-preserving VQE ansätze for fermionic systems. *arxiv:2104.05695*, 2021.

[71] Bryan T. Gard, Linghua Zhu, George S. Barron, Nicholas J. Mayhall, Sophia E. Economou, and Edwin Barnes. Efficient symmetry-preserving state preparation circuits for the variational quantum eigensolver algorithm. *Npj Quantum Inf.*, 6:10, 2020.

[72] Kazuhiro Seki, Tomonori Shirakawa, and Seiji Yunoki. Symmetry-adapted variational quantum eigensolver. *Phys. Rev. A*, 101:052340, May 2020.

[73] Luca Crippa, Francesco Tacchino, Mario Chizzini, Antonello Aita, Michele Grossi, Alessandro Chiesa, Paolo Santini, Ivano Tavernelli, and Stefano Carretta. Simulating static and dynamic properties of magnetic molecules with prototype quantum computers. *Magnetochemistry*, 7(8):117, Aug 2021.

[74] Harper R. Grimsley, Sophia Economou, Edwin Barnes, and Nicholas J. Mayhall. An adaptive variational algorithm for exact molecular simulations on a quantum computer. *Nat. Commun.*, 10:3007, 2019.

[75] Ho Lun Tang, V. O. Shkolnikov, George S. Barron, Harper R. Grimsley, Nicholas J. Mayhall, Edwin Barnes, and Sophia E. Economou. *PRX Quantum*, 2:020310, 2021.

[76] Masuo Suzuki. Generalized Trotter's formula and systematic approximants of exponential operators and inner derivations with applications to many-body problems. *Communications in Mathematical Physics*, 51(2):183–190, June 1976.

[77] John Hubbard. Electron correlations in narrow energy bands. *Proceedings of the Royal Society of London. Series A. Mathematical and Physical Sciences*, 276(1365):238–257, 1963.

[78] Patrick A Lee. From high temperature superconductivity to quantum spin liquid: progress in strong correlation physics. *Reports on Progress in Physics*, 71(1):012501, 2007.

[79] Nevill F Mott. The basis of the electron theory of metals, with special reference to the transition metals. *Proceedings of the Physical Society. Section A*, 62(7):416, 1949.

[80] Hans Bethe. Zur theorie der metalle. *Zeitschrift für Physik*, 71(3):205–226, 1931.

[81] DJ Scalapino. Numerical studies of the 2D Hubbard model. In *Handbook of High-Temperature Superconductivity*, pages 495–526. Springer, 2007.

[82] James PF LeBlanc, Andrey E Antipov, Federico Becca, Ireneusz W Bulik, Garnet Kin-Lic Chan, Chia-Min Chung, Youjin Deng, Michel Ferrero, Thomas M Henderson, Carlos A Jiménez-Hoyos, et al. Solutions of the two-dimensional hubbard model: Benchmarks and results from a wide range of numerical algorithms. *Physical Review X*, 5(4):041041, 2015.

[83] Dave Wecker, Matthew B. Hastings, Nathan Wiebe, Bryan K. Clark, Chetan Nayak, and Matthias Troyer. Solving strongly correlated electron models on a quantum computer. *Phys. Rev. A*, 92:062318, 2015.

[84] Zhang Jiang, Kevin J Sung, Kostyantyn Kechedzhi, Vadim N Smelyanskiy, and Sergio Boixo. Quantum algorithms to simulate many-body physics of correlated fermions. *Physical Review Applied*, 9(4):044036, 2018.

[85] J. R. McClean. Openfermion: the electronic structure package for quantum computers. *Quantum Science and Technology*, 5:3, 2020.

[86] Pascual Jordan and Eugene P. Wigner. About the Pauli exclusion principle. *Z. Phys.*, 47:631–651, 1928.

[87] Guifre Vidal and Christopher M. Dawson. A universal quantum circuit for two-qubit transformations with three CNOT gates. *Phys. Rev. A.*, 69:010301(R), 2004.

[88] Ian D. Kivlichan, Jarrod McClean, Nathan Wiebe, Craig Gidney, Alán Aspuru-Guzik, Garnet Kin-Lic Chan, and Ryan Babbush. Quantum simulation of electronic structure with linear depth and connectivity. *Phys. Rev. Lett.*, 120:110501, Mar 2018.

[89] DJ Thouless. Stability conditions and nuclear rotations in the hartree-fock theory. *Nuclear Physics*, 21:225–232, 1960.

[90] Rodney J. Barlett, Stanislaw A. Kucharski, and Jozef Noga. Alternative coupled-cluster ansätze ii. the unitary coupled-cluster method. *Chemical Physical Letters*, 155:133–140, 1989.

[91] A.G. Taube and R. J. Barlett. New perspectives on unitary coupled-cluster theory. *Int. J. Quant. Chem.*, 106:3393–3401, 2006.

[92] Kohdai Kuroiwa and Yuya O. Nakagawa. Penalty methods for a variational quantum eigensolver. *Phys. Rev. Research*, 3:013197, Feb 2021.

[93] Denis Lacroix. Symmetry-assisted preparation of entangled many-body states on a quantum computer. *Phys. Rev. Lett.*, 125:230502, Dec 2020.

[94] Tzu-Ching Yen, Robert A Lang, and Artur F Izmaylov. Exact and approximate symmetry projectors for the electronic structure problem on a quantum computer. *The Journal of chemical physics*, 151(16):164111, 2019.

[95] Kazuhiro Seki and Seiji Yunoki. Spatial, spin, and charge symmetry projections for a fermi-hubbard model on a quantum computer. *arXiv preprint arXiv:2112.14077*, 2021.

[96] M. J. D. Powell. A direct search optimization method that models the objective and constraint functions by linear interpolation. 1994.

[97] M. J. D. Powell. Direct search algorithms for optimization calculations. *Acta Numerica*, 7:287–336, 1998.

[98] M. J. D. Powell. A view of algorithms for optimization without derivatives 1. 2007.

[99] Tudor Giurgica-Tiron, Yousef Hindy, Ryan LaRose, Andrea Mari, and William J. Zeng. Digital zero noise extrapolation for quantum error mitigation. In *2020 IEEE International Conference on Quantum Computing and Engineering (QCE)*. IEEE, oct 2020.

[100] Andre He, Benjamin Nachman, Wibe A. de Jong, and Christian W. Bauer. Zero-noise extrapolation for quantum-gate error mitigation with identity insertions. *Physical Review A*, 102(1), jul 2020.

[101] W. J. L Buyers, R. M. Morra, R. L. Armstrong, M. J. Hogan, P. Gerlach, and K. Hirakawa. Experimental evidence for the haldane gap in a spin-1 nearly isotropic, antiferromagnetic chain. *Phys. Rev. Lett.*, 56:371–374, Jan 1986.

[102] M. Hagiwara, K. Katsumata, Ian Affleck, B. I. Halperin, and J. P. Renard. Observation of s=1/2 degrees of freedom in an s=1 linear-chain heisenberg antiferromagnet. *Phys. Rev. Lett.*, 65:3181–3184, Dec 1990.

[103] Shantanu Mishra, Gonçalo Catarina, Fupeng Wu, Ricardo Ortiz, David Jacob, Kristjan Eimre, Ji Ma, Carlo A. Pignedoli, Xinliang Feng, Pascal Ruffieux, Joaquín Fernández-Rossier, and Roman Fasel. Observation of fractional edge excitations in nanographene spin chains. *Nature*, 598(7880):287–292, oct 2021.

[104] M. P. Nightingale and H. W. J. Blöte. Gap of the linear spin-1 heisenberg antiferromagnet: A monte carlo calculation. *Phys. Rev. B*, 33:659–661, Jan 1986.

[105] Zheng-Cheng Gu and Xiao-Gang Wen. Tensor-entanglement-filtering renormalization approach and symmetry-protected topological order. *Physical Review B*, 80(15), oct 2009.

[106] Xie Chen, Zheng-Cheng Gu, and Xiao-Gang Wen. Classification of gapped symmetric phases in one-dimensional spin systems. *Physical Review B*, 83(3), jan 2011.

[107] Frank Pollmann, Erez Berg, Ari M. Turner, and Masaki Oshikawa. Symmetry protection of topological phases in one-dimensional quantum spin systems. *Physical Review B*, 85(7), feb 2012.

[108] Frank Pollmann, Ari M. Turner, Erez Berg, and Masaki Oshikawa. Entanglement spectrum of a topological phase in one dimension. *Physical Review B*, 81(6), feb 2010.

[109] Robert Raussendorf and Hans J. Briegel. A one-way quantum computer. *Phys. Rev. Lett.*, 86:5188–5191, May 2001.

[110] F. Verstraete and J. I. Cirac. Valence-bond states for quantum computation. *Phys. Rev. A*, 70:060302, Dec 2004.

[111] D. Gross and J. Eisert. Novel schemes for measurement-based quantum computation. *Phys. Rev. Lett.*, 98:220503, May 2007.

[112] D. Gross, J. Eisert, N. Schuch, and D. Perez-Garcia. Measurement-based quantum computation beyond the one-way model. *Phys. Rev. A*, 76:052315, Nov 2007.

[113] Gavin K. Brennen and Akimasa Miyake. Measurement-based quantum computer in the gapped ground state of a two-body hamiltonian. *Phys. Rev. Lett.*, 101:010502, Jul 2008.

[114] Rainer Kaltenbaek, Jonathan Lavoie, Bei Zeng, Stephen D Bartlett, and Kevin J Resch. Optical one-way quantum computing with a simulated valence-bond solid. *Nature Physics*, 6(11):850–854, 2010.

[115] Denis Lacroix. Symmetry-assisted preparation of entangled many-body states on a quantum computer. *Phys. Rev. Lett.*, 125:230502, Dec 2020.

[116] Pooja Siwach and Denis Lacroix. Filtering states with total spin on a quantum computer. *Phys. Rev. A*, 104:062435, Dec 2021.

[117] A Klümper, A Schadschneider, and J Zittartz. Matrix product ground states for one-dimensional spin-1 quantum antiferromagnets. *Europhysics Letters (EPL)*, 24(4):293–297, nov 1993.

[118] Mark Fannes, Bruno Nachtergaele, and Reinhard F Werner. Finitely correlated states on quantum spin chains. *Communications in mathematical physics*, 144(3):443–490, 1992.

[119] Fergus Barratt, James Dborin, Matthias Bal, Vid Stojevic, Frank Pollmann, and Andrew G Green. Parallel quantum simulation of large systems on small nisq computers. *npj Quantum Information*, 7(1):1–7, 2021.

[120] Sheng-Hsuan Lin, Rohit Dilip, Andrew G. Green, Adam Smith, and Frank Pollmann. Real- and imaginary-time evolution with compressed quantum circuits. *PRX Quantum*, 2:010342, Mar 2021.

[121] Adam Smith, Bernhard Jobst, Andrew G. Green, and Frank Pollmann. Crossing a topological phase transition with a quantum computer. *Phys. Rev. Research*, 4:L022020, Apr 2022.

[122] Shi-Ju Ran. Encoding of matrix product states into quantum circuits of one- and two-qubit gates. *Phys. Rev. A*, 101:032310, Mar 2020.

[123] James Dborin, Fergus Barratt, Vinul Wimalaweera, Lewis Wright, and Andrew G. Green. Matrix product state pre-training for quantum machine learning, 2021.

[124] Manuel S. Rudolph, Jing Chen, Jacob Miller, Atithi Acharya, and Alejandro Perdomo-Ortiz. Decomposition of matrix product states into shallow quantum circuits, 2022.

[125] Manuel S. Rudolph, Jacob Miller, Jing Chen, Atithi Acharya, and Alejandro Perdomo-Ortiz. Synergy between quantum circuits and tensor networks: Short-cutting the race to practical quantum advantage, 2022.

[126] Kevin C. Smith, Eleanor Crane, Nathan Wiebe, and S. M. Girvin. Deterministic constant-depth preparation of the aklt state on a quantum processor using fusion measurements, 2023.

[127] Bruno Murta, Pedro M. Q. Cruz, and J. Ferná ndez-Rossier. Preparing valence-bond-solid states on noisy intermediate-scale quantum computers. *Physical Review Research*, 5(1), mar 2023.

[128] Tianqi Chen, Ruizhe Shen, Ching Hua Lee, and Bo Yang. High-fidelity realization of the aklt state on a nisq-era quantum processor, 2023.

[129] Seth Lloyd. Universal quantum simulators. *Science*, 273(5278):1073–1078, 1996.

[130] Alexander Miessen, Pauline J. Ollitrault, Francesco Tacchino, and Ivano Tavernelli. Quantum algorithms for quantum dynamics. *Nature Computational Science*, pages 1–13, December 2022. Publisher: Nature Publishing Group.

[131] Ying Li and Simon C. Benjamin. Efficient Variational Quantum Simulator Incorporating Active Error Minimization. *Physical Review X*, 7(2):021050, June 2017. Publisher: American Physical Society.

[132] Xiao Yuan, Suguru Endo, Qi Zhao, Ying Li, and Simon Benjamin. Theory of variational quantum simulation. *Quantum*, 3:191, October 2019. arXiv:1812.08767 [quant-ph].

[133] Adam Smith, M. S. Kim, Frank Pollmann, and Johannes Knolle. Simulating quantum many-body dynamics on a current digital quantum computer. *npj Quantum Information*, 5(1):1–13, November 2019. Number: 1 Publisher: Nature Publishing Group.

[134] Cristina Cîrstoiu, Zoë Holmes, Joseph Iosue, Lukasz Cincio, Patrick J. Coles, and Andrew Sornborger. Variational fast forwarding for quantum simulation beyond the coherence time. *npj Quantum Information*, 6(1):1–10, September 2020. Number: 1 Publisher: Nature Publishing Group.

[135] Stefano Barison, Filippo Vicentini, and Giuseppe Carleo. An efficient quantum algorithm for the time evolution of parameterized circuits. *Quantum*, 5:512, July 2021. arXiv:2101.04579 [cond-mat, physics:physics, physics:quant-ph].

[136] F. Barratt, James Dborin, Matthias Bal, Vid Stojevic, Frank Pollmann, and A. G. Green. Parallel quantum simulation of large systems on small NISQ computers. *npj Quantum Information*, 7(1):1–7, May 2021. Number: 1 Publisher: Nature Publishing Group.

[137] Steven R. White. Density matrix formulation for quantum renormalization groups. *Phys. Rev. Lett.*, 69:2863–2866, Nov 1992.

[138] Kyungjoo Noh, Liang Jiang, and Bill Fefferman. Efficient classical simulation of noisy random quantum circuits in one dimension. *Quantum*, 4:318, September 2020. arXiv:2003.13163 [quant-ph].

[139] Meng Zhang, Chao Wang, Shaojun Dong, Hao Zhang, Yongjian Han, and Lixin He. Entanglement entropy scaling of noisy random quantum circuits in two dimensions. *Physical Review A*, 106(5):052430, November 2022. Publisher: American Physical Society.

[140] Vincenzo Alba and Pasquale Calabrese. Entanglement dynamics after quantum quenches in generic integrable systems. *SciPost Physics*, 4(3), mar 2018.

[141] Norbert Schuch, Michael M Wolf, Karl Gerd H Vollbrecht, and J Ignacio Cirac. On entropy growth and the hardness of simulating time evolution. *New Journal of Physics*, 10(3):033032, 2008.

[142] Baptiste Anselme Martin, Thomas Ayral, François Jamet, Marko J. Rančić, and Pascal Simon. Combining matrix product states and noisy quantum computers for quantum simulation, 2023.

[143] C. Schön, E. Solano, F. Verstraete, J. I. Cirac, and M. M. Wolf. Sequential Generation of Entangled Multiqubit States. *Physical Review Letters*, 95(11:110503, 2005. Publisher: American Physical Society.

[144] Shi-Ju Ran. Encoding of matrix product states into quantum circuits of one- and two-qubit gates. *Physical Review A*, 101(3):032310, March 2020. Publisher: American Physical Society.

[145] Manuel S. Rudolph, Jing Chen, Jacob Miller, Atithi Acharya, and Alejandro Perdomo-Ortiz. Decomposition of Matrix Product States into Shallow Quantum Circuits, September 2022. arXiv:2209.00595 [quant-ph].

[146] Tomonori Shirakawa, Hiroshi Ueda, and Seiji Yunoki. Automatic quantum circuit encoding of a given arbitrary quantum state, December 2021. arXiv:2112.14524 [cond-mat, physics:quant-ph].

[147] Sheng-Hsuan Lin, Rohit Dilip, Andrew G. Green, Adam Smith, and Frank Pollmann. Real- and imaginary-time evolution with compressed quantum circuits. *PRX Quantum*, 2(1):010342, March 2021. arXiv:2008.10322 [cond-mat, physics:quant-ph].

[148] James Dborin, Fergus Barratt, Vinul Wimalaweera, Lewis Wright, and Andrew G. Green. Matrix Product State Pre-Training for Quantum Machine Learning, July 2021. arXiv:2106.05742 [quant-ph].

[149] Manuel S. Rudolph, Jacob Miller, Jing Chen, Atithi Acharya, and Alejandro Perdomo-Ortiz. Synergy Between Quantum Circuits and Tensor Networks: Short-cutting the Race to Practical Quantum Advantage, August 2022. arXiv:2208.13673 [quant-ph].

[150] Mohsin Iqbal, David Muñoz Ramo, and Henrik Dreyer. Preentangling quantum algorithms – the density matrix renormalization group-assisted quantum canonical transformation, 2022.

[151] William Huggins, Piyush Patil, Bradley Mitchell, K. Birgitta Whaley, and E. Miles Stoudenmire. Towards quantum machine learning with tensor networks. *Quantum Science and Technology*, 4(2):024001, January 2019. Publisher IOP Publishing.

[152] Jin-Guo Liu, Yi-Hong Zhang, Yuan Wan, and Lei Wang. Variational quantum eigensolver with fewer qubits. *Physical Review Research*, 1(2):023025, September 2019.

[153] Qiang Miao and Thomas Barthel. A quantum-classical eigensolver using multiscale entanglement renormalization, September 2021. arXiv:2108.13401 [quant-ph].

[154] Adam Smith, Bernhard Jobst, Andrew G. Green, and Frank Pollmann. Crossing a topological phase transition with a quantum computer. *Physical Review Research*, 4(2):L022020, April 2022. Publisher: American Physical Society.

[155] Reza Haghshenas, Johnnie Gray, Andrew C. Potter, and Garnet Kin-Lic Chan. Variational Power of Quantum Circuit Tensor Networks. *Physical Review X*, 12(1):011047, March 2022. Publisher: American Physical Society.

[156] James Dborin, Vinul Wimalaweera, F. Barratt, Eric Ostby, Thomas E. O'Brien, and A. G. Green. Simulating groundstate and dynamical quantum phase transitions on a superconducting quantum computer. *Nature Communications*, 13(1):5977, October 2022. Number: 1 Publisher: Nature Publishing Group.

[157] Eli Chertkov, Justin Bohnet, David Francois, John Gaebler, Dan Gresh, Aaron Hankin, Kenny Lee, David Hayes, Brian Neyenhuis, Russell Stutz, Andrew C. Potter, and Michael Foss-Feig. Holographic dynamics simulations with a trapped-ion quantum computer. *Nature Physics*, 18(9):1074–1079, September 2022. Number: 9 Publisher: Nature Publishing Group.

[158] Michael Foss-Feig, Stephen Ragole, Andrew Potter, Joan Dreiling, Caroline Figgatt, John Gaebler, Alex Hall, Steven Moses, Juan Pino, Ben Spaun, Brian Neyenhuis, and David Hayes. Entanglement from Tensor Networks on a Trapped-Ion Quantum Computer. *Physical Review Letters*, 128(15):150504, April 2022. Publisher: American Physical Society.

[159] Daoheng Niu, Reza Haghshenas, Yuxuan Zhang, Michael Foss-Feig, Garnet Kin-Lic Chan, and Andrew C. Potter. Holographic Simulation of Correlated Electrons on a Trapped-Ion Quantum Processor. *PRX Quantum*, 3(3):030317, August 2022.

[160] Francois Jamet, Connor Lenihan, Lachlan P. Lindoy, Abhishek Agarwal, Enrico Fontana, Baptiste Anselme Martin, and Ivan Rungger. Anderson impurity solver integrating tensor network methods with quantum computing, 2023.

[161] Glen Evenbly and Guifré Vidal. Algorithms for entanglement renormalization. *Physical Review B*, 79(14):144108, 2009.

[162] Joel J. Wallman and Joseph Emerson. Noise tailoring for scalable quantum computation via randomized compiling. *Phys. Rev. A*, 94:052325, Nov 2016.

[163] Qiskit contributors. Qiskit: An open-source framework for quantum computing, 2023.

[164] The Qiskit Research developers and contributors. Qiskit research, March 2023.

[165] Kaelyn J. Ferris, A. J. Rasmusson, Nicholas T. Bronn, and Olivia Lanes. Quantum simulation on noisy superconducting quantum computers, 2022.

[166] Youngseok Kim, Christopher J. Wood, Theodore J. Yoder, Seth T. Merkel, Jay M. Gambetta, Kristan Temme, and Abhinav Kandala. Scalable error mitigation for noisy quantum circuits produces competitive expectation values. *Nature Physics*, feb 2023.

[167] I-Chi Chen, Benjamin Burdick, Yongxin Yao, Peter P. Orth, and Thomas Iadecola. Error-mitigated simulation of quantum many-body scars on quantum computers with pulse-level control. *Phys. Rev. Res.*, 4:043027, Oct 2022.

[168] Nathan Earnest, Caroline Tornow, and Daniel J. Egger. Pulse-efficient circuit transpilation for quantum applications on cross-resonance-based hardware. *Phys. Rev. Res.*, 3:043088, Oct 2021.

[169] Maurits S. J. Tepaske, Dominik Hahn, and David J. Luitz. Optimal compression of quantum many-body time evolution operators into brickwall circuits. *SciPost Physics*, 14(4), apr 2023.

[170] Conor Mc Keever and Michael Lubasch. Classically optimized hamiltonian simulation. *Physical Review Research*, 5(2), jun 2023.